People's Democratic Republic of Algeria

Ministry of Higher Education and Scientific Research

University Abbes Laghrour Khenchela

Faculty of Sciences and Technology

Department of Matter Sciences

THESIS

Presented for LMD Doctorate Degree Requirement

In Chemistry

Specialty: Materials Chemistry

By: Hanane Berkani

Entitled

Additive's Structural and Magnetic Effect on the Solid State Reaction in Fe-Co Powders

Jury Members:

A. Messai	Professor	Abbes Laghrour Khenchela University	President
R. Siab	Professor	Chadli Bendjedid-El Tarf University	Supervisor
W. Tebib	Professor	Chadli Bendjedid-El Tarf University	Co- Supervisor
A. Azizi	Professor	Ferhat Abbes Sétif 01 University	Examiner
A. Djelloul	Professor	Abbes Laghrour Khenchela University	Examiner

Defended on Decembre 07, 2023

Acknowledgments

No one walks alone in the journey of life, but when walking, you start to thank those who joined you, walked beside you, and helped you along the way. First and foremost, I would like to praise Allah who gave me the strength and patience during my study to complete this Ph.D project.

I would like to express my sincere gratitude to my supervisor **Pr. Rachid Siab** for accepting to supervise my Ph.D thesis and giving me an opportunity to work at the Materials Physico-Chemistry Laboratory (MPCL) Chadli Bendjedid-El Tarf University. I would like to thank the Physics Department, Science and Technology Faculty, and Eltarf University for giving me the opportunity to work on my Ph.D project in Materials Physico-Chemistry Laboratory (MPCL), for providing access to some of their equipments, for their dedication to excellence, and assistance in all of my academic endeavors. I extend my deepest gratitude to my co-supervisor **Pr. Wassila Tebib** for the professional and personal guidance, the valuable feedback, precious advice, patience, motivation, and immense knowledge that made the accomplishments of this Ph.D project possible.

I would like to thank all examiners for taking the time to read my thesis and to evaluate this work. Sincere thanks for agreeing to be the examiners for my research.

It is a pleasure to dedicate appreciation to MPCL members, for the invaluable support. I am especially thankful to **Dr. Ali Hafs** for the VSM characterization and to **Dr. Loucif Redouani** and **Mme. Saida Boukeffa** for XRD investigations.

I would like to thank the entire management team and engineers of pedagogic laboratories at Abbes Laghrour Khenchela University for their support and help. Special thanks also go to **Dr. Asma Kheddouma** for providing insight and expertise, from a microbiological point of view, to this project.

I warmly thank **Pr. Amel Messai, Pr. Abdelkader Djelloul** and **Pr. Mohamed Boudina, Pr. Abdecharif Boumaza**, **Pr. Linda Aissani** for their precious help and insightful comments.

I am also thankful to all my closest friends (**Rachida Litim**, **Oumhani Ounnassi**, **Amira Belhadj** and **Aymen**), well-wishers, and colleagues (**Mme. Faiza Salhi, Mme. Marwa Brinis**, **Mrs. Ismahane Chenouga**, **Mrs. Souria Bendjemaa**, **Mme. Fatouma Ouannassi, Mme. Saida Hoggas**, **Mme. Lamia Radjhi**, **Mrs. Rania Kara, M. Ali Akram Derarjda** and **M. Ragheb Khalil Bouriche**) for their support and cooperation.

Last but not least, nothing would be possible without the love and support of my entire family members, especially my beloved father **Boubaker Berkani** and my dearest mother **Djamila Berkani**, who have been a constant source of support and encouragement during the challenges of graduate

school and life. Thanks to my brothers (**Abdelaziz**, **Abdelhafid**, and **Abdelghani**), my sisters (**Assia**, **Soumia**, and **Hadil**). All of them, in their own ways, supported me; I am truly thankful for having you in my life.I sincerely thank all my relatives who were with me with their support, love and prayers, especially my grandmother, my uncles, my aunts, and my cousins.

Thank you all for a memorable experience.

Dedication

This thesis work is dedicated to the memory of my lovely grandfather (**Mohamed Ben Abdellah Berkani)** who passed away when I began my doctoral studies.

"Nothing in life is to be feared, it is only to be understood. Now is the time to understand more, so that we may fear less".

Marie Curie

Abstract

The main goal of this thesis is to understand the influence of the average crystallite size as a function of the milling time on the structural, microstructural, mechanical, magnetic properties and also the growth of bacteria strains. This study is devoted to the elaboration of nanostructured $Fe_{15}Co_2P_3$powder mixtures by mechanical alloying process which allows the formation of alloys with a grain size in the nanometer range, then the physicochemical characterization of the powder mixtures and also the effect of $Fe_{15}Co_2P_3$ powder mixtures on the growth of test bacteria. A high energy planetary ball-mill Retsch PM 400 was chosen for synthesis the powder mixtures. Phases formation, microstructural, structural, mechanical magnetic and growth of bacteria strains of the ball milled powders were studied as a function of milling time, t (t = 0h, 1h, 2h and 3h) by X-ray diffraction using the MAUD program which is based on the Rietveld method, vibrating sample magnetometer, and Fourier-transform infrared spectroscopy and ultraviolet–visible spectroscopy. The XRD results revealed the coexistence of the centered cubic α-Fe(P) solid solution and $Co_{75}Fe_{25}$ binary phase, for all milled samples. The average crystallite size <L> of the formed solid solution and binary phase decreased with the milling time. The evolution of the mechanical properties "Young's Modulus and Poisson's Coefficient" demonstrated the stiffness and the deformation properties of the formed phase and solid solution. The milling process induced some important changes in the magnetic properties, whereas the variation of the saturation magnetization and coercivity was associated mainly with the particle size refinement, accumulation of microstrain and formation of solid solution α-Fe(P) and $Co_{75}Fe_{25}$ phase. Several fundamental magnetic parameters have been discussed as a function of milling time. The current study provides evidence that milled $Fe_{15}Co_2P_3$ powder mixtures with different concentrations have better antibacterial activity against Gram-positive strains and the same powder mixtures could be used as cofactor for the examined Gram-negative strains.

Keywords: High energy ball milling; Nanostructured $Fe_{15}Co_2P_3$ powder mixtures; X-ray diffraction; Mechanical properties; Magnetic properties; Antibacterial activity.

Résumé

Le but principal de cette thèse est de comprendre l'influence de la taille moyenne des grains en fonction du temps de broyage sur les propriétés structurales, microstructurales, mécaniques, magnétiques et aussi la croissance des bactéries. Cette étude est consacrée sur l'élaboration d'un mélange de poudres nanostructures $Fe_{15}Co_2P_3$ par broyage mécanique qui permet la formation des alliages avec une taille de grain dans le domaine nanométrique, puis les caractérisations physicochimiques des mélange des poudres et aussi l'effet des mélange des poudres $Fe_{15}Co_2P_3$ sur la croissance des bactéries testées.Un broyeur à billes haute énergie de type Retsch PM 400 a était choisi pour synthétiser le mélange de poudres. La formation des phases, les proprietés structurales, microstructurales, mécaniques, magnétiques des poudres broyés ainsi que la croissance des bactéries ont été étudiés en fonction de temps de broyage, t (t = 0h, 1h, 2h and 3h) par les technique de diffraction des rayons X en utilisant un programme d'affinement structural MAUD basé sur la méthode de Rietveld, la magnétométrie à échantillon vibrant, la spectriscopie infrarouge à transformée de Fourier et la spectroscopie ultraviolet-visible. Les résultats de la diffraction des rayons X révèlent la coexistence des structures cubiques centrées de la solution solide α-Fe(P) et la phase binaire $Co_{75}Fe_{25}$. La taille des crystallites <L> de la solution solide et de la phase binaire diminue en fonction du temps de broyage. L'évolution des propriétés mécaniques (module de Young et coefficient de Poisson) révèlent la rigidité et la grande aptitude à la déformation de la solution solide et la phase formées .Le processus de broyage a induit des changements importants dans les propriétés magnétiques, tandis que la variation da l'aimantation à saturation et de la coercivité était principalement associée au raffinement de la taille des grains à l'accumulation de microdéformations et à la formation d'une solution solide α-Fe(P) et de la phase $Co_{75}Fe_{25}$. Plusieurs paramètres magnétiques fondamentaux ont été discuté on fonction de temps de broyage. L'étude actuelle fournit la preuve que les mélanges des poudres $Fe_{15}Co_2P_3$ broyés avec différentes concentrations ont montré une bonne activité antibactérienne contre les souches de Gram positif et que les mêmes mélanges des poudres pourraient être utilisés comme cofacteur pour les souches Gram négatif examinées.

Mots-clés: Broyage mécanique haute énergie; Mélange de poudres nanostructures $Fe_{15}Co_2P_3$; Diffraction des rayons X; Propriétés mécanique ; Propriétés magnétique; Activité antibactérienne.

ملخص

الهدف الرئيسي من بحث الدكتوراه هذا هو فهم تأثير الحجم المتوسط الحبوب كدالة لوقت الطحن على الخصائص التركيبية والبنيوية والميكانيكية إضافة للمغناطيسية و كذلك نمو البكتيريا. هذه الدراسة مخصصة لتطوير خلائط مساحيق $Fe_{15}Co_2P_3$ ذات البنية النانومترية عن طريق الطحن (التوليف) الميكانيكي لصناعة السبائك التي تسمح لتشكيل سبائك من الحجم الحبيبي في نطاق النانومتر ثم التوصيف الفيزيوكيميائي لخلائط المسحوق وأيضا تاثير خلائط مسحوق $Fe_{15}Co_2P_3$ في اختبار نمو البكتيريا. تم اختيار مطحنة كوكبية عالية الطاقة من نوع Retsch PM 400 لصناعة خلائط المساحيق. تمت دراسة تكوين الاطوار والخصائص الهيكلية البنية الدقيقة الميكانيكية إضافة الى الخصائص المغناطيسية والمضادة للبكتيريا للمساحيق المطحونة بدلالة زمن الطحن (0 سا، 1 سا، 2 سا، 3 سا) باستخدام حيود الأشعة السينية X باستعمال برنامج (MAUD) الذي يعتمد على طريقة Rietveld الاهتزاز المغناطيسي وجهاز مطياف تحويل فورييه بالأشعة تحت الحمراء ومطيافية الأشعة فوق البنفسجية المرئية. أكدت الدراسة بالأشعة السينية تشكيل هياكل مكعبة مركزية لكل من المحلول الصلب α-Fe(P) والطور الثنائي $Co_{75}Fe_{25}$ الناتجين في جميع العينات المطحونة. التناقص في حجم الحبوب <L> للمحلول الصلب والطور الثنائي المتشكلين مع زيادة زمن الطحن $<\sigma^2>^{½}$. يكشف تطور الخواص الميكانيكية "معامل يونغ ومعامل بواسون" عن خواص الصلابة وقابلية التشوه للمساحيق للمحلول الصلب والطور المتشكلين. عملية الطحن أدت إلى تغيرات مهمة في الخصائص المغناطيسية فتغيرات التشبع المغناطيسي والمقاومة المغناطسية مرتبطة أساسا مع حجم الحبوب والتشوهات وكذلك تكوين المحلول الصلب α-Fe(P) والطور $Co_{75}Fe_{25}$. تمت مناقشة العديد من الخواص المغناطيسية الأساسية بدلالة زمن الطحن. تقدم الدراسة الحالية دليلا على أن خلائط المسحوق المطحون بتراكيز مختلفة لها نشاط مضاد للبكتيريا السلالات موجبة Gram-positive و يمكن استخدام نفس الخلائط كعامل مساعد لنمو السلالات سالبة Gram-negative التي تم فحصها.

الكلمات المفتاحية: طحن ميكانيكي عالي الطاقة؛ ؛ خليط لمساحيق نانومترية $Fe_{15}Co_2P_3$ ؛ حيود الاشعة السينية ؛ خواص ميكانيكية ؛ خواص مغناطيسية ؛ نشاط مضاد للبكتيريا.

Table of Contents

Abbreviations and Symbols

MAUD	Materials analysis using diffraction
XRD	X-rays diffraction
UV	Ultraviolet
VSM	Vibrating sample magnetometer
UV-Vis	Ultraviolet Visible
FTIR	Fourier-Transform Infrared Spectroscopy
ICSD	Inorganic crystal structure database
0D	Zero-dimensional nanomaterials
1D	One-dimensional nanomaterials
2D	Two-dimensional nanomaterials
3D	Three-dimensional nanomaterials
BPR	Ball to powder ratio
S. aureus	Staphylococcusaureus
K. pneumonia	Klebsiella pneumonia
H. influenzae	Haemophilus influenzae
OD	Optical density
H	Magnetic field strength
X	Magnetic susceptibility
T_C	Curie temperature
M	Magnetization
M_r	Remanent magnetization
M_S	Saturation magnetization

H_C	Coercivity
$<L>$	Average crystallite size
$\sigma(L)$	Hardness
σ_0	Friction stress
k_{HP}	Hall-Petch intensity parameter
B	Magnetic induction
μ_0	Magnetic permeability of free space
μ_r	Relative permeability
D	Grain size
f	Vibration frequency
A	Vibration amplitude
ω	Angular velocity
E_m	Total mechanical energy transferred by the ball mill to the material
Ω	Disc rotation speed
R	Ball to powder weight ratio
ω	Vial rotation speed
t	Milling time
n	Order of diffraction
λ	Wavelength of the incident X-ray
d_{hkl}	Distance between the crystallographic planes (h,k, and l)
θ	Bragg angle
y_i	Observed intensity
y_{ci}	Calculated intensity
w_i	Weight factor

K	Miller's index for a reflection h, k and l
S_ϕ	Scale factor
$j_{\phi k}$	Multiplicity factor
k^{th}	Reflexion peak
$L_{P\phi k}$	Lorentz-Polarization factor
$O_{\phi k}$	Correction factor
A	Absorption factor
$F_{\phi K}$	Structure factor
$\Omega_{i\phi k}$	Profile shape function
R_p	Reliability factor
R_{wp}	Reliability weighted
R_{exp}	Expected R factor
R_{Bragg}	Bragg factor
GoF	Goodness of fit
β_{hkl}	Line broadening at half the maximum intensity
σ	Strain also called deformation parameter
$< \sigma^2 >^{1/2}$	Average strain
I_0	Incident intensity of light
I	Transmitted intensity of light
R	Radius
ΔV	Relative deviation of the lattice volume
V	Cell volume after milling
V_0	Cell volume from that of the perfect crystal

SFP	Stacking fault probability
α'	Intrinsic deformation faults probability
α''	Extrinsic deformation faults probability
β	Twin faults
N	Average number of compact atomic planes between two consecutive stacking faults
ρ	Dislocation density
E	Young's modulus
N	Poisson's ratio
K	Bulk modulus of elasticity
K	Magnetocrystalline anisotropy constant
Q_h	Maximum energy loss
μ_{max}	Maximum magnetic permeability
H_n	Nucleation field
SFD	Switching field distribution
v	Poisson's ratio

List of Figures

Chapter I

Chapter II

Chapter III

Chapter IV

Chapter V

Appendix

List of Tables

Introduction

“Nano”, this small word with huge potential has rapidly insinuated itself into the world’s consciousness of today’s modern area. It is not a buzzword; rather, this term indicates the dimension of the materials. It has conjured up speculation about a seismic shift in almost every aspect, leading to undiscovered realms of science and creating new research domains. Nanomaterials are the materials that have at least one dimension in a nanoscale regime, more specifically within 100 nm. In the past few decades, the emergence and use of nanomaterials in consumer products has revolutionized many industries. This novel class of materials has emerged as an exciting class of materials that are in high demand for a range of practical applications due to their unique structural features, and hence their unusual physical, chemical, mechanical, and magnetic properties. These characteristics result from the refinement of the crystallite size up to the nanoscale and the large fraction of the atoms residing in the grain boundaries. Nanostructured materials with critical dimensions have attracted increasingly more attention from the materials community due to their existing and/or potential applications in a wide variety of technological areas and fields.

Nanomaterials can be classified based on their origin or according to their dimensionality and composition. There are different methods for producing nanomaterials. The two major approaches are the bottom up and the top down methods (*Iqbal, et al., 2012* and *Wang, et al., 2004*). Mechanical milling is one among the top down methods which is a good processing technique to produce a large variety and large quantities of nanostructured materials at the solid state (*Loginov, et al., 2015*) from compositional heterogeneous (generally pure elements) powder. Nanomaterials are often used in health care diagnostics. A number of manufactured nanomaterials have, however, been associated with health hazards. Their application has gained immense interest in recent years owing to their superior properties compared to traditional materials. Nanomaterials extensively explored for health care diagnostics are predominantly either purely organic or inorganic materials, or a combination of both. Nonetheless, due to their small size and large surface area, particulate nanomaterials in powder form may present risks of explosion, whereas non-nanosized versions of the same substance may not.

A worldwide initiative is under way to develop a new generation of antibacterial nanomaterials. The antibacterial activity of nanomaterials has been attributed to shape, high surface area and small size that permit nanomaterials to interact thoroughly with bacterial membrane. The antibacterial mechanism depends on the bacteria type; Gram-negative or Gram-positive. Generally, bacteria distinction is based on the difference in the structure of the bacterial wall. Gram-negative bacteria have an outer cell membrane in contrast of Gram-positive bacteria. Currently, diverse metallic nanomaterials are regarded as practical alternative to antibiotics due to their great effectiveness towards antibacterial activities. Recently, the bacteriological behavior of nanomaterials synthetized by mechanical milling is a challenge for many researchers (*Bagha, et al., 2018* and *Karthik, et al., 2016*).
Magnetic nanomaterials have been studied due to their remarkable properties, like saturation magnetization and coercivity which are considerably different from bulk materials and closely related

to the structure and microstructures (*Herzer, 1997* and *Shull, 2007*). It is well known that the good understanding of the magnetic or mechanical properties of materials often requires knowledge of their microstructure, in particular their grain size. Iron cobalt (Fe-Co) alloys are the most well-known and effective magnetic materials due to their benefits of magnetic properties, with high Curie temperatures, the highest saturation magnetization, high permeability, low losses and are relatively strong, in addition to their good strengths, structural chemical properties and effectiveness in catalytic process (*Bozorth, 1951* ; *Sourmail, 2005* and *Quigley, 1993*). Since the discovery of these interesting alloys by Elmen (*1929*), their cost has confined them to applications where a small volume and high magnetic performances are critical. Currently, Fe-Co alloys are ideally suited for applications requiring high flux density; they are used in applications where their high saturation values provide an advantage in reducing components weight and/or volume. Fe-Co alloys find application in data storage, high performance transformers, and pole tips for high field magnets (*Sundar* and *Deevi, 2005* and *Sourmail, 2005*). Due to the interesting effect of the mechanical milling method in the magnetic and mechanical properties of Fe-Co alloys, various studies have been carried out on Fe-Co nanostructured powders produced by this technique for different elaboration conditions using several types of ball-mills (*Sánchez-De Jesús, et al., 2016* ; *Moumeni, et al., 2005* ; *Akkouche, et al., 2011* and *Laala-Bouali, et al., 2013*). A critical step was undertaken in achieving the ball-milled Fe-Co alloy combined with other elements of industrial relevance, such as Mo (*Moumeni, et al., 2013* and *Tavakoli, et al., 2013),*V *(Chitsazan, et al., 2011),* Ni *(Ahmadian, et al., 2012),* Nb *(Nasibi, et al., 2012),* Cr *(Bentayeb, et al., 2007),* and *C (Wu, et al., 2013*). Most solute additions in Fe-Co alloys tend to reduce the saturation of the alloy and in general increase its coercivity, thereby degrading its magnetic performance (*Sourmail, 2005*). Those studies gave controversial results with regard to the magnetic parameters (saturation magnetization and coercive field) as a function of the milling duration and, therefore, the grain size. The aim of the presented thesis work deals with the mechanical milling and characterization of $Fe_{15}Co_2P_3$ nanostructured powders. Phosphorus included in iron cobalt alloys can improve the structural, microstrucrtural, mechanical and magnetic properties of the nanomaterial. For example, a very small amount of red P mixed with iron cobalt alloys can result in weld brittleness and apparently increase the tendency of crack.

In the present thesis, clarifications of the effect of mechanical milling on microstructure, mechanical, magnetic and antibacterial properties of the $Fe_{15}Co_2P_3$ powder mixtures at various milling times is discussed. The current PhD thesis consists of five chapters organized as follows:

The first chapter provides the related literature review. In particular, nanomaterials and their classifications are introduced and their fundamentals properties are outlined. Various nanomaterial synthesis methods, including top-down and bottom-up approaches, are discussed. This chapter describes advances in nanomaterials, specifically in healthcare. Finally, basic knowledge and the literature review related to phosphides and iron cobalt alloys are provided.

The second chapter is dedicated to the experimental procedures and processes employed for the mechanical milling and the bacteriology tests during the preparation of this thesis together with the main characterization techniques used.

In the third chapter, the structural, microstructural and mechanical properties of $Fe_{15}Co_2P_3$ powder mixtures at different milling periods are presented.

In the fourth chapter, the magnetic behavior of $Fe_{15}Co_2P_3$ powder mixtures milled for several times is discussed. The dependence of magnetic properties with microstructural parameters of the ball-milled $Fe_{15}Co_2P_3$ powder mixtures were investigated in details.

In the last chapter, it is found that the novel synthesized nanomaterial exhibit bacteriological behavior for both, Gram-positive and Gram-negative bacteria.

Finally, the thesis was concluded with a summary of the main results obtained and a highlight of the contributions of this study in terms of the mechanical, magnetic and bacteriologycal behavior of the proposed nanomaterial. Moreover, future research is recommended.

Chapter 1:

Backgrounds and Literature Review

This chapter contains general information about nanomaterials, their classification, their properties, various synthetic process of nanomaterials including mechanical milling and factors affecting the mechanical milling process, nanomaterial healthcare applications, basic information and the literature review of work conducted on CoFe based alloys, phosphides FeP, CoP, and FeCoP alloys.

I.1 Nanomaterials

The prefix “nano” derived from the Greek language “*νάν*ς” (nanus) literally means “dwarf” (*Fang, et al.,2009*). Nowadays, this prefix means a billionth (1×10^{-9}) of any unit *(Buzea, et al.,2007)*. In general, nanometer grain size materials are considered as having at least one dimension in the 1-100 nm range. Because of such small dimensions, a large volume fraction of the atoms is located at the grain boundaries, and this confers special attributes to these materials (*Suryanarayana, 1995)*.

There are many definitions of the term “Nanomaterial”. The definition given by the European Commission Stated in October 2011 that the particle size of at least half of the particles in the number size distribution must measure 100 nm or below. The term “nanomaterial” refers to materials that contain nanoscale structures internally or with internal structure or surface structure in the nanoscale. Nanomaterials means natural, incidental or manufactured chemical substances or materials containing particles (*Lungu, et al., 2015* and *Galloway, et al., 2017*). In an unbound state, as an aggregate or as an agglomerate and where, for 50 % or more of the particles in the number size distribution, one or more external dimension measuring in the size range 1–100 nm.

I.2 Classifications of Nanomaterials

In the past few decades, hundreds of novel nanomaterials have been obtained and therefore their classification became necessary. Factors such as source of origin, dimensionality and composition are used to determine few of these classifications.

I.2.1 Classification According to the Source of Origin

Nanomaterials can be classified based on their source of origin, which means the source materials to produce nanomaterials, into three main categories (*Tahir, et al., 2021*):

- Incidental nanomaterials, also called subsidiary nanomaterials which are produced incidentally or as byproducts of chemical processes; for example the nanoparticles produced from vehicle engine exhaust and anthropic or natural combustion processes such as forest fires.
- Engineered nanomaterials, which have been manufactured to have certain required properties for desired applications. Furthermore, those artificial nanomaterials are prepared deliberately through a well-defined mechanical and fabrication process. Examples of artificial nanomaterials include carbon nanotubes and semiconductor nanoparticles like quantum dots, etc. (*Buzea, et al., 2007*).
- Naturally produced nanomaterials, which can be found in the bodies of organisms, insects, plants, animals and human bodies. Examples of some natural nanomaterials include viruses, protein, molecules, antibodies, minerals, natural colloids, insect wings and opals, spider silk, lotus leaf, gecko feet, volcanic ash, and ocean spray (*Fabbro, et al., 2012*).

The distinctions between naturally occurring, incidental, and manufactured nanoparticles are often indistinct. In some cases, incidental nanomaterials can be reflected as a subgroup of naturally produced nanoparticles.

I.2.2 Classification According to Dimensionality

Nanomaterials can be classified based on their dimensionalities into four groups. This classification was first setby *Gleiter, et al.* in 1995 (*Gleiter, et al., 1995* and *2000*), and further explored and described by Skorokhod in 2000 as zero-dimensional (0D), one-dimensional (1D), two-dimensional (2D) and three-dimensional (3D) nanomaterials, with all dimensions in the nanoscale. Later on, such a classification was newly modified and presented by Pokropivny and Skorokhod (*2008*). The schematic representation of the classification of nanomaterials according to their dimensions is given in Figure I.1.

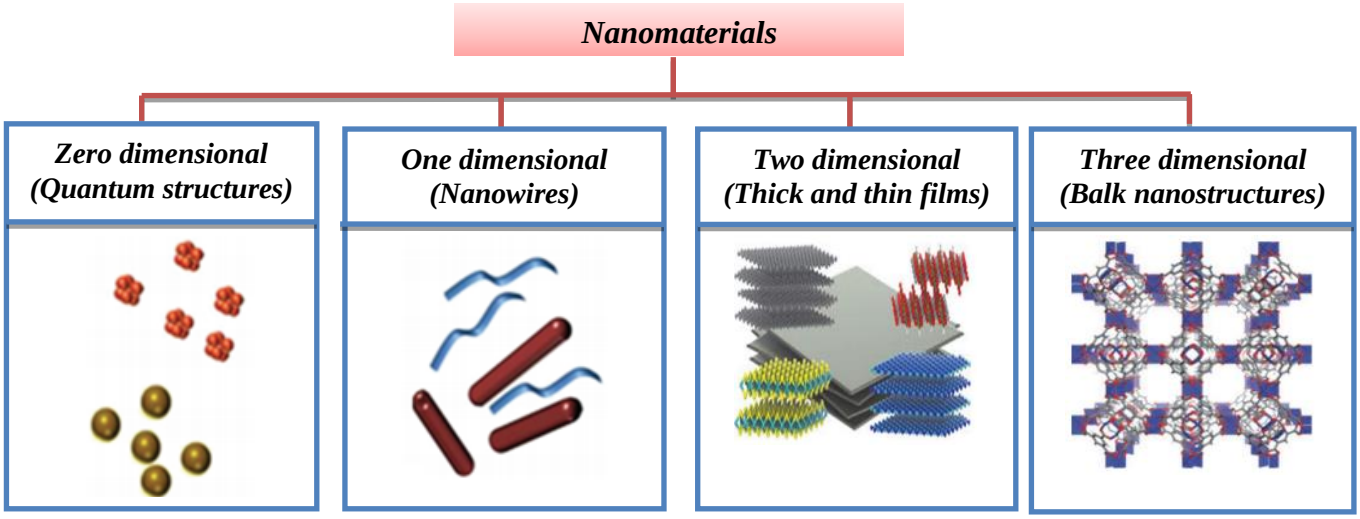

Figure I.1: *Schematic representation of classification of nanomaterials based on their dimensions (Alagarasi, 2009* and *Sharma, et al., 2019).*

Zero-dimensional nanomaterials (clusters) are usually denoted as 0D structures. Nanoparticles, nanoclusters and nanocrystals belong to this category. This range corresponds to colloidal particles. The most common representation of 0D nanomaterials is nanoparticles which could (*Sharma, et al., 2019*):

- be amorphous or crystalline,
- be single crystalline or polycrystalline,
- be metallic, ceramic or polymeric,
- consist of single or multi-chemical elements,
- exhibit various shapes and forms, and
- exist individually or be incorporated in a matrix.

One-dimensional nanomaterials (Long and nanoscale thin) are referred to as 1D structures. They are the materials that are equivalent in all but one direction. Examples of nanomaterials that belong to this class are nanotubes, nanorods, nanowires, filaments, or fibers (*Saleh, et al., 2016*). 1D nanomaterials could be (*Sharma, et al., 2019*):

- amorphous or crystalline,
- single crystalline or polycrystalline,
- chemically pure or impure,
- embedded within another medium, and
- metallic, ceramic or polymeric.

Two-dimensional (2D) nanomaterials (Nanoscale thickness but large area) consist of two outer dimensions beyond the nanorange (>100 nm) and one dimension in the range of nanometer. Free particles with a large aspect ratio, with dimensions in the nanoscale range, are considered 2D nanomaterials. Examples include nanosheets, nanofilms, nanolayers and nanocoatings which can be (*Sharma, et al., 2019*):

- amorphous or crystalline,
- made up of various chemical compositions,
- used as a single layer or multilayer structures,
- deposited on a substrate,
- integrated in a surrounding matrix material, and
- metallic, ceramic or polymeric.

Three-dimensional (3D) nanomaterials are associated with three arbitrary dimensions. 3D materials are beyond the nanorange (>100 nm). This category of nanomaterials includes foams, honeycombs, fibers and nanotubes, layer skeletons, powdered nanoparticles, and layered composites (*Pokropivny* and *Skorokhod*, *2007*). With respect to the presence of features at the nanoscale, 3D materials can contain dispersions of nanoparticles, bundles of nanowires and nanotubes as well as multi-nanolayers (*Tiwari, et al., 2012* and *Teo, et al., 2007*).

1.2.3 Classification According to Composition

Nanomaterials can also be divided, depending on their composition, into three groups as inorganic, organic, or inorganic-organic hybrid. These classifications are based on the main elements containing nanomaterials namely carbon, silicon, metal, etc as (*Karak, 2019*) (Figure I.2). Organic nanomaterials are composed of carbon-based nanomaterials such as fullerenes, carbon nanotubes, single-walled carbon nanotubes, multi-walled carbon nanotubes, graphite, and nanofibers. Inorganics nanomaterials consist of metals, nanogold such as gold and silver nanomaterials and the metal oxide-

based nanomaterials such as titanium dioxide (TiO_2) and zinc oxide (ZnO) nanomaterials. Quantum dots (nanomaterials metalloid) are also inorganic nanomaterials. The third group is called hybrid nanomaterials that are defined as unique chemical conjugates of organic and/or inorganic materials (*Gómez-Romero, et al., 2005*). That is, these are mixtures of two or more inorganic components, two or more organic components, or at least one of both types of components. It is a combination of organic-organic nanomaterials, organic-inorganic nanomaterials, and inorganic-inorganic nanomaterials (*Al-Kayiem, et al., 2013*).

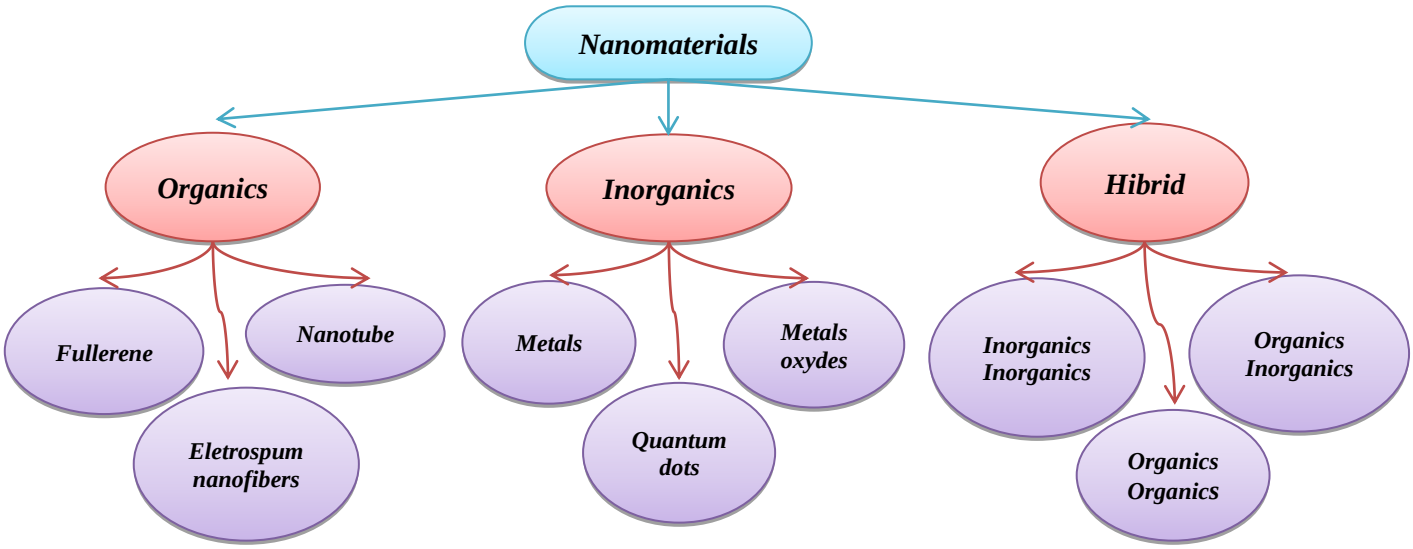

Figure I.2: *Classification of nanomaterials based on composition.*

I.3 Properties of Nanomaterials

I.3.1 Origin of New Properties

Because of their very fine grain sizes, nanomaterials have the structural features in between atoms in comparison of those in their bulk counterparts and conventional coarse grained polycrystalline materials which give them different properties. Nanomaterials can be produced with outstanding chemical, physical, magnetic, electrical, optical, mechanical, biological and catalytic properties that are substantially different from materials of a coarser structure, even when the elemental or molecular composition is the same. The nanomaterial properties can be tuned as desired via precisely controlling the size (distribution and morphology), shape, synthesis conditions, and appropriate functionalization.

I.3.2 Nanomaterials Composition

A ‘hard-sphere’ two-dimensional model proposed by Gleiter (*Gleiter, 1995* and *2000*) for a nanocrystalline solid, in which atoms in the crystalline region are indicated as black circles, while those in the boundary regions are represented as open circles (Figure I.3). Two different structures of atoms can be distinguished: crystal atoms with the nearest neighbor configuration corresponding to the lattice and boundary atoms with a wide variety of interatomic spacing. In the boundary regions, the coordination between the nearest neighbor atoms deviates or reduces from the one in the crystallites, implying the occurrence of atomic disorder at these regions *(Eastman, 1992* and *Loffler, et al., 1995).* It has become apparent that the total inter crystalline region consisting of grain boundaries and triple junctions (intersection lines of three or more adjoining crystals) become an important component of the microstructure at very small grain sizes *(Suryanarayana, 1995).*

The concept of grain boundary ledges sources for dislocations under an applied stress or fluctuation of temperature was recognized by Li (*1963*). Li proposed the emission of dislocations from grain boundary ledges and assumed that the density of ledges is about the same in the grain boundary, so the dislocation density scales inversely with grain size which implies that fine-grained materials have a greater dislocation density when they yield. Crystal growth often occurs at growth ledges, which can be associated with dislocations and their impact on crystal properties (*Lagerlof, 2018*).

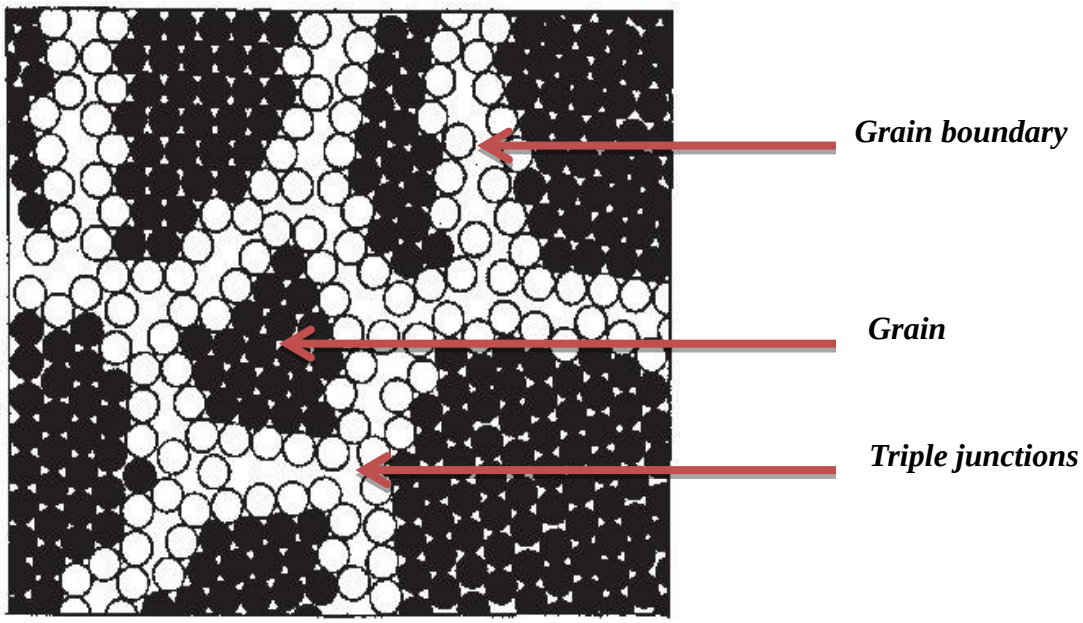

Figure I.3: *Two-dimensional model of nanomaterial (Gleiter, 2000).*

I.3.3 Chemical Properties

The chemical properties are important factors in nanomaterials. Those properties include stability and sensitivity, toxicity, corrosive and anti-corrosive, oxidation, reduction, composition, presence of biochemical moieties on surface (peripheral coatings or functional groups), hydrophilic or hydrophobic nature, aggregation and disinfection which determine the role of nanomaterials in chemical and biomedical engineering (*Nel, et al., 2006* and *Singh, et al., 2020*). In addition, morphology has an exceptional effect on the chemical properties of nanomaterials. The latter also depends on the size of nanomaterials which affect the appearance in interaction change during chemical processes. The reaction speed for a large number of heterogeneous chemical processes with the participation of solid phases is determined by diffusion in hard materials. This is related to the decrease in particle size, and the exponential grow of reaction speed (*Abdullaeva, 2017*). The larger numbers of atoms on nanomaterial surfaces is the main cause of the change in nanomaterials behavior and results in higher average energy than longer structures (*Singh, et al., 2020*), and therefore nanomaterials show more reactivity than bulk materials. Surface atoms are more active as compared with bulk atoms owing to fewer adjacent coordinate atoms or more dangling bonds (*Burda, et al., 2005*). The surface atoms are not fully bonded on all sides, and therefore have one or more dangling bonds. Consequently, less energy is required to break the chemical bonds in their chemical reaction (*Kuo, et al., 2003*). A nanoparticle can burn and release energy much more easily due to their large surface area to volume ratio and short oxidizer diffusion length.

I.3.4 Physical Properties

Between the dimensions on an atomic scale and the normal dimensions, which characterize bulk material, is a size range where condensed matter exhibits some remarkable specific properties that may be remarkable different from the physical properties of bulk materials such as grain boundaries, triple junctions and declinations. Physical properties of nanomaterials are related to different origins: large fraction of surface atoms, large surface energy, spatial confinement, and reduced imperfections. Surface effects are inversely proportional to material, leading to a smooth scaling of physical properties due to an increased fraction of the atoms at the particle surface compared to its interior.

Some examples of the physical properties of nanomaterials are:

- Colored nanomaterials of yellow gold and gray silicon are red in color.
- Gold nanoparticles (of 2.5 nm size) melt at much lower temperatures (~300 °C) than the gold slabs (1064 °C).
- Zinc oxide particles have been found to have superior UV blocking properties compared with their bulk substitutes.

- The absorption of solar radiation in photovoltaic cells is much higher in nanoparticles than in thin films of continuous sheets of bulk materials. Since the particles are smaller, they absorb greater amount of solar radiation.

I.3.5 Structural Properties

The crystalline structure is of a paramount importance in deciding a nanomaterial's properties. Nanomaterials with different crystal structures may differ in important physicochemical properties, such as reactivity or photocatalytic activity. Accordingly, the same material in a different crystalline form can have very different properties and in such cases only a specific crystal structure is used for given applications. The different crystal structures are not only relevant to the various technical applications, but can also affect the behavior and toxicity of nanomaterials.

As the grain size decreases, there is a significant increase in the volume fraction of grain boundaries or interfaces. This is mainly due to the nanometer size of the materials which render them with very high surface-to-volume ratio and large fractions of surface atoms. This characteristic strongly influences the different properties of the material. The size limitation introduces the high population of atoms located on the surface area. Exceptionally high surface areas can be achieved through the rational design of nanomaterials, and this property is associated with all nanomaterials (*Tomar, et al., 2020*). In addition, as the particle size decreases the number of molecules in the surface relative to the bulk increases, giving new and unexpected properties. Furthermore, the surface is related to many phenomena such as the effects of catalysis, absorption and chemical reactivity. Moreover, the surface atoms may have crystallographic structures, chemical bonds and mechanical behavior different from those on the core. The atoms proportion increases with the reduction of the particle size. This has been schematically illustrated in Figure I.4. In a micro-sized particle, only 2 % of atoms are different from those presented in the core. On the other hand, in a particle with a diameter of 60 nm, 4 % of their atoms are different. 50 % of atoms are different for a size of 5 nm, and 80 % difference is found in 1 nm particles (*LeMercier, 2019*). As a result, the properties of nanomaterials are drastically affected.

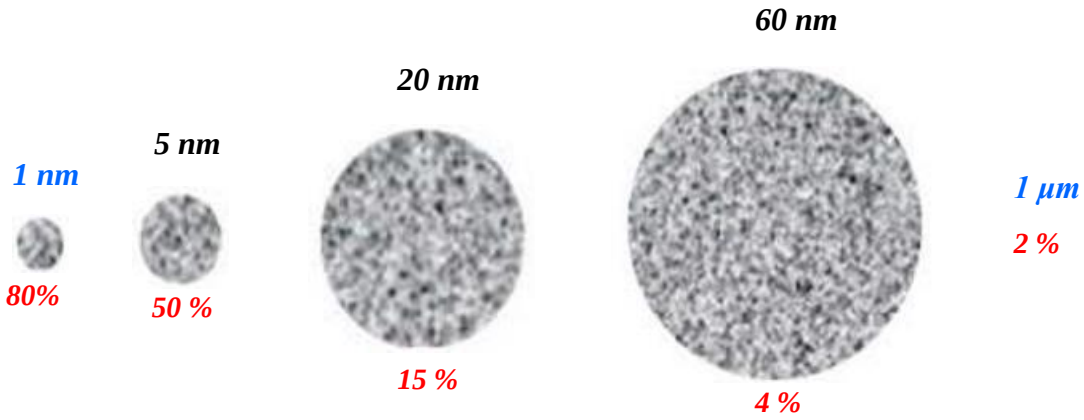

Figure I.4: *Variation, at the nanometirc scale, of the surface atoms proportion with the size of the particle (Le Mercier, 2019).*

I.3.6 Mechanical Properties

Nanomaterials have excellent mechanical properties and unique properties that are not found in macroscopic materials due to the volume, surface and quantum effects of nanoparticles. The mechanical properties of nanomaterials are affected by the triple junctions, the pores and the impurities. Moreover, several factors including the surface structure, functionalization, preparation methods, chemical treatments, etc have a direct influence on the mechanical properties, which also vary with the base material. Compared with their bulk counterparts, the mechanical properties of nanomaterials are considerably improved due to increases in crystal perfection or reductions in crystallographic defects (*Tomar, et al., 2020*). These properties refer to the mechanical characteristics of nanomaterials under different environments and various external loads. The mechanical properties, which reflect the internal bonds between the molecules and atoms of a material, are namely elasticity, toughness, hardness, ductility and superplasticity. These exceptional mechanical properties are closely linked to the gradient nanostructures of materials. Some fundamental mechanical properties are briefly discussed in the next sections.

I.3.6.1 Elastic Properties

In the years around 1950, two effects of size were identified in the strength of materials; both can be summarised as “smaller is stronger”. The elastic constant of nanomaterials is proportional to the bond strength between atoms or molecules and has been found to be reduced by 30% or less. The higher the bond strength, the higher the melting point and the lesser elastic modulus. If the temperature is increased, the mean separation between atoms increases and the elastic modulus decreases. The reduction in Young's modulus values could be related to the level of porosity and the state of cracks in

the samples. The most significant change resulting from a reduction in the grain size to the nanometer level is a 4-5 times increase in the strength and hardness over the course grained material.

Nanomaterials show an increase in yield strength (or hardness), σ (L), with a reduction in grain size, L, of a material decreases the free motion distance of dislocations by a reduction in obstacle spacing according to the well-known Hall–Petch (H–P) equation *(Hall, 1951* and *Petch, 1953)*. Hall (1951) and Petch (1953) found that the strength of iron and steel increases when the grain size is smaller. Eshelby, et al. (1951) established experimentally the eponymous relationship, based on the theoretical work, which holds well up to a grain size of 100 nm:

$$\sigma(L)= \sigma_0 + \frac{k_{HP}}{\sqrt{L}} \qquad (I.1)$$

σ(L) is the stress at yield or the flow stress at higher plastic strains, also called the elastic limit (or hardness). σ_0 is the friction stress resisting the motion of gliding dislocation (or the hardness of a single crystal specimen, d $\rightarrow\infty$). L is the grain size and k_{HP} is a constant called the Hall-Petch intensity parameter that may be predicted by theory or may be considered as a material constant.

Accordingly, nanomaterials are expected to show much higher yield strength than the coarse grained materials of the same composition. The hardness of nanomaterials is dependent upon the grain size for a particular range of temperature. It is about five times greater than their bulk counterparts.

1.3.6.2 Ductility

Ductility is one of the most important mechanical properties for structural materials. Good ductility is essential to avoid catastrophic failure in load-bearing applications and is also very important for many shaping and forming operations. By definition, ductility can be considered as the ability of solid materials to change their shape and deform plastically under tensile stress *(Zhu* and *Wu, 2018)*. Quantitatively, ductility is usually measured as the elongation to failure of a sample during standard uniaxial tensile tests *(Zhu and Wu, 2018)*. Uniform elongation is a better measure of ductility for small samples because they are less sensitive to sample size. Usually a reduction in grain size leads to an increase in ductility. Thus one should expect a ductility increase as the grain size is reduced to nanoscale. Nevertheless, the large increases in yield stress (hardness) observed in nanomaterials suggest that fracture stress can be lower than yield stress and therefore results in reduced ductility. Nanomaterials in most cases usually have very poor ductility, due to their low strain hardening capability *(Zhao* and *Liao, 2010)*. Increasing strain hardening rate via modifying microstructure is the primary route to improve ductility. Furthermore, the low ductility of nanostructured materials can be classified into two groups: extrinsic processing artifacts and intrinsic microstructures/deformation

mechanisms. The former case includes porosity, insufficient bonding, impurities etc that may develop during consolidation and/or synthesis of nanomaterials.

I.3.6.3 Superplasticity

The interest in superplasticity has increased due to the recent observations of this phenomenon in a wide range of materials, including nanomaterials. Superplasticity was described broadly as the ability of a material to exhibit, in a generally isotropic manner, very high tensile elongations prior to failure. Typically, elongations of 100% to >1000% are considered the defining features of this phenomenon. Superplasticity is a well-established grain size dependent phenomenon that is exhibited by fine grained materials at elevated temperatures. In the superplastic deformation regime, the dominating effect is sliding at grain boundaries, in which grains move over distances close to or greater than the grain size, without major change in their geometry. The grain boundary sliding is the dominant mechanism for structural superplasticity which leads to stress concentration at the grain boundary triple junctions *(Mukherjee, 1993).* This sliding is accommodated by dislocation or diffusional processes. The nanomaterials show superplasticity at significantly lower temperatures as well as at enhanced strain rates as grain size is decreased.

I.3.7 Thermal Properties

The thermal properties of nanomaterials are better than their fluid forms because they have a large surface area and so heat transfer occurs directly on the surface of the material. Surface affects result in reduced melting points of nanomaterials (*Shukla, 2017*). The specific heat and melting temperature are considered as the most fundamental thermal properties of any solid. Those properties depend upon many factors that usually are insignificant in bulk materials. In particular, surface properties, interfacial structures, and quantum or classical size effects prominently determine the thermal transport in nanomaterials, leading to carrier scatterings and localization that are otherwise absent or unobvious in bulk materials. Generally, nanomaterials exhibit enhanced specific heat and lower melting points (*Koper, et al., 2001*). The specific heat of a material is closely related to its vibrational and configurational entropy, which is significantly affected by the nearest-neighbour configurations. Thus, the increase in the specific heat of nanomaterials has been attributed to the small crystal size *(Suryanarayana, 1995).* The melting point is the temperature above which the crystalline structure of solids disappears and bereplaced by disordered atomic arrangement in liquids (*Koper, et al., 2001*). The decrease in bonding energy due to enhanced surface and grain boundary area in nanomaterials can reduce the enthalpy of fusion and the melting temperature (*Murty, et al., 2013*). In this model, the mean-square atom displacement averaged over the entire volume of the particle, including its surface was evaluated. As the particle decreases, the increased number of surface atoms

enhances the average values of atomic displacement. According to the second law of thermodynamics, entropy rate is positive for a system that is large with a longer timescale. However, smaller systems with smaller timescales violate this law according to the fluctuation theorem which has been proved experimentally (*Tahir, et al., 2021*).

I.3.8 Magnetic Properties

I.3.8.1 Magnetism and Magnetic Materials

Moving electrical charges generate a magnetic field in a material. Magnetism is therefore a characteristic property of all materials that contain electrically charged particles and often considered to be the origin of electronics. The origin of magnetism lies in the orbital and spin motions of electrons and their interactations with one another. Orbital and spin magnetic moments are invaluable fundamental quantities for understanding the macroscopic magnetic properties of matters. The spin magnetic moment is due to the precession of the electrons about their own axes whereas the orbital magnetic moment is due to the motion of electrons around the nucleus (Figure I.5). The resultant combination of the spin and orbital magnetic moments of the constituent atoms of a material gives rise to the observed magnetic properties. In general, the total dipole magnetic moment of all electrons in a material is zero because all electrons exist in pairs with opposite spins. Only those materials with partially filled shells generate a net magnetic moment, from which we can observe a macroscopic magnetic field.

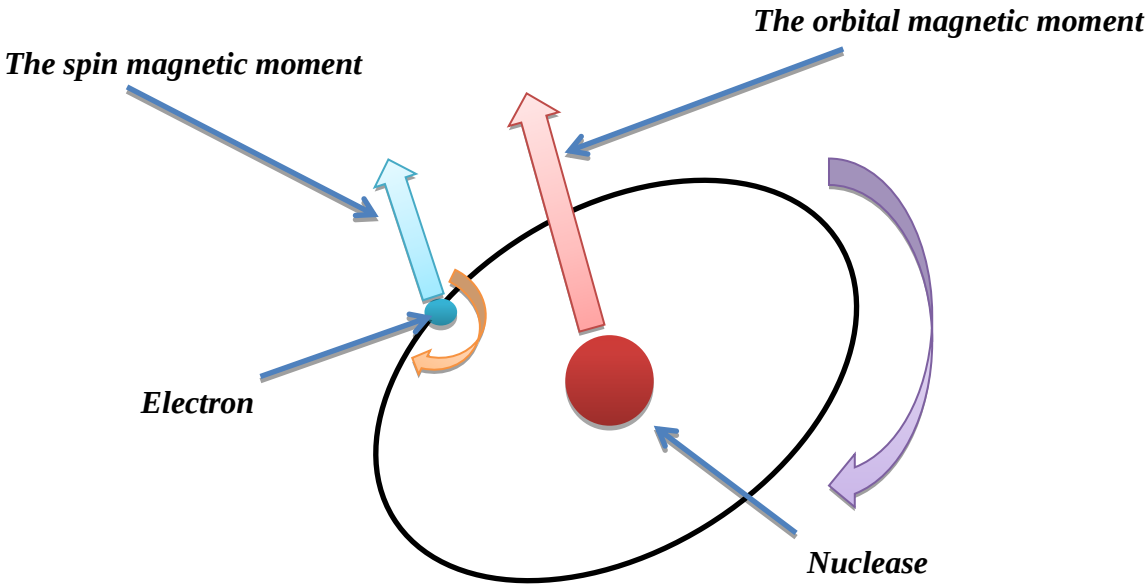

Figure I.5: *Orbital and spin magnetic moments.*

Magnetic materials are characterized by their magnetic fields. The magnetization M is induced by the external magnetic field H. The former is related to the latter by magnetic susceptibility χ. That is:

$$\vec{M} = \chi \vec{H} \qquad (I.2)$$

$\vec{M}$ is magnetization (total magnetic moment per unit volume), χ is magnetic susceptibility and $\vec{H}$ magnetic field strength.

The term "magnetic field" is commonly used to refer to the magnetic field strength $\vec{H}$ and to the magnetic induction $\vec{B}$. In vacuum, both quantities are linearly related via the magnetic permeability of free space μ_0.

$$\vec{B} = \mu_0 \vec{H} \qquad (I.3)$$

If the magnetic induction occurs within a material, the magnetization of the material is also considered:

$$\vec{B} = \mu_0 (\vec{H} + \vec{M}) = \mu_0 (1+ \chi) \vec{H} = \mu_0 \mu_r \vec{H} \qquad (I.4)$$

μ_r is the relative permeability of the material.

The moment of magnetic solids nearly originates from the partly filled inner electron shells of transition-metal atoms. Of a particular importance are the rare-earth or 4f elements, such as Nd, Sm, Gd and Dy, and transition-metal elements (3d elements) Co, Fe and Ni. These magnetic intermetallic compounds have several key properties divided into two categories: the intrinsic properties (dependent on the chemical composition) and the extrinsic properties (dependent on the microstructure). The intrinsic properties are the saturation magnetization, the Curie temperature, and the magnetocrystalline anisotropy. They are expressed on an atomic length and time scales but describe infinite crystals. These properties are determined by the crystallographic structure and the chemical composition of materials, and are generally considered as equilibrium properties. By contrast, the extrinsic magnetic properties are the coercivity and the remanent magnetization, which are mainly a function of the microstructure of the material. The extrinsic behavior reflects the magnet's real-structure (morphology) (*Skomski* and *Sellmyer, 2008*). By comparison, intrinsic properties tend to approach their bulk values on fairly small length scales and in the case of extrinsic properties, nanostructural effects are important on much larger distances (typically at least several nm). Intrinsic properties are not affected by small concentrations of defects whereas extrinsic ones show, in general, nonequilibrium behavious, closely related to magnetic hysteresis.

I.3.8.1.1 Classification of Magnetic Materials

All Materials can be classified at room temperature in terms of their magnetic behavior falling into one of five major groups, according to their susceptibility and permeability, into diamagnetic, paramagnetic, ferromagnetic, antiferromagnetic and ferrimagnetic materials (*Culity, et al., 2009*), as depicted in Figure I.5. Diamagnetism and paramagnetism do not exhibit magnetic properties or collective magnetic interactions. The other three types exhibit long range magnetic order below a critical temperature. The Curie temperature, T_C is the critical temperature in the case of ferromagnetic and ferrimagnetic materials, above which the magnetism is disordered and the materials exhibit paramagnetism. Similarly, the Neel temperature, T_N is the critical temperature for anti-ferromagnetic materials above which the materials become paramagnetic. This transition occurs due to thermal energy overcoming the electronic interaction in magnetic materials (*Moskowitz 1991*).

Diamagnetism is the weakest form of magnetism where the magnetization is proportional to the applied magnetic field. In a diamagnetic materials, electron shells are completely filled and therefore no dipoles are formed because the applied magnetic field is cancelled out (Figure I.6a).

The materials which are not strongly attracted to a magnet are known as paramagnetic materials. They have individual atomic dipoles oriented in a random fashion as shown in Figure I.6b. In this class of materials, some of the atoms or ions in the materials have a net magnetic moment due to the unpaired electrons in partially filled orbitals. However, the individual magnetic moments do not interact magnetically, and like diamagnetism, the magnetization ceases when the field is removed.

The materials which are strongly attracted by a magnetic field or magnets are known as ferromagnetic materials. Ferromagnetism is only possible when atoms are arranged in a lattice and the atomic magnetic moments can interact in order to align parallel to each other. Furthermore, ferromagnetic materials exhibit parallel alignment of moments resulting in a large net magnetization even in the absence of a magnetic field (Figure I.6c).

If the sublattice moments are exactly equal but opposite, the net moment is zero (Figure I.5d). This type of magnetic ordering is called antiferromagnetism. Antiferromagnetic materials are similar to ferrimagnetic materials. However, the magnetization of the two opposite sublattices is equal in magnitude. As a result, the magnetization of one cancels out that of the other and there in no net magnetization in the material.

Ferrimagnetism is only observed in compounds, which have more complex crystal structures than pure elements. These materials are similar to ferromagnetic substances; however they have two

sublattices which are magnetized in opposite directions. One of the sublattices has a stronger magnetization and hence a net magnetization in the material sample is achieved (Figure I.6e).

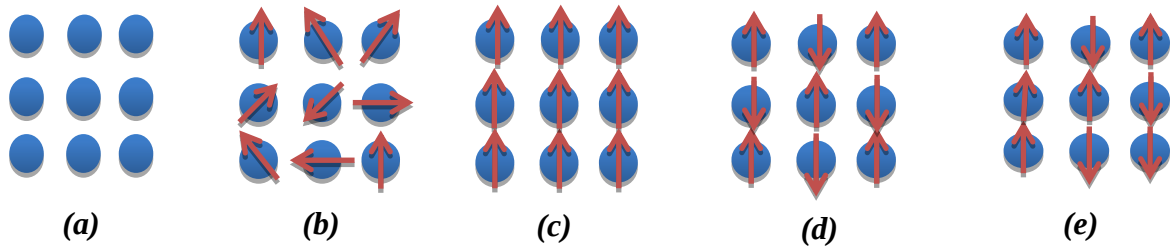

Figure I.6: *Different types of magnetism* ***(a)*** *Diamagnetism,* ***(b)*** *Paramagnetism,* ***(c)*** *Ferromagnetism,* ***(d)*** *Antiferromagnetism and* ***(e)*** *Ferrimagnetism.*

I.3.8.1.2 Magnetic Domains

In the year 1907, Pierre Weiss stated that a ferromagnet possesses a number of small regions (Magnetic domains) (*Weiss, 1907*). Each of them exhibits the saturation magnetization. The formation of the magnetic domains is energetically favorable because this structure can lower the magnetostatic energy originating from the dipole–dipole interaction. The directions of magnetization of neighboring domains are not parallel. As a result, between two neighboring domains, there is a region in which the direction of magnetic moments gradually changes. This transition region is called a magnetic domain wall. The domain walls can be distinguished according to the angle of the magnetization between two surrounding domains with the wall as a boundary of a 180° wall and a 90° wall. A 180° domain wall represents the boundary between two domains with opposite magnetization (Figure I.7a). A 90° domain wall represents the boundary between two domains with the magnetizations being perpendicular to each other (Figure I.7b).

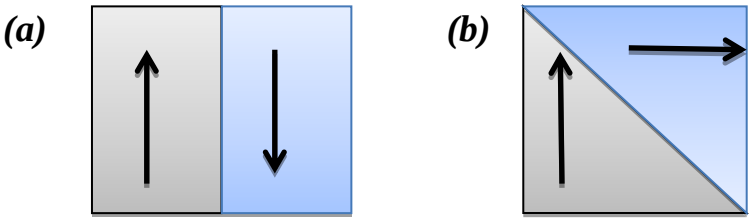

Figure I.7: ***(a)*** *180◦ and* ***(b)*** *90◦ domain wall.*

A closer inspection of 180° domain walls reveals that they can be divided into two classes; Bloch wall and Néel wall. In Bloch wall, the rotation of the magnetization occurs in a plane parallel to the plane of the domain wall (Figure I.8a). On the other hand, in Néel wall the rotation of the magnetization vector takes place in a plane perpendicular to the plane of the domain wall (Figure I.8b).

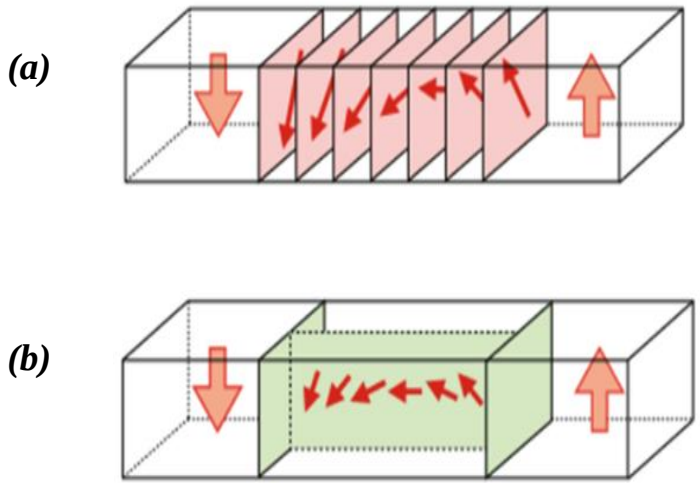

Figure I.8: *Rotation of the magnetization in a* ***(a)*** *Bloch wall and* ***(b)*** *Néel wall (Li-cong, et al., 2018).*

I.3.8.1.3 Magnetization Hysteresis Loop

Magnetic hysteresis is an irreversible phenomenon that represents the magnetization and demagnetization of any magnetic material where the basic magnetic properties of those materials are explained on the hysteresis loop curve (magnetization vs field), as shown in Figure I.9. All the magnetic properties determined from the hysteresis loop are detailed in the following lines.

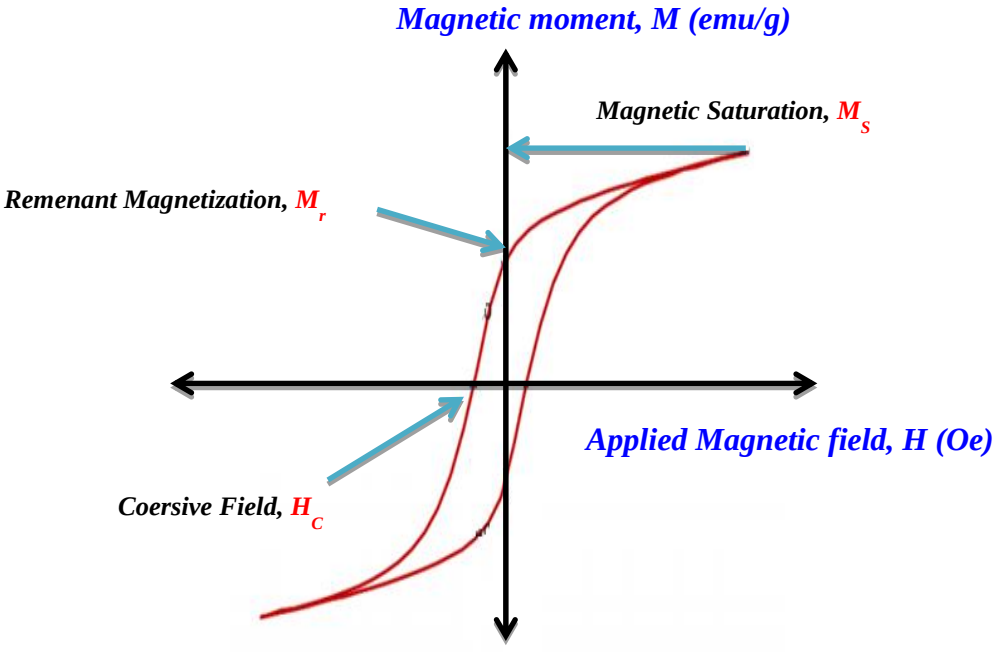

Figure I.9: *Magnetization hysteresis loop of a ferromagnetic material.*

Magnetic properties determined from the hysteresis loop:

- Saturation magnetization, M_S: It is the measure of the maximum magnetization in the material at sufficiently large fields where all the magnetic moments are aligned in the direction of the field, as depicted in Figure I.9.
- Coercivity, H_C: It is the magnitude of the field that must be applied in the negative direction to bring the magnetization of the sample back to zero (*Stefanita, 2012* and *Goldman, 2006*), as illustrated in Figure I.9.
- Remanent magnetization or retentivity, M_r: It is the measure of the amount of magnetization remaining in the material when the magnetic field is reduced to zero after reaching saturation, as shown in Figure I.9.
- Squareness, M_r/M_S: It is given by the ratio of retentively over magnetization saturation which is characteristic of in homogeneity of the material and the corresponding mobility of the domain walls.

According to the nature of the hysteresis loop, magnetic materials can be categorized into two main groups depending on how easy they are to magnetize; they can either be soft magnetic materials or hard magnetic materials (permanent magnets). Both types of magnetic materials are distinguished from their magnetic properties, especially their coercivity, H_c. Coercivity of a soft magnet is lower than that of a hard one (*Jiles, 2016*). A hard magnetic material is difficult to magnetize and demagnetize, whereas a soft magnetic material can easily be magnetized and demagnetized. As shown in Figure I.10, hard intermetallics are characterized by their wide hysteresis. They are used as permanent magnets, while soft ones with a very narrow hysteresis are utilized in electromagnetic machines (*Coey, 1991* and *2020*).

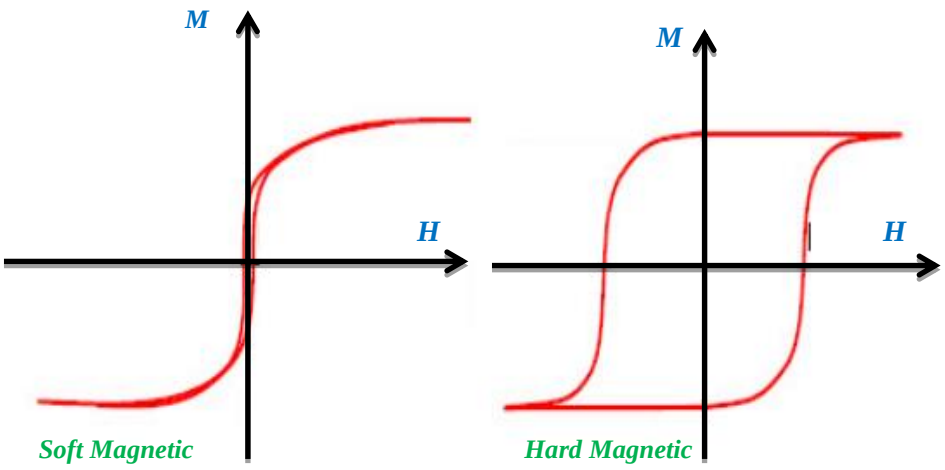

Figure I.10: *Hysteresis curve of soft and hard magnetic materials.*

The saturation magnetization, M_s, is the maximum magnetic moment per unit volume for a magnetic material. In general, M_s is insensitive to the microstructure and strongly relies on the chemical composition of the material (*Bozorth, 1978*). Coercivity, H_c is the strength of the applied reverse magnetic field that causes a reduction, in the magnetic induction, to zero. Coercivity is microstructure sensitive, and therefore is affected by heat treatment or deformation (*Jiles, 2016*). The effect of grain size on coercivity is shown in Figure I.11. Thus, when the grain size is progressively refined, the magnetic "hardness" increases. For very small grains, a D^6 proportionality is found (where D is the grain size). The coercive field classically follows a 1/D dependence.

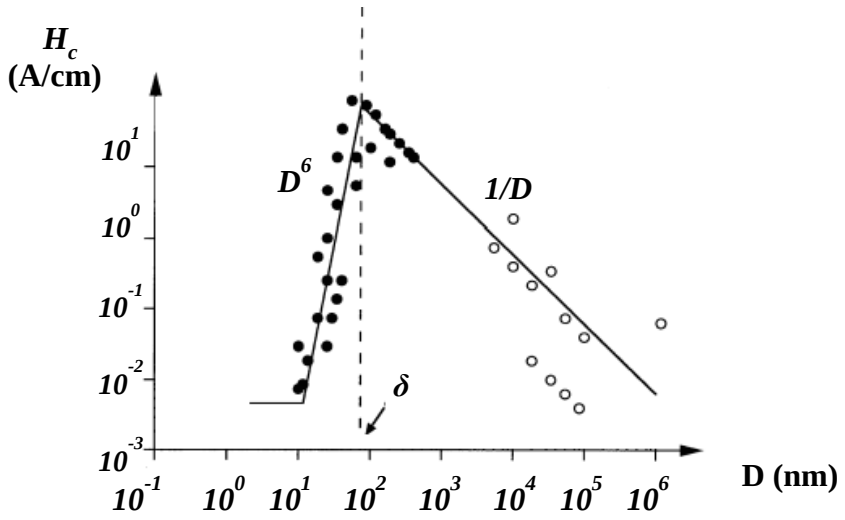

Figure I.11: *Grain size effects in magnetism (Arzt, 1998).*

I.3.8.2 Magnetic Behavior of Nanomaterials

The magnetic behavior of elements can change at the nanoscale where a non-magnetic element becomes magnetic at the nanoscale level (*Roduner, 2006*). At the nanometric scale the change in the magnetic properties becomes dramatic because of the effects related to the finite size (decreased volume), and the very important effect due to the surface. Indeed, the magnetic properties are strongly modified at the surface, where the atoms have a reduced coordination number. On the other hand, the magnetic state of the surface in nanocrystals plays a determinant role on the resulting magnetic properties, because the surface/volume ratio is high. Any material with a dimension less than 100 nm that responds on the magnetic field is considered a magnetic nanomaterial. The magnetic properties of nanomaterials are, as stated before, strongly altered compared with bulks. Gleiter, et al. (1989) found that the M_s value of pure nanocrystalline iron (130 emu/g) is lower than the M_s of polycristalline iron (220 emu/g). Quantum-size effects appear with a decrease in size; those effects involve the confinement of electrons within a very small nanoparticle, or a quantum dot which manifest in a quantized energy spectrum resulting in the appearance of magnetic moments, particularly in nanoparticles made of nonmagnetic materials in bulk form (*Shukla, 2017*). The first great advantage of

magnetic nanomaterials is that they have single-domain and therefore have large coercivities, allowing them to individually retain their magnetization directions (*Stoner* and *Wohlfarth, 1948*). Novel nanomagnetic materials are interesting from the point of view of the relationship between microstructural features and the unique magnetic properties observed at the nanoscale such as super paramagnetism, enhanced magnetic moment, high saturation field, shape anisotropy, etc.

I.4 Nanomaterial's Synthesis Process

A myriad of methods exist for fabricating nanomaterials with a higher degree of efficacy specifically tailored to the material to be produced. Generally, the fabrication of nanomaterials is considered to proceed and fall into two opposite, but complementary approaches. One is a top-down approach and the other is a bottom-up approach as shown in Figure I.12. These two different methods highlight the organization level of nanosystems as the crossing point hanging between the worlds of molecular objects and bulk materials (*Thangadurai, et al., 2020*).

I.4.1 Bottom-Up Approach

The bottom-up approach focuses on obtaining nanomaterials by building upon single atoms or molecules due to attractive chemical or physical forces (*Cai, et al., 2010* and *Chan, et al., 2011*). This approach has the potential to generate functional multicomponent devices by self-assemblying the atoms and molecules without wasting them or eliminating parts of the system (*Biswas, et al., 2012*). The chemical growth of nanometer-sized materials often implies colloidal or supramolecular systems and it frequently passes through phase transformations. In general, there are two basic methods utilizing the bottom-up approach, gas-phase synthesis and liquid-phase formation. Some of the methods used in bottom-up approach include plasma arcing, chemical vapor deposition process, metal organic decomposition, laser pyrolysis, molecular beam epitaxy, sol-gel method and wet synthesis.

I.4.2 Top-Down Approach

The top-down approach has been advanced by Richard Feynman and his coworkers of tencited 1959 lecture stating that "there is plenty of room at the bottom" and it is ideal for obtaining structures with long-range order and for making connections with macroscopic world. In this approach, micro and/or macro scale materials are broken down into nano-scale domains. In this approach, a bulk sample is manipulated to remove nanomaterials by either subtractive or additive methods, leaving behind the nano-sized structures (*Park, et al., 2009*; *Silva, 2004* and *Wang, et al., 2007*). A key advantage of the top-down approach is that the parts are both patterned and built in place, so that no further assembly steps are needed. This strategy is based on miniaturizing techniques including lithography, laser ablation, chemical etching, milling process, thermal decomposition, nanocontact printing, ion implantation, diffusion and deposition (*Chi, 2010* and *Kumar, et al., 2013*). Although this

approach has been playing a vital role in the elaboration of nanomaterials, it has several limitations such as the development of imperfections in processed materials, high cost (lithographic processes), requirement of high surface finished materials, and longer etching times (*Mijatovic, et al., 2005* and *Biswas, et al., 2012*).

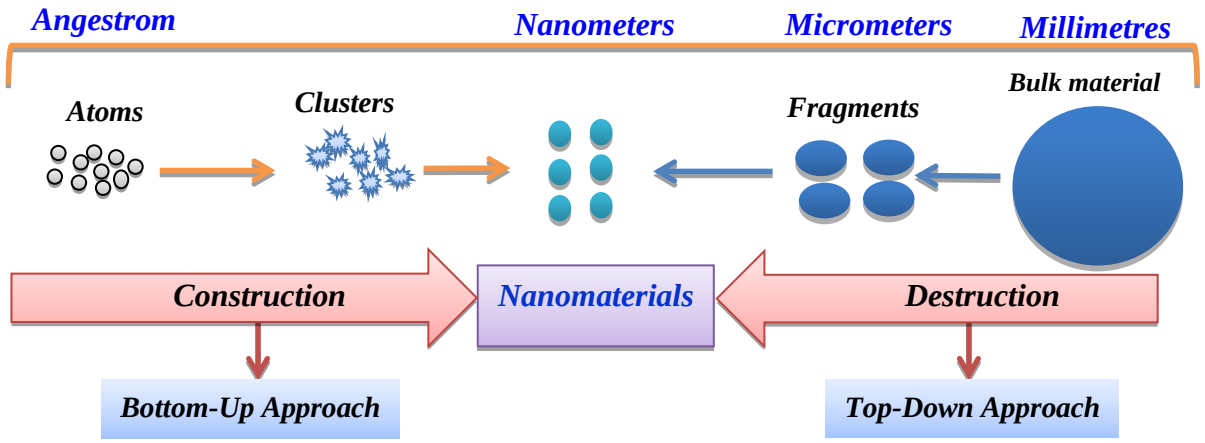

Figure I.12: *Schematic representation of the top-down and bottom-up approaches for the fabricaion of nanomaterials.*

I.4.2.1 Mechanical Milling

It has been well established that mechanical milling, also known as the mechanical alloying, is one of the best techniques for producing nanomaterials. It is widely regarded as one of the most efficient nanotechnology techniques for the top-down preparation approach. Mechanical milling is a well-known high energy process in which metallic powders involving repeated successive welding and fracturing the elemental powder mixtures at the atomic level which can induce chemical reactions and leads to the production of homogeneous alloys (*Gilman* and *Benjamin, 1983* and *Suryanarayana, 2001*). It is well confirmed that both welding and fracturing occur when metallic particles are ball milled, and that high energy ball mills may significantly expedite the grinding and fracturing processes. The repetition of all these events changes the particle size to the nano scale. This repetition also modifies the particles morphology and the evolution of the microstructure. This technique makes it possible to mix and combine solids ranging from micrometric scale of powder particles, while the crystallites are reduced to nanometric size, making it possible to obtain nanostructured materials (*El-Eskandarany, 2015*) (Figure I.13). This process was developed by John Benjamin and his coworkers at the International Nickel Company (INCO) in the late seventies. In the metallurgy field, mechanical milling refers to the solid state processes occurring at room temperature in which reactions between the fresh powder surfaces and the reactant materials occur (*El-eskandarany, 2001*). This method has a great advantage in the formation of various alloys which are difficult to prepare via any other synthesis method. It also demonstrates a high capability for the preparation of immiscible systems (*Fukunaga, et*

al., 1990). A variety of stable and metastable solid solutions, intermetallic phases, and amorphous alloys have been synthesized using this method in a number of alloy systems. The most important advantage of this technique compared with other alloying methods is the feasibility of the addition of alloying elements to improve the mechanical and physical properties of alloys.

Mechanical alloying diffusion is the main process during mechanical milling that leads to the formation of alloy phases. Diffusion is driven in any system by a decrease in the Gibbs free energy or chemical potential difference. The substitutional or interstitial mechanisms are the two major mechanisms by which atoms can diffuse through a solid, and both of them are referred to as lattice diffusions. Conventional solid-state reactions involve the formation of product phases between solid reactants that are mainly temperature dependent. Many factors on which the possibility and rate of a solid state reaction depend like the reaction conditions and the thermodynamic free energy change associated with the reaction (*West, 2007).* Furthermore, essential factors associated with the reactants are important in this type of reactions such as the structural properties of the reactants, their initial contact areas, and their reactivity (*West, 2007*). Additionally, the presence of structure defects in milled powders including dislocations, grain boundaries, stacking faults, vacancies, etc, enhance the diffusivity of solute elements in the matrix. Furthermore, the refined microstructural features decrease the diffusion distances. Moreover, the slight raise in temperature during ball-milling further aids the diffusion behavior, and consequently true alloying takes place amongst the constituent elements.

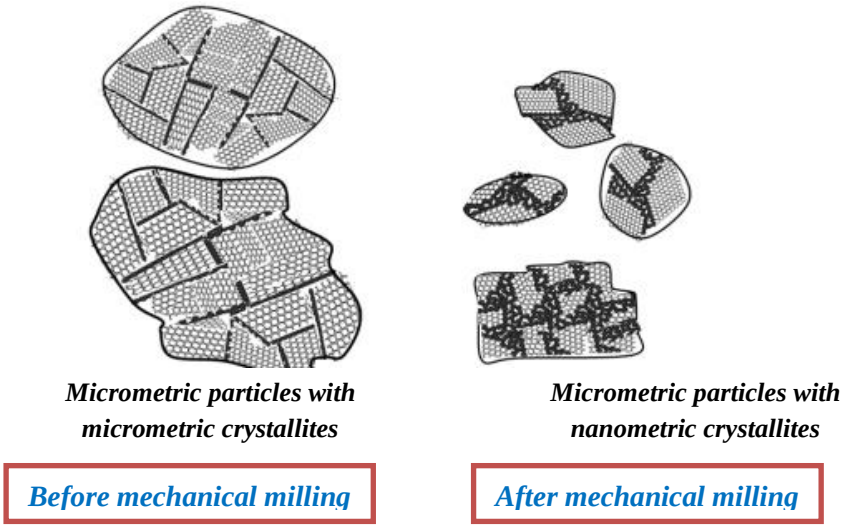

Figure I.13: *Schematic representation of the effect of the mechanical milling on particles and grain size (Bouchenafa, 2020).*

I.4.2.1.1 Historical Outline

Ball milling has evolved over the last five decades from a standard method in mineral dressing and powder metallurgy to its current prominence as a powerful process for the preparation of materials with improved physical and mechanical properties (*El-Eskandarany, et al., 2021*). Figure I.14 depicts a schematic history of the evolution of the mechanical alloying process since 1950.

Benjamin invented the mechanical process in the 1960s. The “Mechanical Alloying” phrase was introduced by Ewan C. MacQueen in a patent owned by INCO in the United States (*Benjamin, 1970)*. Benjamin and his coworkers used mechanical milling for the development of oxide particles (Al_2O_3, Y_2O_3, ThO_2) in nickel-base super alloys, opening a new field of research which drew much interest (*Benjamin, et al., 1974* ; *1977* and *1981* ; *Dai, et al., 2012* and *Wilcox, et al., 1974*). In mid-1966, researchers investigated the possibility of employing the mechanical milling technique and some useful alloys powder technology. They also proposed the ability of this method to coat the hardceramics phase (e.g., WC or ZrO_2) with a soft-metallic phase (Co or Ni) (*Lü, et al., 1998*). Mechanical alloying method has been utilized to fabricate a large variety of amorphous alloys since the fabrication of oxide dispersion strengthened alloys (ODS) ($Ni_{60}Nb_{40}$ amorphous alloy) (*Koch, et al., 1984).*

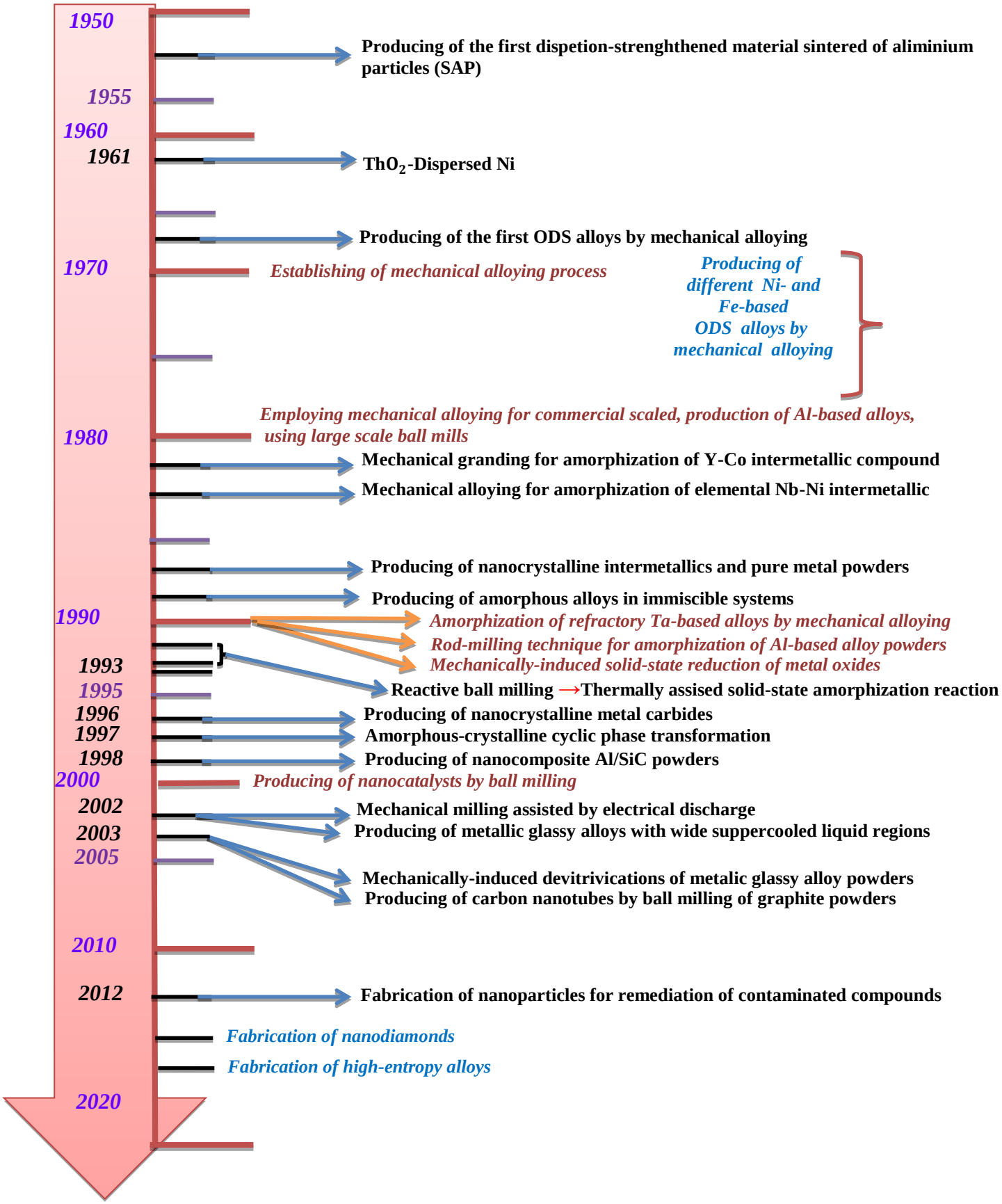

Figure I.14: *A timeline presentation displaying the evolution of mechanical milling since 1950, along with some instances of novel materials obtained by this method (El-Eskandarany, et al., 2021).*

I.4.2.1.2 Mechanical Milling Types

Various kinds of ball mills are depicted in Figure I.15. The principles of these operations are, however, the same for all such techniques. They can be divided into two categories based on their rotation speed: high energy ball mills, and low energy ball mills. Each type of mill is designed with a specific purpose, speed, time, substrate loading, and geometric parameters of the mill, which are potential factors in determining the dynamic energy. In fact, the type of ball mill used is determined by the milling goals.

- **High Energy Ball Mills**

The planetary ball mill involves the generation of both shear and impact forces (*Dash, et al., 2016*). This type of mills owes its name to the planet-like movement of vials. They are arranged on a clockwise rotating circular disc and an internal mechanism makes the milling jars rotate anticlockwise around their own axes at the same time (Figure I.15a). the milling jars and the supporting disc rotate in opposite directions with different speeds, bringing frictional and impact forces especially the effective centrifugal force to generate high dynamic energies.

The simple and effective type is known as the attrition mill or the attritor (also known as the stirred ball mill). In an attrition mill, a higher surface contact is ensured between balls and the powder because of horizontal impellers and a vertical rotating shaft. The cylinder itself is fixed (Figure I.15b).

Vibratory (or shaker) mills are commonly used for laboratory investigations and for screening purposes. While using a vibratory tube mill, a cylinder containing balls vibrates the sample at a high frequency and small amplitude to obtain high milling forces. In this case, the important factors are the vibrational frequency, the amplitude of vibration and the mass of the milling medium (Figure I.15c).

- **Low Energy Ball Mills**

The useful kinetic energy can be transferred to the powder particles of the reactant materials in this type of mill. The tumbler ball mill contains a cylinder with steel milling balls in which an axial rotation causes these balls to roll down and impact upon the powder charge (Figure I.15d). In this type of instrument, the efficiency of the process mainly depends on the diameter of the mill. Larger diameters allow greater height of the fall and consequently a higher energy is transmitted to the balls.

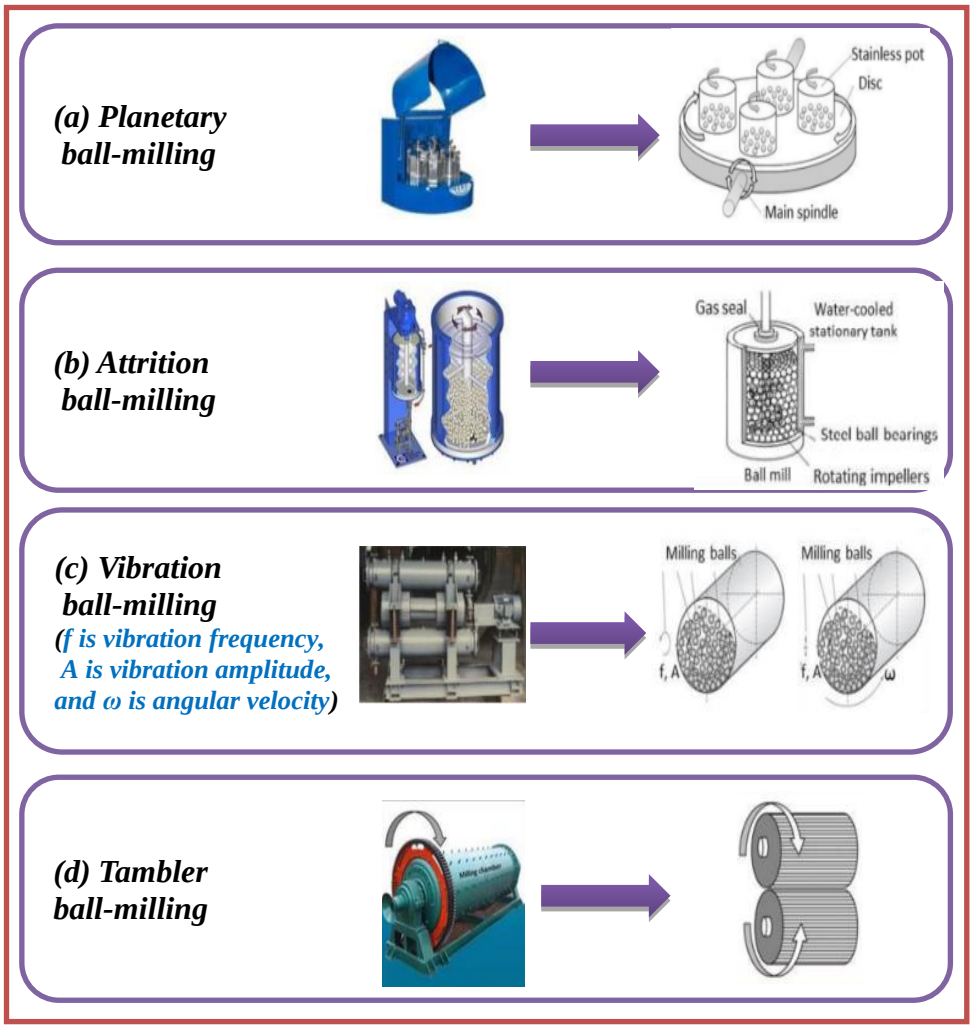

Figure I.15: *Different types of ball milling (Kumar, et al., 2020).*

I.4.2.1.3 Factors Affecting the Mechanical Milling Process

Mechanical alloying is impacted by a variety of parameters that are crucial in the manufacturing of homogeneous ultra-fine powders and hence involves optimizing a number of variables to achieve the desired product phase and/or microstructure. Some of the important parameters that have an effect on the properties of the final milled products include particle size distribution, degree of disorder or amorphization, final stoichiometry, type of mill, milling container, milling speed, duration of milling, ball-to-powder weight ratio (BPR), extent of filling the vial, milling atmosphere and milling temperature (*Suryanarayana, 2001* and *El-Eskandarany, et al., 2021*). Those different critical factors affecting the milling technique are discussed in the rest of this section.

Different types of ball milling grinder are used depending on the capacity of the mill, operation speed, temperature control and extent of minimizing contaminations during milling (*Suryanarayana, 2001)*. Cross contamination can be avoided using the same material for the milling jars and the milling

medium. It depends on each type of ball milling process. In principal, the higher the energy, the faster the product is obtained. The total mechanical energy transferred by the ball mill to the material is given by the following expression (*Dakiche, 2020*):

$$E_m = R\Omega\omega t \qquad (I.2)$$

With R being the ball to powder weight ratio, Ω the disc rotation speed, ω the vial rotation speed and t the milling time.

To obtain desirable results, the powder must be milled for as long as required. If the powder is milled longer than the required duration, unwanted contamination and phase transformation may occur (*Suryanarayana, 1995*). The required milling time for a particular sample can be determined based on parameters such as type of mill, ball to powder ratio, milling temperature and intensity.

In ball mill, increasing the rotation speed simultaneously increases the speed in which the ball moves. As a result, the ball is pinned and exerts no effects on the particle. Therefore, milling speeds should remain below this critical speed to keep the ball moving. Additionally, high speed results in high temperature that might contaminate the powder or re-crystallizes the nanoparticle.

Fine powder particles are produced due to impact forces exerted on these particles. To achieve this, the milling jar should be 50% filled and 50% empty to allow free movement of the milling ball and the powder particles in the jar. If the quantity of the ball and powder particles is large, there is not enough space for balls to move; ultimately the impact is less on powder particles.

The ball to powder weight ratio or charge ratio is one of the important variables for the milling operation (BPR = $\frac{\text{Balls wight}}{\text{Powder wight}}$). The higher BPR the shorter the time required. At high BPR, the collision of balls in the milling medium increases per unit time, producing more energy that leads to the phase transformation of the particles.

The temperature of the milling container depends on the characteristics of the milling powder mixture, milling jars and the kinetic energy of the ball. In the milling process, two types of temperature effects are usually taken into consideration. Firstly, local temperature arises due to the collision and friction of the ball. The rising temperature initiates the diffusivity and the defect concentration in the milling powder followed by phase transformation of the particle (*Suryanarayana, 2001*). Secondly, overall temperature in the milling container; during the mechanical alloying, one part of the powder is attached to the vial walls and the other part is attached to the balls, keeping the rest of the powder moving in free-state. All these three parts have different temperatures (*Suryanarayana, 2001*).

The milling atmosphere is one of the factors responsible for contaminating the milling powder. Generally, the milling chamber is evacuated or filled with inert gas such as argon or helium to avoid this contamination. Different atmospheres can be used in the milling media if particular effects are desired. Nitrogen, hydrogen and air have been used to produce nitrides, hydrides and oxides in the powder.

It should be noted that all these variables influence the milling process in different ways and are completely independent. For example, the optimum milling time depends on the type of mill, the grinding medium size, the milling temperature, the BPR, etc. However, other parameters have no significant effect on the final product obtained after milling (*Suryanarayana, 2001*). The more comprehensive the control and monitoring of the milling conditions, the better the end product is.

I.5 Applications of Nanomaterials in Healthcare

Nanomaterials exhibits outstanding physio-chemical properties such as biocompatibility, higher molar extinction coefficients, superior reactivity, reduced size, high surface to volume ratio, differential shape, well-ordered composition, meticulous surface coatings or functional groups, solubility, specific hydrophilic or hydrophobic nature and aggregation. These properties are important for better adsorption, cellular uptake, accumulation and biodistribution patterns, clearance mechanisms, tunable plasmonic properties, photo and magnetic properties, and quantum effects. Furthermore, in growing fields of material research at nanoscale, nanomaterials by virtue of their small size comparable to many biological molecules like proteins and viruses, open up a wide range of new opportunities and applications, such as diagnostic biosensors, drug and gene delivery, and biomedical imaging and sensing, to name a few (*Nath, et al., 2013* ; *Casalini*, et al*., 2019* and *Dong, et al., 2012*).

Nanomaterials generally come in direct contact with body tissues and cells, where they can cause positive or damaging effects on the body. The application of nanomaterials in the diagnosis and treatment of different diseases is known as nanomedicine. Generally, nanomaterials used in commercial applications are engineered nanomaterials produced using chemical, biological, and physical methods.

Genetic testing is focused on identifying chromosome, gene, or protein changes between healthy and diseased cells or persons. Genetic test outcomes can either verify or rule out possible genetic conditions and help determining whether a person is likely to develop or pass a genetic disorder. Nanomaterials offer a futuristic diagnosis platform for genetic diseases. Different nanomaterials have been developed and functionlized with the target molecules to provide therapeutic selectivety and molecular imaging (*Khan, 2020*).

The toxicity and the antibacterial activity performance, which provide a great platform to update physio-chemical properties of the materials, such as the chemical composition, size, shape, concentration and in particular particle aging, result in more promising agents against bacteria (*Hajipour, et al., 2012* and *Bardhan, et al., 2019*). Toxic nanomaterials, especially metallic nanomaterials and nanoparticles show distinguished toxicological properties in comparison to the larger micron-sized (bulk) form or solution of the same substance (*Yong, et al., 2010*). Therefore, toxic nanomaterials and nanoparticles should carefully be eliminated before being used on human patients (*Attarilar, et al., 2020*). This toxicity is more related to particle number and surface area than mass. The reduction in size may attenuate toxicity because the nanomaterial becomes electrochemically reactive and could enter the blood stream and translocate in cells, tissues and functional organelles (*Tucci, et al., 2013*). Several toxicological studies have indicated that nanomaterials are potentially harmful particles may alter and inhibit cell growth leading to various pathophysiological states in humans, animals and aquatic organisms (*Liu, 2022*). Most nanomaterials especially inorganic metals and metal oxides such as silver (Ag), zinc (Zn), copper (Cu), titanium (Ti), gold (Au) and iron (Fe) possess strong antibacterial activities in wound healing and related medical conditions. Nevertheless, not all the nanomaterials are toxic (*Oberdörster, et al., 2005*). The antibacterial effects of various nanomaterials are well known, however the exact mechanism for their bactericidal nature is still not clear. A number of mechanisms ranging from physical interactions with the microbial body to chemical disruptions of cells have been suggested (*Wang, et al., 2017* and *Godoy-Gallardo, et al., 2021*).

Great advances in biomedical sciences and nanotechnology would expand the entities of artificially organic and inorganic engineered nanomaterials for cancer therapeutic and diagnostic applications due to their unique characteristics of passive tumor targeting. Nanomedicine has made great strides, since the established conventional cancer therapies have not been able to overcome limits for safer and improved cancer diagnosis and therapy. For nanomedicine to succeed and have meaningful commercial impact, physical, biochemical, and physiological properties of nanomedicine carrying particles have to be understood, and how such nanomaterials and nanoparticles can be manufactured in a controlled and scalable manner for drug delivery and therapy (*Khan, 2020*). Nanomaterials used in cancer therapy can be classified into several main categories such as targeting cancer cells, tumor microenvironment, and immune systems. These nanomaterials have been modified for a wide range of cancer therapies to overcome toxicity and lack of specificity, enhance drug capacity as well as bioavailability (*Cheng, et al., 2021*). Additionally, they exhibit greater cellular uptake, prolonged circulation after surface modification, and more efficient access to targeted tumor sites, as compared with micron-sized particles. Furthermore, they can carry a large number of therapeutic drugs owing to their high surface-area-to-volume ratio, penetrate into the leaky tumor

vasculatures, and subsequently deliver the drug payloads to tumor tissues via the enhanced permeability and retention effect (*Bae, et al., 2011*). Inorganic nanomaterials are used to kill cancer cells due to specific cancer inhibition mechanisms such as enzyme inhibition, oxygen capture approaches from tumor sites, and the production of free radicals in the tumor microenvironment (*Adeel, et al., 2020*).

Magnetic nanomaterials are mainly used in magnetic resonance imaging (MRI). Guided by external magnetic fields, magnetic nanomaterials and nanoparticles loaded with chemical drugs can target cancer cells, and therefore reduce the side effects of conventional chemotherapy (*Zhu, et al., 2009*). Magnetic hyperthermia is a type of thermal treatment of cancer, which uses ferromagnetic nanomaterials and nanoparticles such as metallic particles, heated up to induce cancer cell death. Furthermore, the superparamagnetic behavior of nanomaterials provides several usages for cancer diagnosis and treatment. Superparamagnetic iron oxide nanoparticles has potential in cancer hyperthermia treatment due to its smaller size, higher targeting specificity, controllable releasing speed, and immune evasion capability (*Horst, et al., 2017*).

I.6 CoFe Based Alloys

FeCo based nanostructured materials have excellent soft magnetic properties with the highest saturation magnetization of any material, as well as high Curie temperatures, making such materials ideal for high-temperature applications. FeCo-based alloys (Fe-Co-Si-B-P) were formed by partial replacement of Fe by Co in Fe-Si-B-P alloy system. Good soft magnetic properties have high B_s approaching 1.75 T, an higher total ferromagnetic element content and bending ductility after stress relief annealing. Partial substitution of Co for Fe causes further increase in Curie temperature of the Fe-Si-B-P amorphous alloys (*Han, et al., 2017*). A modified polyol process has been used to synthesize FeCo alloy nanoparticles. The maximum saturation magnetization of 212 emu/g was recorded for both $Fe_{60}Co_{40}$ and $Fe_{75}Co_{25}$ particles with a coercivity of 200 Oe (*Huba,* et al., *2011*). Nanocrystalline $Fe_{100-x}Co_x$ (x = 20, 35, 50, 60) alloys have been prepared by mechanical alloying. Co dissolves into the Fe matrix and forms a disordered FeCo solid solution with equiaxed grains of about 8 nm in size upon 20h of milling. Both coercivity and saturation magnetization of the mixtures of Fe and Co increases with milling time, indicating an increasing homogeneity in the composition and phase formation. It is found that the saturation magnetization is also dependent on the Co content, which reached the highest value of 240 emu/g for $Fe_{65}Co_{35}$ (*Poudyal, et al., 2012*). A two-step electroless plating method was developed to control the morphology and grain size of FeCo films, to obtain excellent magnetic properties. Kim, et al. (2019) found that the best soft magnetic performance was exhibited by the micron-sized $Fe_{65}Co_{35}$ grain-embedded $Fe_{65}Co_{35}$ alloy. By altering the reaction temperature, large $Fe_{65}Co_{35}$ crystallites were first formed at a high plating temperature for high M_s

(237 emu/g); this was followed by filling the gaps between the crystallites with $Fe_{65}Co_{35}$ nanograins to retain a low H_c (31 Oe). More information about FeCo binary systems are given in the appendix.

I.7 Phosphides

The environment is rich in phosphorus (P). This vital element, contained in the human body, occupies 1% of the total body weight. It is named from the Greek word φωσφόρος (phosphoros) which means "bringer of light". It was discovered in 1669 by Hennig Brand, as the 13th element of the present periodic table. Phosphorus has one main isotope (*Kim, et al., 2011*), and shows extensive allotropy. The important allotropic forms of phosphorus are white phosphorus, red phosphorus, violet phosphorus, and black phosphorus (the thermodynamically stable form). To date, phosphorus is unique within the chemical elements; it is the sole element whose thermodynamic standard state is defined for the most instable allotrope, while the other modifications marked with negative standard enthalpy values (*Nilges, et al., 2018*). Red P is the most abundant and easily available allotrope of elemental phosphorus, (*Roth, et al., 1947* and *Ceppatelli, et al., 2013*). It is prepared from white phosphorus by a simple heating step to higher than 20°C (*Holleman, et al., 1995* and *DeWitt, et al., 1946*). It is polymeric and consists of chains of P_4 tetrahedra linked together. Red phosphorus has widely been used in our everyday life as safety matches (*Scheer, et al., 2010*), flame retardants (*Braun, et al., 2004*) and in chemical analysis (*Sladkova, et al., 2009*).

Phosphides, are a class of chemical compounds in which phosphorus is combined with a metal forming M_xP_y (M = Fe, Mn, Ni, Co, Cr). They have attracted a lot of attention thanks to their magnetic, electronic and catalytic propertie as well as their large field of applications (*Callejas, et al., 2016* ; *Dutta, et al., 2016* ; *Franco, et al., 2012* and *Oyama, 2003*). Among these P-based materials, red phosphorus was the first to attract researchers' attention due to its favorable properties. There are a number of ways to produce phosphides. The most general method is to heat stoichiometric amounts of the metal and red phosphorus to high temperature in an inert atmosphere or in a vacuum. Metal phosphides are an intriguingly diverse class of metal non-oxide materials and frequently have complex phase diagrams, with several stable phases at room temperature, that range from metal-rich to phosphorus-rich with 3d metals such as FeP_2, CoP_3, and CuP_2. They are well studied as electrocatalysts because they are synthetically accessible and usually require high temperatures near 1000°C (*Okamoto, 2010*). Other methods that can be used include electrolysis reactions, the reaction of a metal (or a metal halide or metal sulfide) with phosphine (PH_3), and the reduction of a metal phosphate with elemental carbon at an elevated temperature. Transition metal phosphides are an interesting class of materials and worth investigating on the nanoscale because of their wide scope of properties and applications. Those compounds have attracted growing interest, used as catalytic materials. This is because; metal-rich phosphides show excellent activity for hydrogenation reactions

(*Prins, et al., 2012*). Extensive studies have been carried out on FeP and CoP binary alloys and on ternary and quarterly alloys containing their three elements (Fe, Co and P).

I.7.1 Fe-P Based Alloys

Bensalema, et al. (2009) prepared nanostructured $Fe_{92}P_8$ (wt.%) powder mixture by mechanical alloying. They found that annealing at a temperature of 210°C for 30 min leads to the formation of FeP phosphide in addition to α-Fe(P) solid solution and Fe_3P nanophase. Tebib, et al. (2008) used high energy ball milling in a planetary ball mill (Fritsch P7) to prepare nanostructured Fe-8P (wt%) powder mixture where several phosphides Fe_2P, Fe_3P and FeP were obtained and two structure states of α-Fe(P) solid solution: α-Fe_1 and α-Fe_2 were confirmed by both XRD and ^{57}Fe Mössbauer spectrometry measurements. After milling for 21h, Tebib, et al. (2018) found the different heat treatments show that Fe_8P (wt.%) powder milled for 21h are not stable and their study leads to a conclusion that milling has a significant influence on the microstructure and thermal stability of powders. The black crystalline powder of FePy ($3 \leq y \leq 4$) is formed after high energy ball milling for 15h by reacting iron and red phosphorus powders in an inert atmosphere. Phase identification reveals that this product is composed of FeP_4, FeP_2 and FeP. Although there is a capacity loss during the 1st cycle associated with the electrode activation and SEI formation, the 2nd and 3rd discharge capacities can reach 1486 and 1436 mAh g^{-1}, respectively. A capacity of 1089 mAh.g^{-1} (~73.3% of the 2nd cycle capacity, 55% of the 1st cycle capacity) can be delivered after 10 cycles at a current density of 0.03 mA/cm^2, with the corresponding coulombic efficiency of ~97%. By adding fluoroethylene carbonate to the electrolyte, the cycling performance of this material can be improved (*Wang, et al., 2014*).

Dekhil, et al. (2015) obtained nanocrystalline Fe–6P–1.7C powders by mechanical alloying in a high energy planetary ball-mill P7. The Rietveld refinement of the X-ray diffraction pattern revealed the formation of disordered Fe(P) solid solutions and Fe_2P phosphide, after 9h of milling. On further milling (50h), Fe_3P and Fe(P,C) phases were formed when the total mixing of the elemental powders was achieved at the atomic level. They found that the crystallite size reduction down the nanometer scale (~9 nm) was accompanied by the introduction of internal strains up to 1.8%. Furthermore, the saturation magnetization and coercivity values were about 157.3 emu/g and 80 Oe, respectively, after 24h of milling (see the appendix for further details on Fe-P binary systems).

I.7.2 Co-P Based Alloys

Cobalt and cobalt based alloys have in recent years been considered as promising functional materials due to their magnetic and mechanical properties. Lucas, et al. (2005) prepared CoP alloys by electrodeposition method at room temperature. An increment in the coercivity of the alloys when the pH of the electrolyte decreases was reported, and can be related to hydrogen evolution during

electrodeposition. Hydrogen produces high internal stresses in the plated alloys, which cause problems with the adhesion of the films and an increase in the coercivity. High electrical conductive cobalt phosphide alloys are fabricated through a liquid phase process and a nanoparticles structure with a high surface area (*Zhang, et al., 2017*). A study by Modin, et al. (2014) showed that adding nickel to the CoP system results in the formation of a clearly manifested network structure and thus a less homogeneous distribution of chemical elements was achieved. Further studies prepared nanostructured CoP through an organic solvent-free low-temperature phosphidation reaction under argon atmosphere. Electrocatalytic properties towards the hydrogen evolution reaction in acidic media found that CoP nanowires produced the highest catalytic activity and stability (*Jiang, et al., 2014*). Phase's diagram of Co-P binary system and its transformations are given in the appendix.

I.8 Fe-Co-P Based Alloys

Pilar, et al. (2008) reported that $Fe_{60}Co_{20}P_{10}B_{10}$ nanocrystalline alloys, were produced after 5, 40 and 100h of milling by mechanical alloying. After 100h, the milled alloy primarily consisted of metastable *bcc* Fe(Co,Ni) nanocrystals (11–17nm) with different Fe-rich environments. The value for the apparent activation energy of the main crystallization processes was 2.4 ± 0.1 eV. Ferrophosphorus, a combination of phosphorus with iron, is used as an ingredient in high-strength low-alloy steel. Yolk–Shell structured FeP-C nanoboxes (FeP-CNBs) were synthesized through a phosphidation process by Yand, et al. (*2019*). The existence of the carbon shell can prevent the aggregation of FeP nanoparticles and enhance the conductivity of the composite, while the void space between the carbon shell and the FeP accommodates the volume expansion of FeP during charge–discharge without destroying the electrode microstructure. FeP-CNBs electrode has achieved high reversible capacity and superior rate performance (*Yang, et al., 2019*). The substitutional solid solution $Mn_{1-x}Fe_xP$ electrodes synthesized via high energy mechanical milling showed an enhanced electrochemical performance in terms of initial columbic efficiency, reversible specific capacities, cycle retention, and rate capability resulting from the beneficial combination of two end members (*Kim, et al., 2019*). Fe-Co-P ternary system's diagram is well detailed in the appendix.

Chapter II:

Materials and Experimental Methods

The main techniques, the experimental equipment used in the production, the application, the characterization and the techniques employed for analyzing the synthesized $Fe_{15}Co_2P_3$ nanostructured powders used in this thesis are explained in this chapter. Including the conditions for production of the powder mixtures by combination of elemental Fe, Co and red P pure powders through atomic diffusion during the mechanical alloying process high energy planetary ball mill like instrument of the preparation, the bacterial cell growth instruments, steps and methods, the X-ray diffraction and Fourier transform infrared are used to characterize our resulting powder mixtures; vibrating sample magnetometer is used to study the magnetic properties, ultraviolet–visible spectroscopy which is used in the bacteriological essays in this research.

II.1 Experimental Setup and Elaboration Conditions

II.1.1 Starting Materials

In this thesis, all chemicals were weighted with a sensitive balance in a glove box under an inert atmosphere without further treatment unless specified otherwise. Table II.1 gives detailed information on the purity and size of the elemental powders used in this study. Table A.1 in the appendix details the important properties of Fe, Co and P.

Table II.1: *Summary of elemental powders used in the elaboration of the mixture powders*

Element	***Average particle size***	***Physical***	***Powder Purity (%)***	***Company form***
Fe	-325 mesh	Dark grey powder	97%	Sigma-Aldrich
Co	<150 µm	Grey Powder	≥ 99.9%	Sigma-Aldrich
Red P	Amorphous	Red Powder	≥ 97.0%	Sigma-Aldrich

II.1.2 Principle of High Energy Ball Mill

Figure II.1, schematically presents the base principle of mechanical milling; that is the impact between the powder and the milling medium in a milling jar causes energy transfer which is responsible for the morphological and microstructural evolution (*Tjong* and *Chen, 2004*). This energy is released at the point of collision between balls as well as on the high grinding energy created by friction of balls on the wall. The balls may roll down the surface of the chamber in a series of parallel layers or they may fall freely and impact the powder and the balls beneath them (Figure II.1a) (*Baheti, et al., 2012*). In mechanical milling, the powders are loaded into a high energy ball mill. The synthesis of materials at low temperatures via ball milling is possible through a combination of multiple processes, which occur during milling. These processes include thermal shock, high-speed and plastic deformation subject to repeating two essential processes, cold welding between the different particles and fracturing of the cold welded particles due to high energy collision (Figure II.1b) (*Dadkhah, et al., 2019* and *Lu, et al., 1999*). Cold welding minimizes the diffusion distance between the atoms of the different components. The fracturing of the welded particles impedes the clustering of the particles promoting the transfer of high ball collision energy to all particles and produces new, clean surfaces without oxide layers accelerating the diffusion (*Gubicza, et al., 2004* and *Lu, et al., 1999*). When

the mill rotates, the balls are picked up by the mill wall and rotate around the wall due to the centrifugal force that leads to material milling due to friction. On the other hand, the reverse rotation of the disc with respect to the mill applies a centrifugal force in the opposite direction. This leads to the transition of balls on the mill's opposite walls and results in impact effect (Figure II.1c) (*Baheti, et al., 2012*).

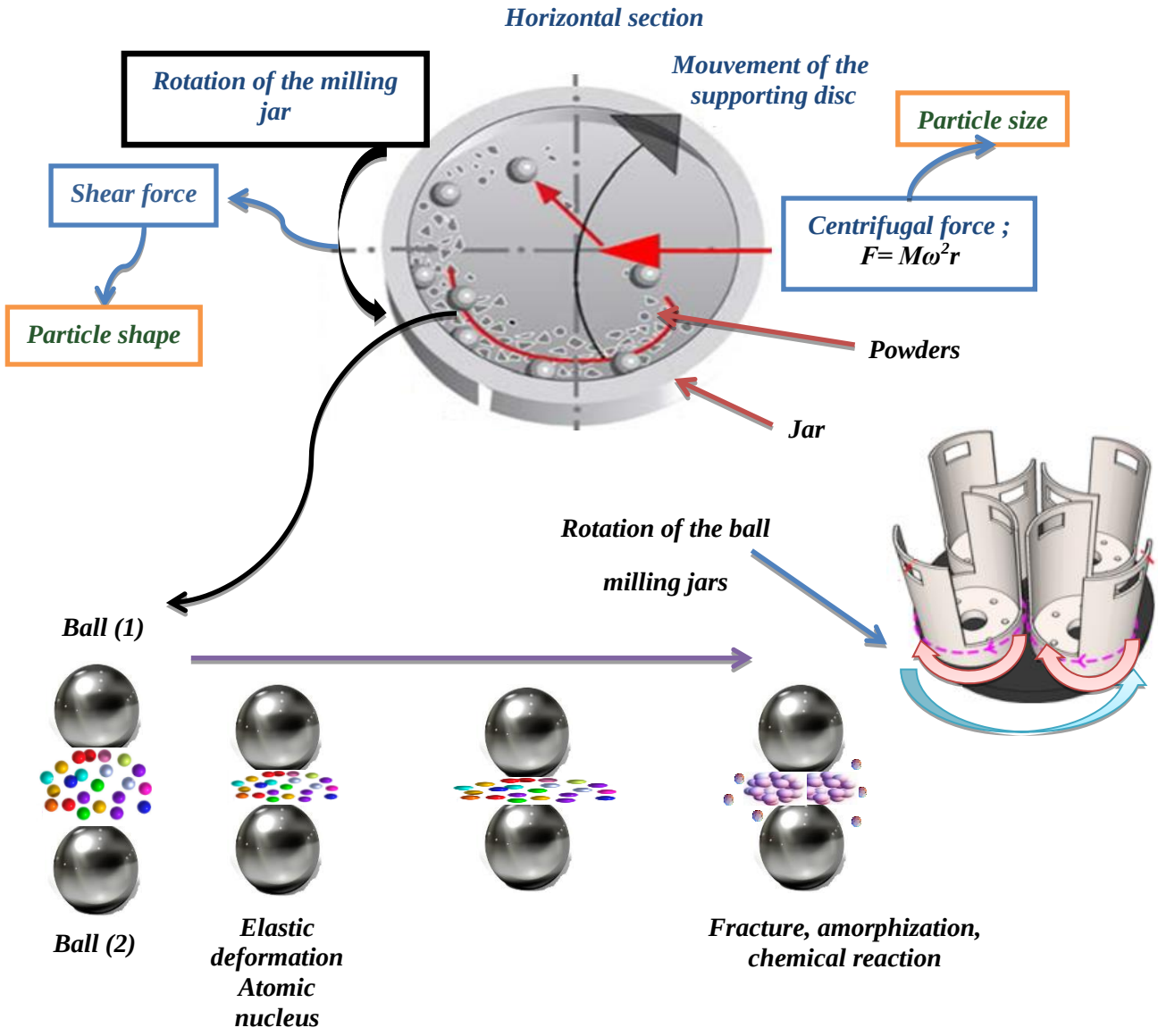

Figure II.1: *Working principle of Planetary Ball Mill (Baheti, et al., 2012).*

- **Parameters of Planetary Ball Mill**

The planetary ball mill process involves loading powders with the milling medium in a vial with severe deformation. The main parameters of planetary ball mill are (*Suryanarayana, 2001*):

- Type of mill (mixer or planetary),
- Height and volume of vial,

- Number, diameter and type of milling balls,
- Ball to powder mass ratio,
- Operation: Milling time, rotation speed, kinetic shock energy, shock frequency,
- Other parameters: milling temperature, milling atmosphere (e.g. argon, nitrogen) and process control agent.

In this thesis, the time of milling was varied from 0h to 3h.

II.1.3 Experimental Setup

Pure elemental powders of iron, cobalt and amorphous red phosphorus were weighted with a sensitive balance in a glove box under an inert atmosphere (Figure II.2). Ball milling of the $Fe_{15}Co_2P_3$powder mixtures was performed using a Retsch PM 400 planetary ball mill at room temperature under an inert atmosphere and with hardened steel balls and vials. Milling experiments were done at rotational velocities of 350 rpm. Milling was carried out as a sequence of 30 min milling intervals interrupted by 30 min breaks to avoid excessive temperature rise. The starting materials for the milling experiments (6 g) were charged in the milling vials, together with 10 mm-diameter steel balls to give a ball-to-powder mass ratio of 10:3.

(a) ***(b)***

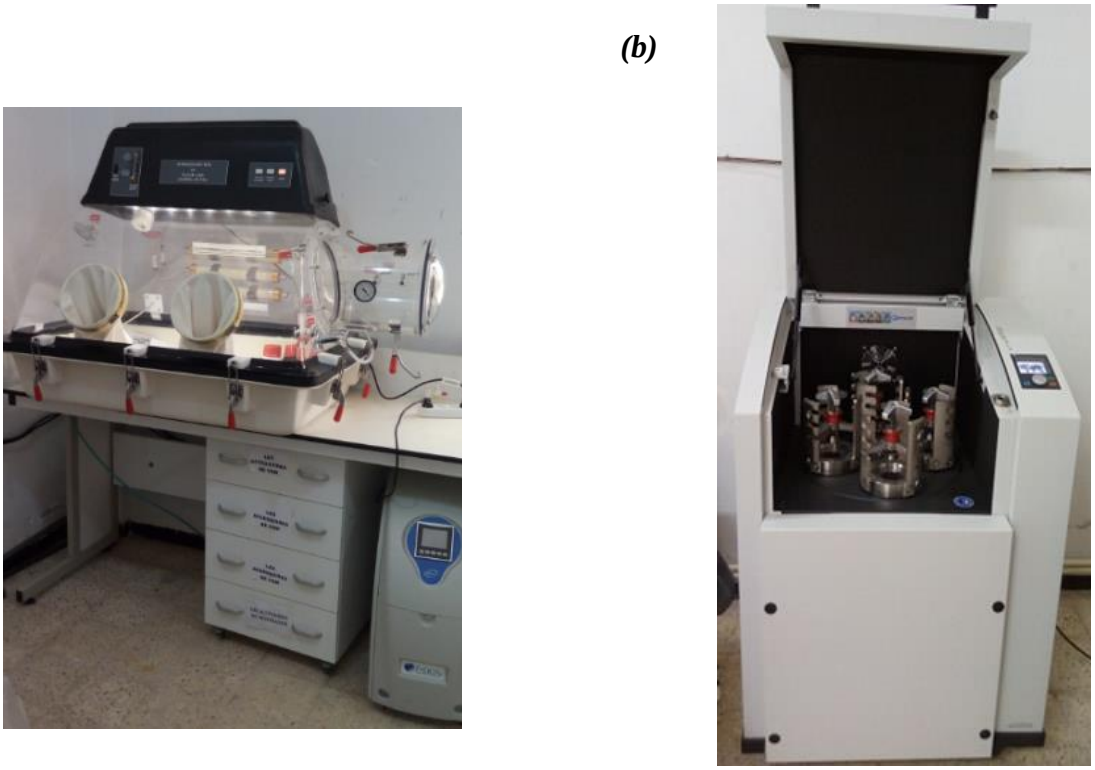

Figure II.2: *Instruments used in the elaboration of $Fe_{15}Co_2P_3$ powder mixtures.* ***(a)*** *glove boxPlas-LabsInc type, and* ***(b)*** *high energy planetary ball mill Retsch PM 400. (LPCM, El-taref University).*

All the milling parameters used in the current study are listed in Table II.2

Table II.2: *Milling parameters used in the current study.*

Parameter	***Value***
Weight of powder	6 g
BPR	10:3
Atmosphere	Argon atmosphere
Milling medium	5 stainless steel balls (10 mm diameter) and stainless vial (25 mL volume)
Milling time	0, 1, 2 and 3h
Pause time	30 min/h
Milling speed	350 rpm
Type of mill	Retsch PM 400

II.2 Evaluation of Bacterial Cell Growth

II.2.1 Chemicals and Instruments

In this part of the research, all chemicals were weighted with a sensitive balance in a sterile field using Bunsen burner without further treatment, unless specified otherwise. All chemicals, instruments and testes for bacteria strains growth were obtained and treated in pedagogic laboratories of Khenchela University. Table II.3 gives detailed information of the chemicals used in this part of the study, followed by Table II.4 which defines the types of instruments.

Table II.3: *Summary of chemicals used in the evaluation of growth in bacteria strains*

Chemicals	***Physical***	***pH at 25°C***	***Company form***
Nutrient agar	Beige Powder	6.8 ± 0.2	Liofilchem
Nutrient broth	Beige Powder	6.8 ± 0.2	Liofilchem

Table II.4: *Instruments types used in the growth of bacteria strains*

Instruments	***Type***
Autoclave	*Raypa*
Drying and heating chamber	*Binder model E28*
UV-Vis spectrophotometer	*Unico Model 1200, 325-1000*

II.2.2 Strains Used and Cultures Media

$Fe_{15}Co_2P_3$ powder mixtures at different milling time were monitored by bacteriological application. To examine the bacterial behavior of $Fe_{15}Co_2P_3$ powder mixtures milled at different milling times, common pathogen Gram-negative and Gram-positive bacteria strains were procured from Ahmed Ben Bella hospital Khenchela, Algeria. The well-known pathogenic bacteria studied were:

- The microorganisms Gram-positive bacteria

Streptococcus (α) is a common human-specific pathogen that can induce a wide spectrum of disease, ranging from noninvasive diseases, such as pharyngitis, scarlet fever, and impetigo, to invasive diseases, such as erysipelas, cellulitis, pneumonia, bacteria, necrotizing fasciitis, and toxic shock syndrome. *Streptococcus (α)* belongs to the family *Streptococcaceae*; an important cause of morbidity and mortality worldwide.

Staphylococcus aureus (S. aureus) is one of the components of microbiota that belongs to the family *Streptococcaceae*. It is a major cause of infective endocarditic and sepsis. *S. aureus* is the most common cause of skin, soft tissue infections and the respiratory tract. However, the bacterial genetic changes associated with adaptation to human skin are not well characterized.

- The microorganisms Gram-negative bacteria

Klebsiella pneumonia (K. pneumoniae) represents a saprophytic pathogen that can affect plants, animals, and humans. It belongs to the family *Enterobacteriaceae*. In medical terms, *K. pneumoniae* is an enteric bacterium responsible for multiple nosocomial infections, including pneumonia, urinary tract, soft tissue infections, and septicemias.

Haemophilus influenzae (H. influenzae) strain is a coccobacilli bacterium that can cause invasive disease. It belongs to the family *Plasteurellaceae. H. influenzae* disease in humans ranges from non-invasive infections such as acute otitis media to severe invasive infections like meningitis and epiglottis. *H. influenza* commonly resides as commensals within the human pharynx and may cause respiratory or invasive infections, variable for the presence of a polysaccharide capsule.

Culture media, also known as growth media or nutrient agar, is a specific mixture of nutrient and other substances that support the growth of microorganisms such as bacteria. Liquid culture medium, also called broth, is a medium widely used for the culture of undemanding microorganisms. The nutrient broth was used for the bacterium and $Fe_{15}Co_2P_3$ powder mixtures contact. Culture media preparation must be carried out accurately to ensure microbiological growth is correctly promoted. The preparation of both the growth media and the nutrient broth is completed first. The individual

ingredients of the nutrient agar and nutrient broth powders were carefully weighed out according to the culture media formulation recipe using a precision sensitive balance and suspended in distilled water. Then, the ingredients were well mixed and heated to boil with a magnetic stirrer until completely dissolved powders. The agar medium was poured into a flask and the broth culture dispensed into tubes then sterilized at 121°C for 15 minutes using an autoclave; a huge steam cooker. The agar was afterward poured into sterile Petri dishes where the rack was tilted to allow the agar to solidify using Bunsen burner flame which creates a sterile field. Subsequently, in the sterile field all the bacterial strains were cultured by taking a single colony from the stock bacterial culture with an inoculating loop and streaking it to the Petri dishes containing the nutrient agar. The weighed $Fe_{15}Co_2P_3$ powder mixtures by analytical sensitive balance were added to 9 ml of liquid growth, with concentrations of 0.00, 0.22, 0.88 and 1.66 mg/mL in a sterile field. The sample with a concentration of 0.00 mg/mL was considered as a control. Again, it was placed in a drying and heating chamber, with the stock bacterial new culture, overnight at 37°C. Controls (0.00 mg/mL) and test samples were incubated exactly in the same conditions. All the steps and instruments are shown in Figure II.3. Sterility matters in culture media preparation; it's the most common area for things to go wrong. It is essential that the stated directions are followed when sterilizing culture media so that vital microbial nutrients and other factors are not destroyed and so that toxins are not developed through excessive heating.

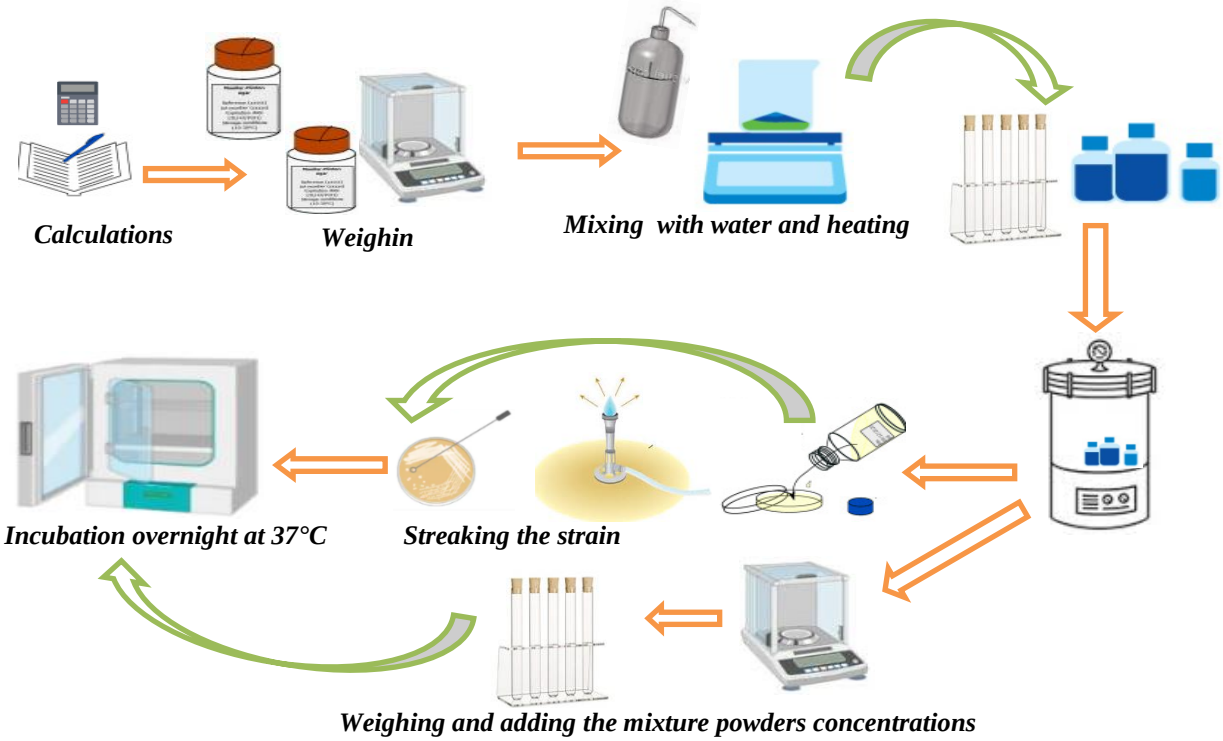

Figure II.3: *Instruments and steps used for bacterium cultures media and $Fe_{15}Co_2P_3$ powder mixtures samples.*

II.2.3 Optical Density

On the second day in a sterile field, a minimum quantity of incubated bacterial strains were taken by a loop and added to the different concentrations and controls and returned back for incubation. After the growth of bacteria, a typical kinetic growth curve experiment, the growth of different concentrations of the $Fe_{15}Co_2P_3$ powders with all the bacteria strains were monitored by determining the population growth rate using the optical density method with a UV-Vis spectrophotometer with quartz cells to assess bacteria cell density, based on the measurements of light extinction at the wavelength of 600 nm with nutrient broth as a reference. The readings were performed every 2h and up to 24h, as shown in Figure II.4.

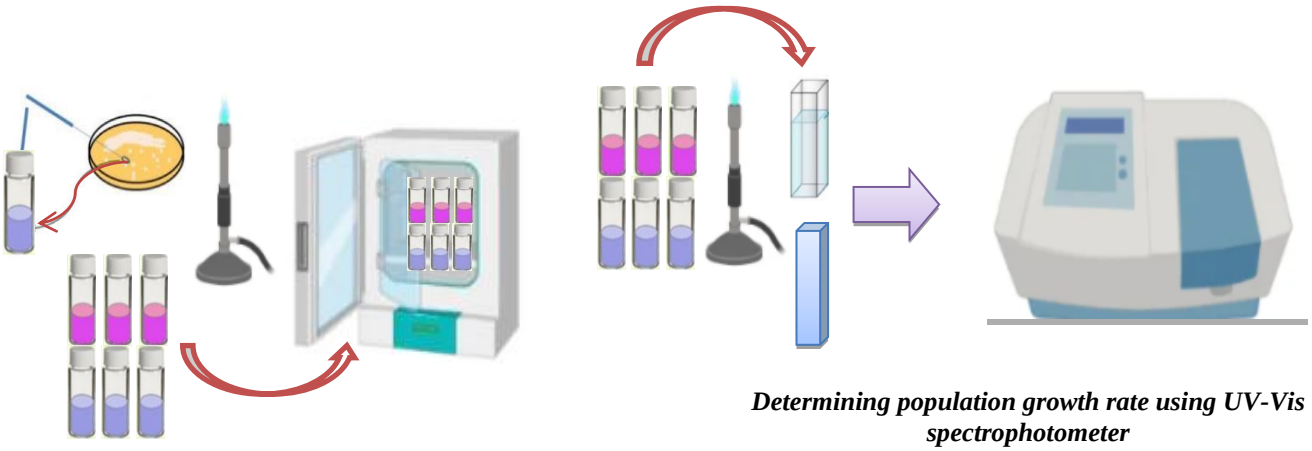

Figure II.4: *Determining population growth rate using the optical density method.*

II.3 Characterization Methods

II.3.1 X-ray Diffractometry

X-Ray Diffraction (XRD) is a qualitative, powerful and nondestructive analytical characterization technique that uses X-ray radiation. X-ray powder diffraction has been the preferred choice for qualitative phase analysis for over 100 years, since von Laue's discovery of the diffraction of X-rays in 1912 (*Eckert, 2012*).A primary use of XRD analysis is the identification of materials based on their diffraction patterns. As well as phase identification, XRD also yields information on how the actual structure deviates from the ideal one, owing to internal stresses and defects. This characteristic is based on the absorption and re-emission of electromagnetic radiation, whereby the energy remains constant. The electrons around the nucleus are accounted for this phenomenon. It provides information on crystalline phases and orientations; it determine structural properties such as, lattice parameters, strain, average grain size, epitaxy, crystallinity, crystal defects, phase composition and preferred orientation (texture). In addition, this technique measures the thickness of thin films and

multi-layers and determines atomic arrangements. Furthermore, it is able to differentiate differences between structures even when assuming they have the same elemental profiles, and thus it can detect minute differences between samples.

II.3.1.1 Working of XRD Instrument

In XRD, a collimated beam (thin and parallel beam) of X-rays is directed towards the sample. The crystal structure can diffract X-ray because the interplanar spacing in a crystal lattice is of the same order as that of the wavelength of X-ray. The incoming beam of rays can penetrate deep into the material and can be diffracted from the periodic arrays of the specimen's atoms and scatter in the outward direction. The angle between an incoming beam and the surface of the specimen is θ. The angle of the diffracted beam is 2θ; which is dependent on the arrangement of the atoms and the type of atoms, etc. The diffracted beam is then detected by a detector and sent to a computer to produce an XRD pattern (Figure II.5).

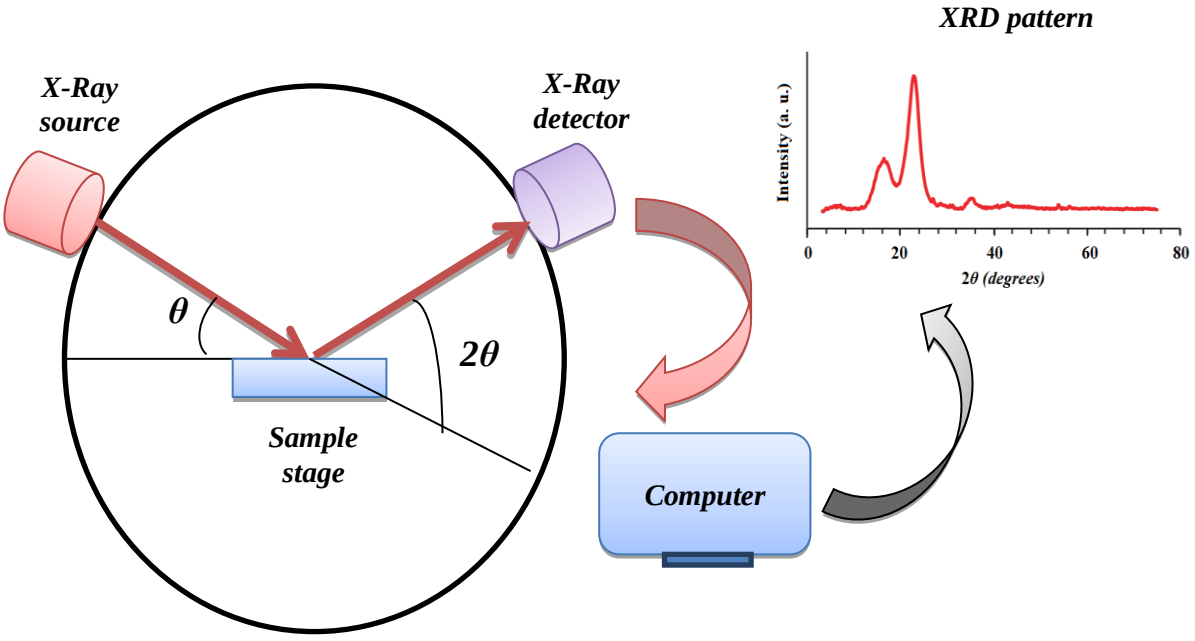

Figure II.5: *Schematic representation of working of XRD instrument along with XRD pattern.*

The structure of the milled powder was checked by XRD using a Bruker-D8 advanced diffractometer in a (θ–2θ) Bragg–Brentano geometry, equipped with Cu-Kα radiation source (λ_{Cu} = 0.15406 nm) (Figure II.6).

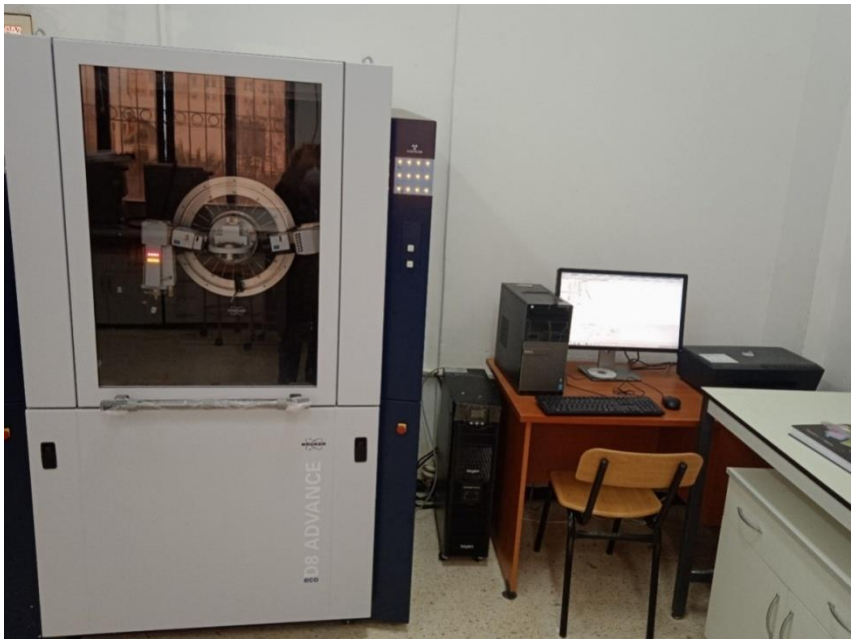

Figure II.6: *Bruker-D8 advanced diffractometer (LPCM, El-taref University).*

II.3.1.2 Principles of X-ray Diffraction

When a propagating X-ray wave encounters some regularly spaced particles, where the wavelength is in the same order of magnitude as the spacing between the particles, diffraction occurs (*Callister, et al., 2013*). The resulting interference pattern is dependent on the phases of the diffracted waves. X-rays can be considered as waves of electromagnetic radiation with high energies and short wavelengths (in the order of the atomic spacing for solids). When an X-ray beam hits a solid material, some of the waves are scattered in all directions by the electrons of the atoms that make up the solid. Not all diffracted waves appear, however, in the interference pattern due to the destructive interference caused by out of phase waves. A crystal can be described as a grating, which is made up of atomic layers with a designated distance *d*. These layers correspond to the crystallographic planes, described by the Miller Indices *h*, *k* and *l*. For every crystal structure, only one possibility exists; that is, how the atoms and the appropriated lattice planes are ordered. Diffraction occurs, if the distance between the gridlines in gratings is in the order of the X-ray radiation wavelength's magnitude.

Bragg's law gives a condition for the intensity of the diffracted beam related to the angle between the diffracted beam and the solid. This behavior is summarized by the equation:

$$n\lambda = 2\, d_{hkl}\, sin\theta \qquad \text{(II. 1)}$$

Where n is the order of diffraction, λ is the wavelength of the incident X-ray, d is the interplanar spacing within the crystalline solid known as the distance between the crystallographic planes (*h*, *k*, and *l*), θ represents the incident angle between the X-rays and sets of parallel "planes" in the crystalline solid (also called Bragg angle). Bragg's condition is schematically depicted in Figure II.7.

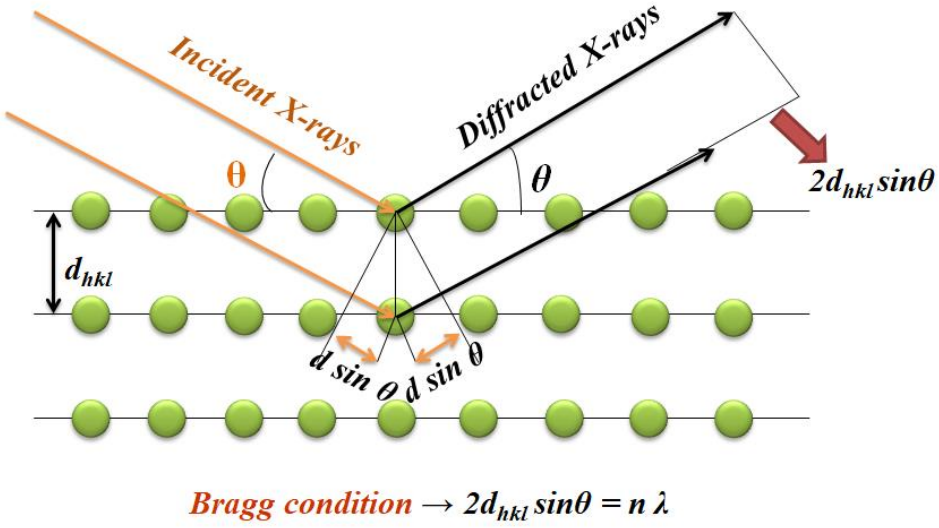

Figure II.7*: *Diffraction of X-ray waves by crystallographic planes.

II.3.1.3 Rietveld Refinement on X-Ray Diffraction Patterns

A powder X-ray diffraction pattern is represented as a two dimensional plot showing the intensity as a function of the diffraction angle. After the preliminary data analysis, the diffraction pattern could be decomposed. Recently, the Rietveld method (*Rietveld, 1969*) was adapted for quantitative XRD analysis (*Hill, et al., 1987* and *Bish, et al., 1988*). This method involves calculating diffraction patterns of a mixture's individual components using a crystal structure model. To identify the phases of a measured pattern, their diffraction lines have to be compared with already known structure data from the literature. Qualitative and quantitative phase analysis of XRD patterns was investigated by the Rietveld refinement data (*Young, 1996*) analysis. The calculated diffraction pattern can be fitted to the measured one using the Materials Analysis Using Diffraction (MAUD) program (*Lutterotti, et al., 1999*). The resultant simulated pattern is fit to an observed pattern by varying parameters of the model(s). The Rietveld method is very powerful and provides not only abundances but also other quantitative measurements, namely:

- Quantitative phase analysis (crystalline and amorphous).
- Lattice parameters.
- Atomic positions and occupancies.
- Temperature vibrations (isotropic and anisotropic).
- Grain size and micro-strain (isotropic and anisotropic).
- Stacking and twin faults.

A (nonlinear) least squares optimization method can be used to fit the parameters in the approximation of the residue function, M, which is the weighted sum of squares used only for the

minimization routines. Its absolute value depends on the intensities and the number of points (*SenGupta, et al., 2002*):

$$M = \sum_i w_i (y_i - y_{ci})^2 \qquad \text{(II. 2)}$$

Where y_i and y_{ci} are, respectively, the observed and calculated intensities at the point *I*, w_i is the weight factor associated with the i^{th} observed count:

$$w_i = \frac{1}{y_i} \qquad \text{(II.3)}$$

The calculated intensity y_{ci} is obtained by summing different contributions of *Bragg* and the continuous background (*Gravereau, 2012*), as follows:

$$y_{ci} = y_{bi} + \sum_{\emptyset=1}^{phases} S_{\emptyset} . \sum_{K=1}^{K} j_{\emptyset k} . L_{P\emptyset k} . O_{\emptyset k} . A . |F_{\emptyset k}|^2 . \Omega_{i\emptyset k} \qquad \text{(II. 4)}$$

With y_{bi} is the continuous background intensity, *K* is Miller's index for a reflection *h*, *k* and *l*, S_ϕ is a scale factor proportional to the volume fraction of each refined phase, $j_{\phi k}$ is the multiplicity factor of the k^{th} reflexion peak, $L_{P\phi k}$ is the Lorentz-Polarization factor, $O_{\phi k}$ is a correction factor describing the preferred orientation. A is the absorption factor, $F_{\phi K}$ is the structure factor, and $\Omega_{i\phi k}$ is the profile shape function.

The reliability factor R_p about the profile is considered. The summation is extended to the number of profile counts.

$$R_P = \frac{\sum(y_i - y_{ci})}{y_i} \qquad \text{(II.5)}$$

The quality Rietveld refinement can be checked by the so called R-factor, also known as the reliability weighted, R_{wp}. The weighted profile R-factor follows directly from the square root of the quantity minimized, scaled by the weighted intensities. A smaller R-value corresponds to a better fitting between the observed and the calculated pattern. The weighted pattern R_{wp} is given as:

$$R_{wp} = \sqrt{\frac{\sum_i w_i (y_i - y_{ci})^2}{\sum_i (w_i y_i)^2}} \qquad \text{(II.6)}$$

The expected *R* factor, R_{exp}, is given by the equation:

$$R_{exp} = \left(\frac{N-P}{\sum_i (w_i y_i)^2}\right)^{1/2} \qquad \text{(II.7)}$$

N and *P* are the number of experimental points and refined parameters, respectively.

Bragg factor is defined by the expression:

$$R_{Bragg} = \frac{\sum_k |I_k - I_{kc}|}{\sum_k I_k} \qquad \text{(II.8)}$$

Where I_k and I_{kc} are integral and calculated intensities of Bragg pick, respectively.

The Rietveld refinement is a mathematical method, which describes the whole pattern using structure, profile and instrument related parameters. In a least square process, the calculated and the observed intensities were compared. The goodness of fit GoF can be determined from the expected and the weighted profile *R* factors:

$$GoF = \frac{R_{wp}}{R_{exp}} \qquad \text{(II.9)}$$

Generally, a known contribution to X-ray peak broadening is the small crystallite size. The average crystallite size <*L*> at the nanoscale is obtained from the line broadening at half the maximum intensity β_{hkl}. Where, the peak width (β) is inversely proportional to crystallite size <L>. Since its first publication, the Scherrer equation is used in X-ray diffraction and crystallography (*Scherrer, 1912*). This formula, named after the Swiss physicist Paul Scherrer, has become a widely used analytical method for determining crystallite size in a powdered sample by measuring X-ray line profile broadening. The average nanocrystalline size was calculated using Debye-Scherrer's formula (*De, et al., 1984*):

$$\beta_{hkl} = \frac{K\lambda}{<L>cos\theta} \qquad \text{(II.10)}$$

Where B_{hkl} is the line broadening at half the maximum intensity, *K* is the dimensionless shape factor, also known as the constant of proportionality (the Scherrer constant). The latter depends on the width determination, the shape of the crystal, and the size distribution. The shape factor has a typical value of about 0.9, λ (the X-ray wavelength). <*L*> is the average crystallite size. As the crystallite size gets smaller, the peak gets broader. θ is Bragg angle.

According to Williamson–Hall approach (*Williamson* and *Hall, 1953*), the diffraction line broadening is due to the crystallite size and strain contribution. Uniform deformation model considers uniform strain throughout the crystallographic direction, which is introduced in the nanocrystals due to crystal imperfections. In other words, uniform deformation model considers strain isotropic in nature (*Hall, 1949*). The strain induced in powders due to crystal imperfection and distortion was calculated using the formula:

$$\beta_{hkl} = 4\sigma \tan\theta \qquad \text{(II.11)}$$

With σ is the strain also called deformation parameter, $\sigma = \frac{\Delta d_{hkl}}{d_{hkl}}$.The average strain was calculated using the formula:

$$< \sigma^2 >^{1/2} = \frac{1}{2\sqrt{2\pi}} \frac{\beta_G}{tan\theta} \qquad \text{(II.12)}$$

II.3.2 Vibrating Sample Magnetometer (VSM)

The Vibrating Sample Magnetometer (VSM) is one of the most successful implementations of a magnetometer, first proposed and developed by Simon Foner in 1955 and reported it in 1959 (*Foner, 1956 and 1959*). VSM is a sensitive and versatile instrument commonly used for determining the material's magnetic moment as a function of magnetic field and/ or temperature. Its use to measure magnetization is based on the Faraday's laws of induction, which states that an electromagnetic force is induced when a conductor is placed in a varying magnetic field. It allows measuring the basic magnetic properties, such as hysteresis loop, magnetization curve, and field cooling curve. Moreover, the magnetic parameters such as coercive force, magnetic field strength, saturation magnetization, retentively, magnetic conductivity, Curie temperature, magnetic anisotropy and susceptibility can be measured in a wide range of temperatures with very high precision. In this technique, the magnetic sample is placed in a constant applied magnetic field in which the sample is physically vibrated sinusoidally. Since the magnetic flux changes due to the sample's vibration, the induced voltage in the pick-up coil varies sinusoidally (Figure II.8). This induced voltage is measured using a lock-in amplifier and then converted into magnetization. The magnetic properties of pellet, powder, film, disk and sphere shaped sample could be measured by this technique.

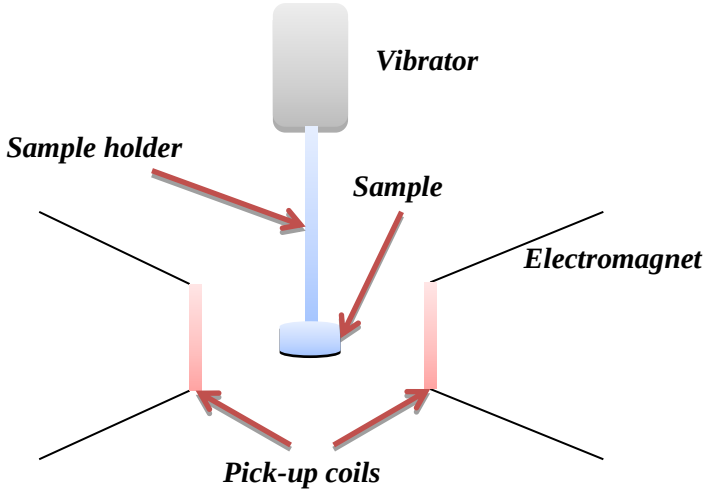

Figure II.8: *Schematic diagram of vibrating sample magnetometer.*

The magnetic characterisation was performed using the vibrating sample magnetometer *MicroSence-EZ7* under an applied magnetic field of *20 kOe*. The samples were characterized at *300 K* (Figure II.9).

Figure II.9: *Vibrating sample magnetometer MicroSence-EZ7 (LPCM, El-taref University).*

II.3.3 Ultraviolet–Visible (UV-VIS) Spectroscopy

Spectroscopy in the ultraviolet (UV) and visible (Vis) spectra is an analytical and powerful technique widely used in many areas of science ranging from bacterial culturing, drag identification, chemical research and biochemistry. This technique measures the amount of discrete wavelengths of UV or visible light that are absorbed by or transmitted through a sample in comparison to a reference or blank sample. This property is influenced by the sample composition (in terms of content and concentration). The optical density (OD), also known as the absorbance, is the quantity of light absorbed by a solution. The OD measurement follows Bear-Lambert law which states that the absorbance of a solution varies directly with the density of the absorbing material and the free path length. In fact, OD measurements are the most common measurement used in microbiology laboratories to assess microbial growth. It is used both qualitatively as the turbidity of a culture and quantitatively as a measure of the intensity of light transmitted along a path through the culture of a known path length. UV-Vis spectrophotometers are also used as detectors in many biological processes, like high pressure liquid chromatography, analytical chemistry, structural biology etc. Spectroscopic analysis is common for solutions, though solids and gases can also be analyzed.

The optical density is often used in spectrophotometry and can be expressed by the following equation:

$$OD = -log\left[\frac{I}{I_0}\right] \qquad \text{(II.13)}$$

In this equation, I_0 is the incident light intensity, I is the intensity of light transmitted through the sample and measured by the photo sensor (*Svanberg, 2004*).

A standard spectrophotometer measures absorbance one sample at a time, typically placed in a cuvette through which light is sent horizontally. An absorbance plate reader offers higher through put and can measure the absorbance of samples in microplates, by sending light through each wall vertically. Light of a certain wavelength, depending on the material being measured, is passed through a sample, and a detector on the other side of the microplate wall measures how much of the original light was absorbed by the sample in the wall (Figure II.10).

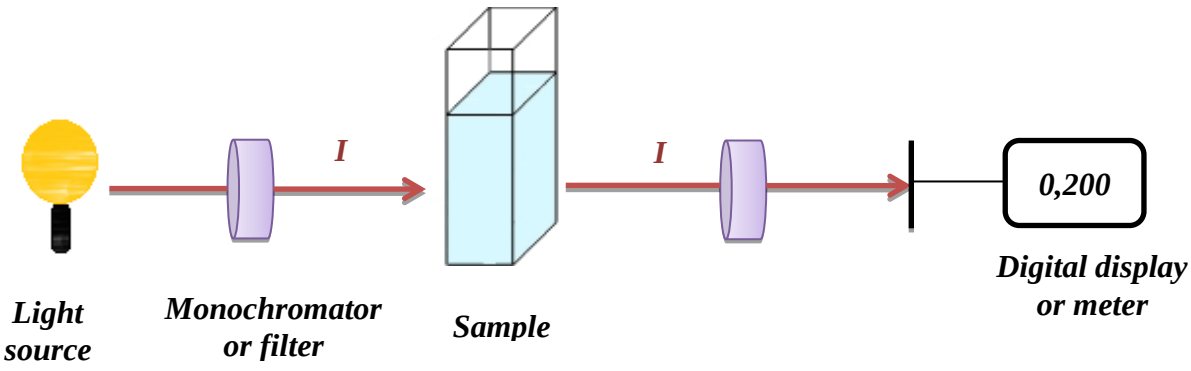

Figure II.10: *Schematic diagram of UV-Visible spectrophotometer.*

A UV-Vis spectrophotometer Unico Model 1200, 325-1000 was used in this study to measure optical density (Figure II.11).

Figure II.11: *UV-Vis spectrophotometer Unico Model 1200, 325-1000 Range. (Pedagogic laboratories. Khenchela University).*

II.3.4 Fourier-Transform Infrared Spectroscopy (FTIR)

Fourier transform infrared (FTIR) is a practical tool for qualitative and quantitative analysis. It is a simple, rapid and sensitive method for chemical compounds analysis. In this energy region spectra are often classified by wave number in the range of 4000-400 cm^{-1}.

FTIR gives valuable information about the rotation and vibration of the molecular structures and chemical bonding status of the materials, which make it easier for investigating both inorganic and organic materials. Besides, an infrared spectrum provides information about a sample's fingerprint with absorption peaks associated with the vibrations frequencies between the bonds of the sample atoms. This spectroscopy probes the molecular vibrations. In particular, when a molecule has a center of symmetry, all vibrations which are symmetrical with respect to the center are infrared inactive. In contrast, the asymmetric vibrations of all molecules are detected. Consequently, infrared spectroscopy can lead to an identification of materials. Besides, with the FTIR, we are able to decide the quality of a sample, identify unknown materials and the components amount in a mixture. The FTIR spectrometer is based on the Michelson interferometer theory (*Michelson, et al., 1887*).This technique uses the mathematical process (Fourier transform named after the French mathematician and physicist Jean Baptiste Joseph Fourier) to translate the raw data (interferogram) into the actual spectrum. FTIR method is used to obtain the infrared spectrum of transmission or absorption of a fuel sample.

The FTIR is consisting of IR source, laser, beam splitter, fixed mirror, moving mirror, laser detector and IR detector. Figure II.12 shows the schematic diagram of FTIR.

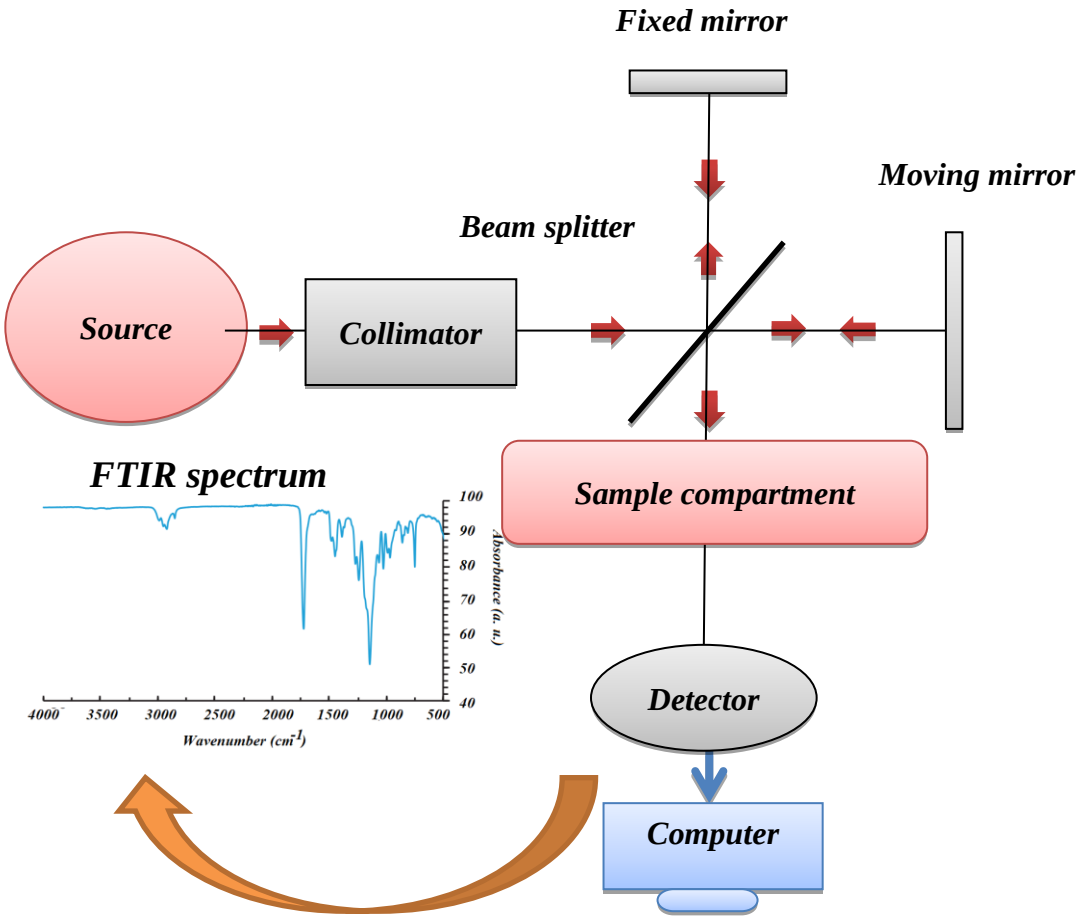

Figure II.12: *Schematic diagram of FTIR.*

The FT/IR-4700 was designed to provide operational features and sensitivity levels found only in more expensive instruments (Figure II.13). The innovative technology incorporated in these instruments results in exceptionally high signal-to-noise ratio specifications. The FTIR spectrophotometer (FT/IR-4700) recorded the spectra within the range of 4000 to 400 cm^{-1}.

Figure II.13: *FTIR -4700 spectrophotometer (Pedagogic laboratories. Oum El bouaghi University).*

Chapter III:

Structural, Microstructural and Mechanical Study

This chapter is devoted to study the influence of the milling time on the structural, microstructural and mechanical properties of the nanostructured $Fe_{15}Co_2P_3$ powder mixtures obtained by high energy mechanical milling in order to have reliable results.

III.1 Structural Study

The structure of the milled powder was checked by XRD using a Bruker-D8 advanced diffractometer in a (θ–2θ) Bragg–Brentano geometry, equipped with Cu-Kα radiation source (λ_{Cu} = 0.15406 nm). The formed phases, the evolution of the structural, microstructural, and mechanical properties of the obtained powders was investigated by MAUD program (*Lutterotti, et al., 1999*) based on the Rietveld method (*Young, 1996*). For more specific formation and evaluation of the presented phases in the $Fe_{15}Co_2P_3$ powder mixtures, FTIR spectra are given.

III.1.1 X-Ray Spectral and Phase Composition Evolution of the $Fe_{15}Co_2P_3$ Powder Mixtures

The evolution of XRD patterns with milling time is displayed in Figure III.1. The diffraction peaks have Lorentzian contributions. The intensity of diffraction peaks reduced gradually. Although there was a gradual peaks' broadening as a function of the milling time, which can indicate the evolution of phases besides grain refinement, the atomic level of strains raised continuously. In addition, the variation of phase's percentage and higher crystalline defects were observed. A variety of crystal defects such stacking faults, dislocations, vacancies and grain boundaries were introduced promoting the mutual diffusivity of all elements during the milling process. The as-mentioned phenomena resulted from welding and disordering effects, occurring because of repeated collisions (ball-powder-ball and ball-powder-wall of bowl). The overlapping of XRD reflections arising from different phases results in an enlargement of peaks' width indicating a slight increase in interatomic distances leading to unit cell expansion. The effect of such phenomena can be observed clearly on the diffraction peaks illustrated in Figure III.1. For longer milling times (1, 2 and 3h), it is obvious that the line profiles are almost symmetrical due to the formation and the stabilization of a new phases after 1h of milling.

The XRD pattern of the un-milled powder mixture showed the presence of hexagonal cobalt (Co-hexagonal), simple cubic phosphorus (sc-P), and body centered cubic α-Fe (bcc-α-Fe) structures besides different structural and microstructural properties. The P phase diffraction cannot be observed because of its amorphous state and its small percentage in comparison with those of Fe (Figure III.1). After 1, 2 and 3h of milling, the same peaks are observed as in the un-milled mixture (0h) with a decrease and broadening of all peak intensities especially for (110) line. This could be explained by the diffusion of P atoms into the iron lattice during the first hour of milling, resulting in the formation of a bcc α-Fe(P) solid solution with Im-3m space group, by solid state reaction. As a consequence of their close lattice parameters, the resolution of both elements was prevented. Due to the processes of cold working and recovery during milling, grain refinement occurs leading to the formation of very fine grains. Bensalem, et al. (2009) found that the same bcc α-Fe(P) solid solution was formed after 9h of milling of $Fe_{92}P_8$ powder mixtures while Tebib, et al. (2008) confirmed the formation of this solid

solution after 21h of milling of nanostructured Fe-8P (wt%) powder mixture. Furthermore, there was a slight increase in powder temperature significantly increasing the diffusivity of solute elements into the solvent lattice and hence alloying occurs which can explain the formation of a binary bcc $Co_{75}Fe_{25}$ phase with Im-3m space group (*Suryanarayana, 2001* and *2004*).

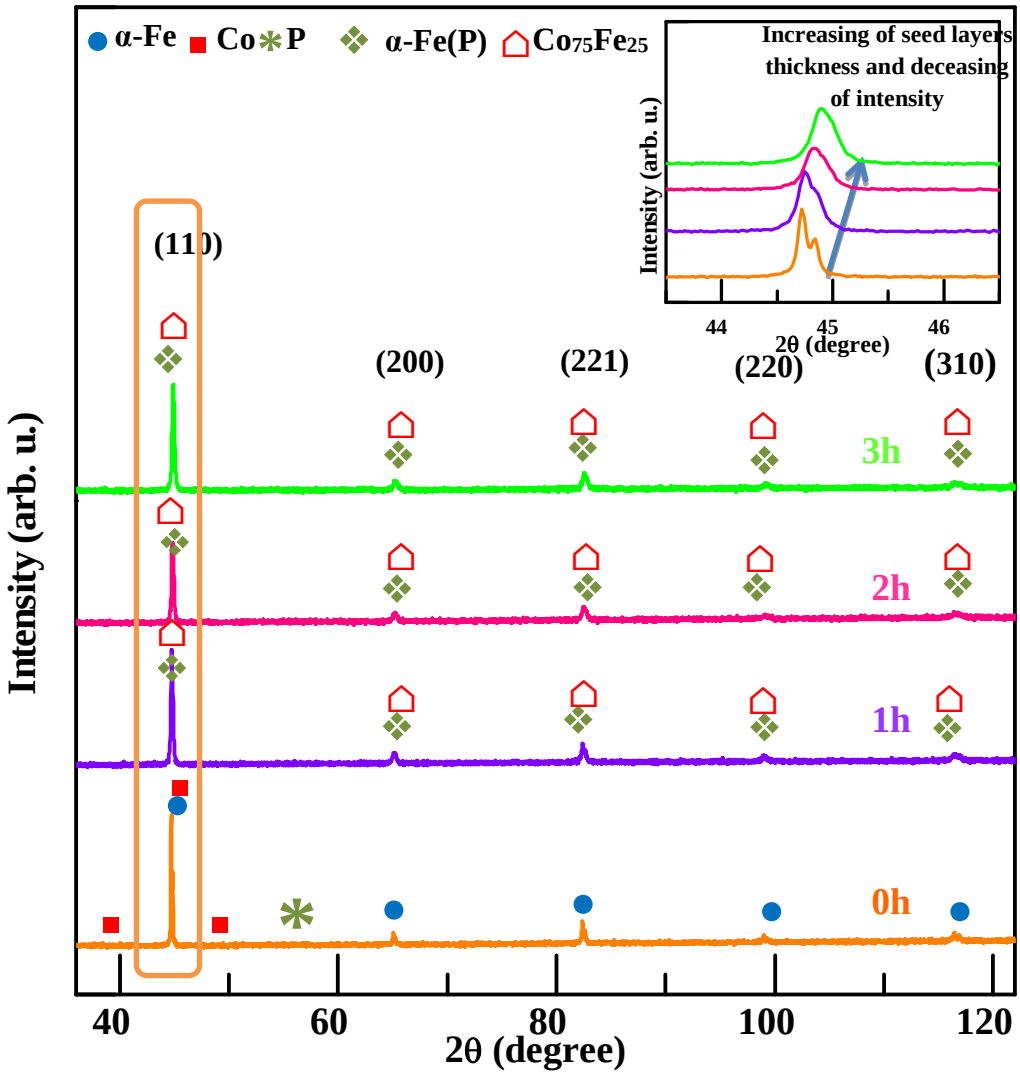

Figure III.1: *XRD patterns of $Fe_{15}Co_2P_3$ powder mixtures for different milling time (0h, 1h, 2h and 3h) indicating the (hkl) peaks and phase's positions.*

In order to check the functional behavior of the $Fe_{15}Co_2P_3$ powder mixtures, it is necessary to obtain good refinements to stabilize the microstructure. The best Rietveld refinement of XRD patterns of the powder mixtures has been obtained using an isotropic fitting model with the combination of different phases. The Marquardt least-squares procedure was adopted for minimizing the difference between the observed and simulated powder diffraction patterns to give information about the quality of fit. The best refinement was reached when GoF approached 1.0. To simulate the theoretical XRD patterns, some considerations were taken into account as indicated in Table III.1.

Table III.1: *The reliability factors, residual parameters and GoF values of the $Fe_{15}Co_2P_3$ powder mixtures revealed from Rietveld analysis.*

Milling time (h)	R_{wnb}	R_b	R_{wp}	R_{exp}	***GoF*** (R_{wp}/ R_{exp})
0	7.5424	1.8933	2.5042	2.1433	1.1683
1	2.7498	1.5797	1.9724	1.9434	1.0149
2	2.9378	1.6115	2.1459	1.9425	1.0371
3	1.8040	1.6095	2.0305	1.9698	1.0222

Figures III.2, III.3, III.4, and III.5 obtained from the MAUD program present the evolution of patterns of X-ray of the $Fe_{15}Co_2P_3$ powders as a function of milling times. For the un-milled mixture powders, the diffraction peaks characteristics show the presence of the pure sc P, bcc α-Fe in addition to Co-hexagonal structure. The best Rietveld refinement for the milled powder was found with two bcc phases: an α-Fe(P) solid solution and a binary $Co_{75}Fe_{25}$ phase. It is only natural to expect the formation of solid solutions during mechanical milling from blended elemental red P and α-Fe powders due to the formation of grain boundaries in the milled elements. This facilitates the diffusion of P into the α-Fe matrix, resulting in the creation of α-Fe(P) solid solution with less energy. This is probably due to the small difference between the radius of the host metal α-Fe and the dissolved P atom (r_{Fe} = 0.125 nm, r_P = 0.128 nm), which prefer a substitutional site in the Fe lattice. However, since the two constituent elements Fe and Co have an electronegativity of 1.8, Co atoms diffuse and incorporate into α-Fe crystal lattices giving rise to the formation of binary $Co_{75}Fe_{25}$ phase, which most likely occurs. The formation of this binary phase is due to its higher thermodynamic stability under the experimental milling conditions compared to other phases present in the binary Fe-Co phase diagram (see the appendix). The existence of the α-Fe(P) solid solution and the $Co_{75}Fe_{25}$ phase is confirmed by the important decrease of Fe and Co peaks intensities after 1h of ball milling. The same mixture of α-Fe(P) solid solution and the $Co_{75}Fe_{25}$ phase was observed after 2 and 3h of milling with deferent percentages.

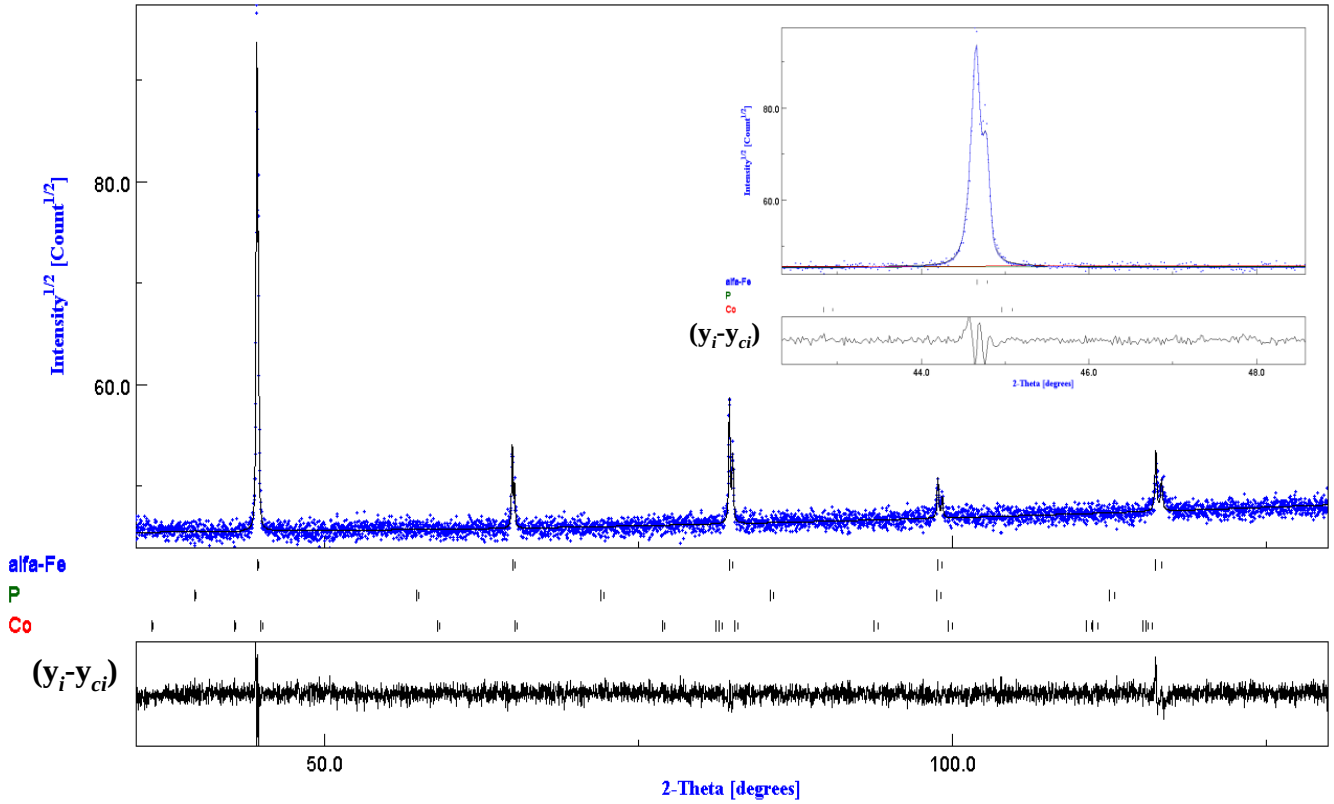

Figure III.2: *Rietveld refinement of the XRD pattern of $Fe_{15}Co_2P_3$ powder mixture before milling.*

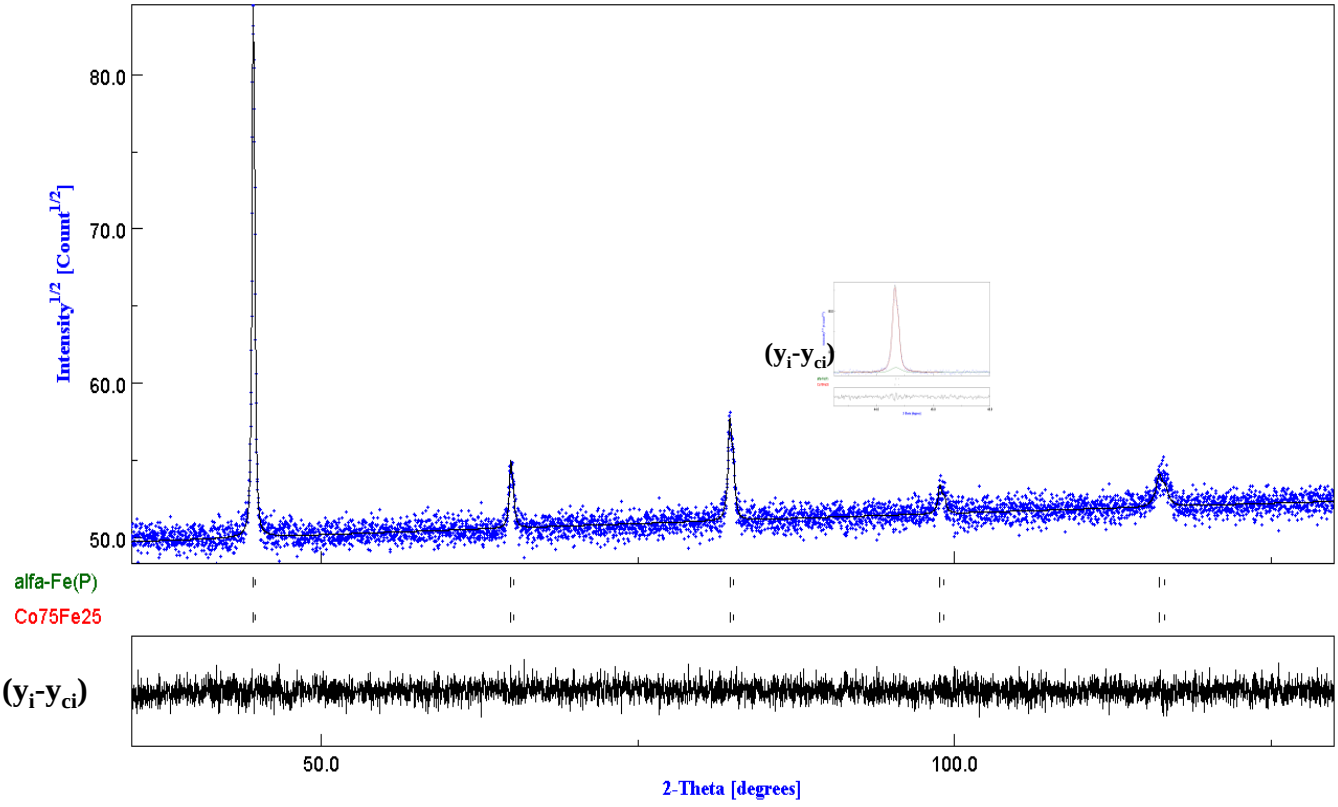

Figure III.3: *Rietveld refinement of the XRD pattern of $Fe_{15}Co_2P_3$ powder mixture milled for 1h.*

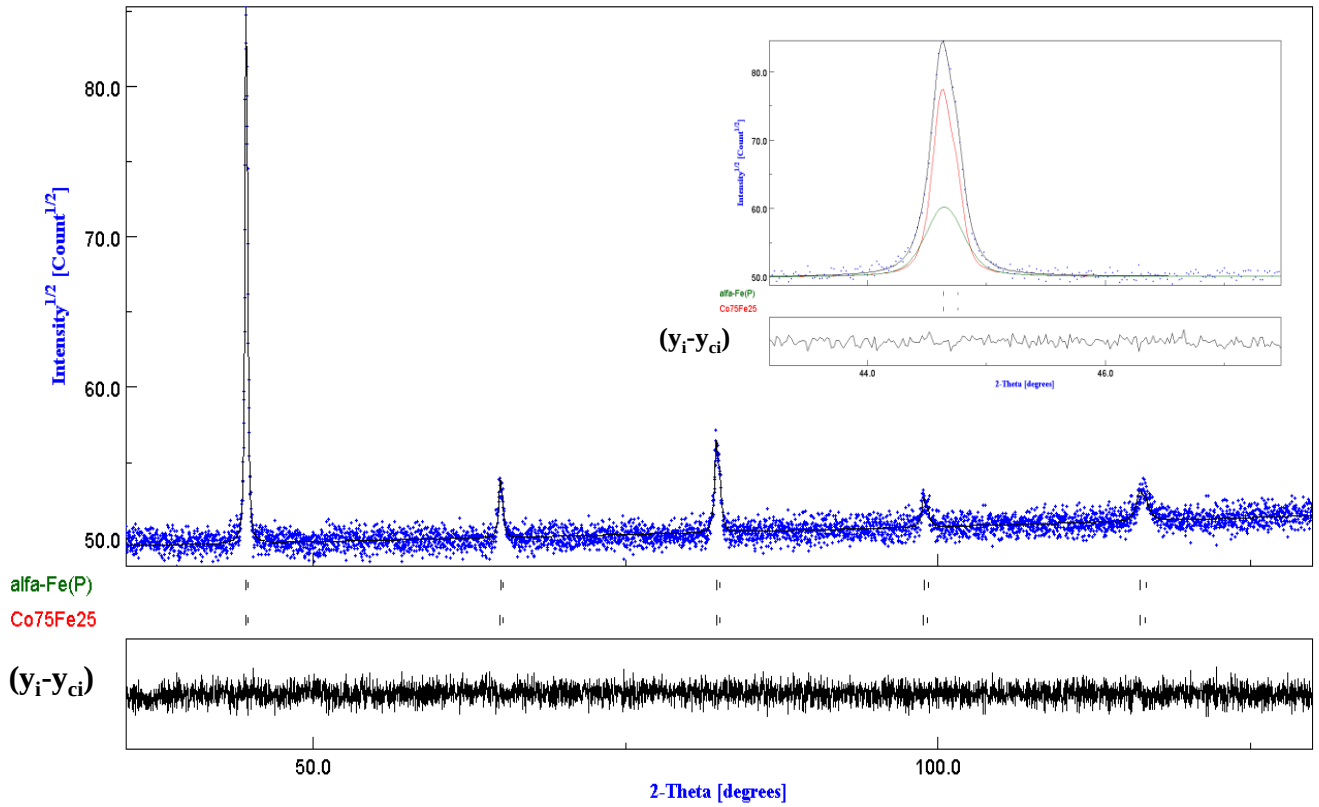

Figure III.4: *Rietveld refinement of the XRD pattern of $Fe_{15}Co_2P_3$ powder mixture milled for 2h.*

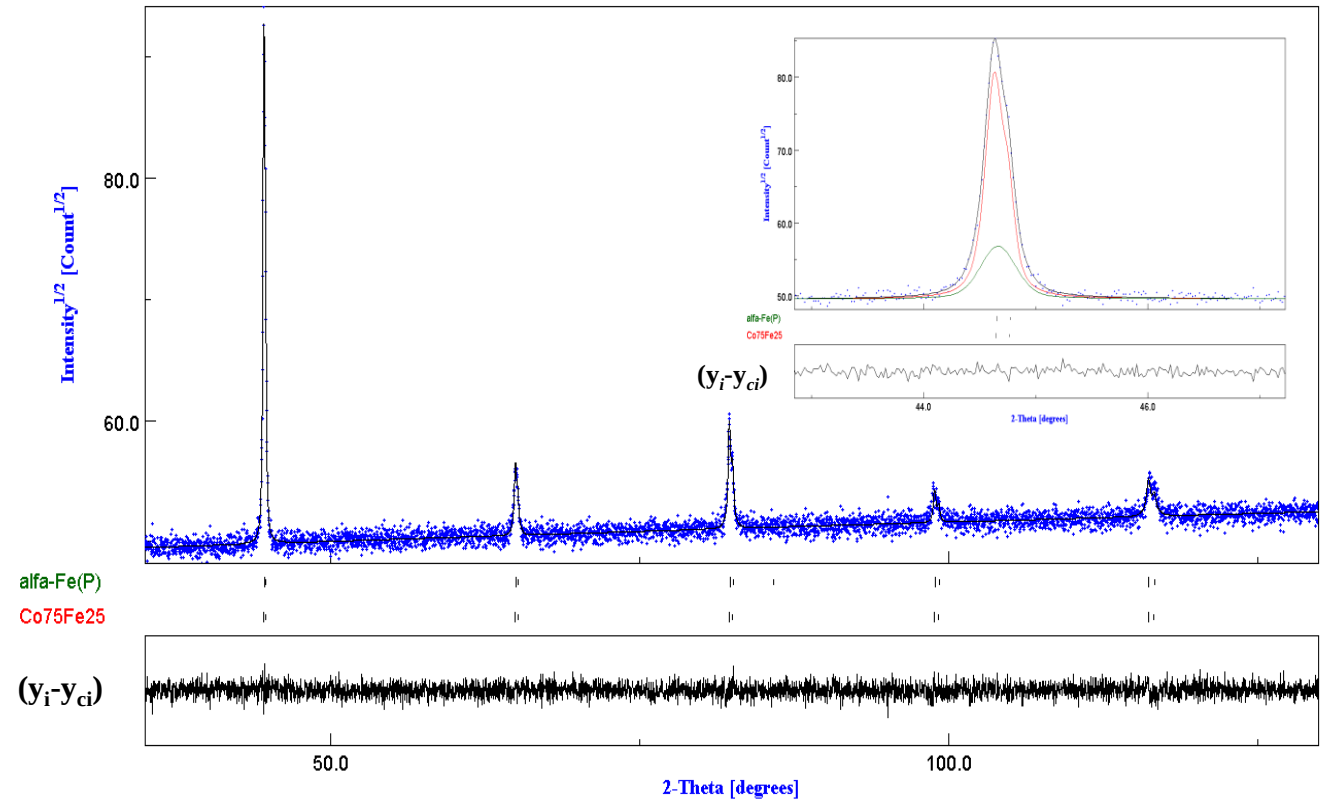

Figure III.5: *Rietveld refinement of the XRD pattern of $Fe_{15}Co_2P_3$ powder mixture milled for3h.*

III.1.2 FTIR analysis

The effects of mechanical milling time on the chemical structure and composition of $Fe_{15}Co_2P_3$ powder mixtures were elucidated by the FTIR analysis. The spectra obtained from FTIR measurements of ball-milled $Fe_{15}Co_2P_3$ powder mixtures at different milling periods 0h, 1h, 2h and 3h were recorded in the range of 400 to 4000 cm^{-1} wave number and are depicted in Figure III.6. This figure shows the change of FTIR peak and pattern. As observed, the characteristic peaks were situated in the same position after each milling period. However, the relative intensities of the peaks varied considerably indicating the change in the crystalline structure. The result shows that due to mechanical milling, few of the characteristics of bonds were changed in transmittance. In fact, as the milling time increases, a progressive increase wave numbers at 500 cm^{-1} and 1000 cm^{-1}. Also, the FTIR spectrum (Figure III.6) of samples at different milling times (1, 2 and 3 h) appeared the similar transmittances band in the wave number range of 1250–1750 cm^{-1}. FeCo materials indicate strong transmittance bands at wavenumber 507 cm^{-1} with stretching mode (*Shankar, et al. 2015* and *Farahmandjou, et al. 2018*) where the FTIR spectra of $Fe_{15}Co_2P_3$ powder mixtures indicate medium transmitance bands at the same wavenumber which can be result of presence of phosphorus in our powder mixtures and also the structure $Co_{75}Fe_{25}$. Furthermore, there is no transmittance peaks around 1650 cm^{-1} and 3400 cm^{-1} which are characteristic of water molecules. This could be evidence that the nanostructured $Fe_{15}Co_2P_3$ powder mixtures milled for different durations are hydrophobic.

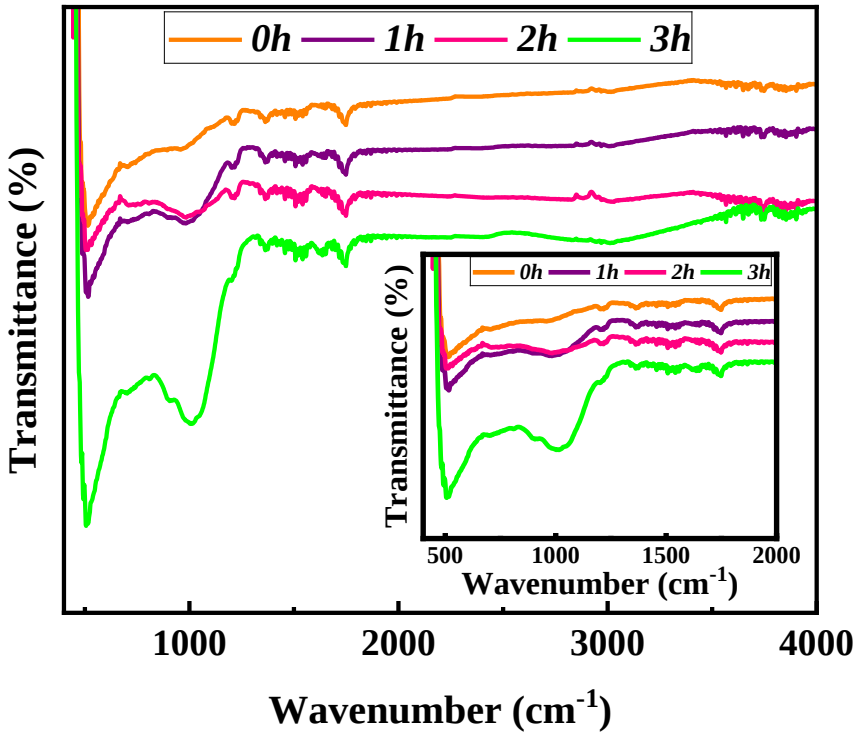

Figure III.6: *FTIR spectra of $Fe_{15}Co_2P_3$ powder mixtures milled for (t = 0h, 1h, 2h, and 3h)*

III.1.3 Effect of Milling Time on Crystalline Parameters

The mechanical milling process can generate several types of defects such as dislocation and vacancy, which influence the crystal parameters. Table III.2 presents the corresponding crystalline parameters (a and c) of the formed phase, the solid solution and the relative deviation of the lattice volume, deduced from the Rietveld refinement of the XRD patterns of the $Fe_{15}Co_2P_3$ milled powders. The relative deviation of the unit cell volume is defined by:

$$\frac{\Delta V}{V_0} = \frac{(V - V_0)}{V_0} \qquad \text{(III.1)}$$

Where V is the cell volume after milling and V_0 is the cell volume from that of the perfect crystal obtained from a_0 in the Inorganic Crystal Structure Database (ICSD).

The lattice parameter of α-Fe phase increased during the mill. This can be related to the diffusion of P and Co atoms in α-Fe matrix, leading to the formation of the solid solution and the binary phase. The lattice parameters of the α-Fe(P) solid solution and the binary $Co_{75}Fe_{25}$ phase reached the same value of about 0.2890 nm after 2 and 3h of milling. The deviation increases after the first hour of milling due to the deformation of the crystal structure of the α-Fe(P) solid solution and the binary $Co_{75}Fe_{25}$ phase, associated with the repeated fracturing, cold welding, and re-welding processes of the newly formed powdered particles and the diffusion of both P and Co atoms within the host Fe lattice. $\frac{\Delta V}{V_0}$ is found to be nearly constant after 1h of milling for both α-Fe(P) solid solution and binary $Co_{75}Fe_{25}$ phase (Table III.2). The obtained results revealed that the unit cell volume expansion of the newly formed binary $Co_{75}Fe_{25}$ phase was higher than that of the α-Fe(P) solid solution. In fact, after 3h of milling, $\frac{\Delta V}{V_0}$ of $Co_{75}Fe_{25}$ was in the order of 5.26 ± 0.02%, which is two times higher than 2.5 ± 0.02% for α-Fe(P), signifying that the structure of the binary $Co_{75}Fe_{25}$ phase is more deformed than that of the α-Fe(P) solid solution. These results can be correlated with the higher internal microstrain for $Co_{75}Fe_{25}$ compared to the α-Fe(P) solid solution, after 3h of milling.

Table III.2: *Lattice parameters and the relative deviation of the lattice volume, $\Delta V/V_0$.*

Milling time (h)	*Phase*	*a (nm) ± 10^{-4}*	*c (nm) ± 10^{-4}*	*$\Delta V/V_0$ (%)*
0	**α-Fe**	0.2882	/	-
	Co	0.2874	0.4050	-
	P	0.2280	/	-
1	**α–Fe(P)**	0.2889	/	2.3
	$Co_{75}Fe_{25}$	0.2890	/	5.14
2	**α–Fe(P)**	0.2890	/	2.56
	$Co_{75}Fe_{25}$	0.2890	/	5.24
3	**α–Fe(P)**	0.2890	/	2.5
	$Co_{75}Fe_{25}$	0.2890	/	5.26

III.1.4 Evolution of Phase's Percentage with Milling Duration

In order to investigate the phase's stabilities during mechanical milling, we obtained the phase proportions of the identified phases as a function of milling time. The obtained results are shown in Figure III.7. The milling process was divided into three main stages (I, II, and III) as shown in Figure III.7. In stage I (0-1h), a decrease in the proportions of α-Fe(P) was observed. This may be due to the mutual diffusion of P in the α-Fe matrix and to the formation of the α-Fe(P) solid solution. The percentage of the formed the $Co_{75}Fe_{25}$ phase increased rapidly in the first milling hour, at the expense of the pure Co and iron elements, reaching 60 %. During stage II (1-2h), which represents a post formation of the α-Fe(P) solid solution and the $Co_{75}Fe_{25}$ binary phase, we note that the $Co_{75}Fe_{25}$ ratio decreased inversely with the proportion of the solid solution. Finally, in stage III (2–3h), the percentage of the binary phase increases while the percentage of the solid solution decreases. In fact, the pure α-Fe has the highest percentage before milling, reaching about 75 % then varying with milling time to reach 35% after 3h milling for the α-Fe(P) solid solution. A higher value of percentage was obtained by $Co_{75}Fe_{25}$ (65% after 3h of milling). Those evolutions can be due to plastic deformations and the complexity of the milling process. In fact, all types of crystalline defects act as a short circuit of atoms diffusion.

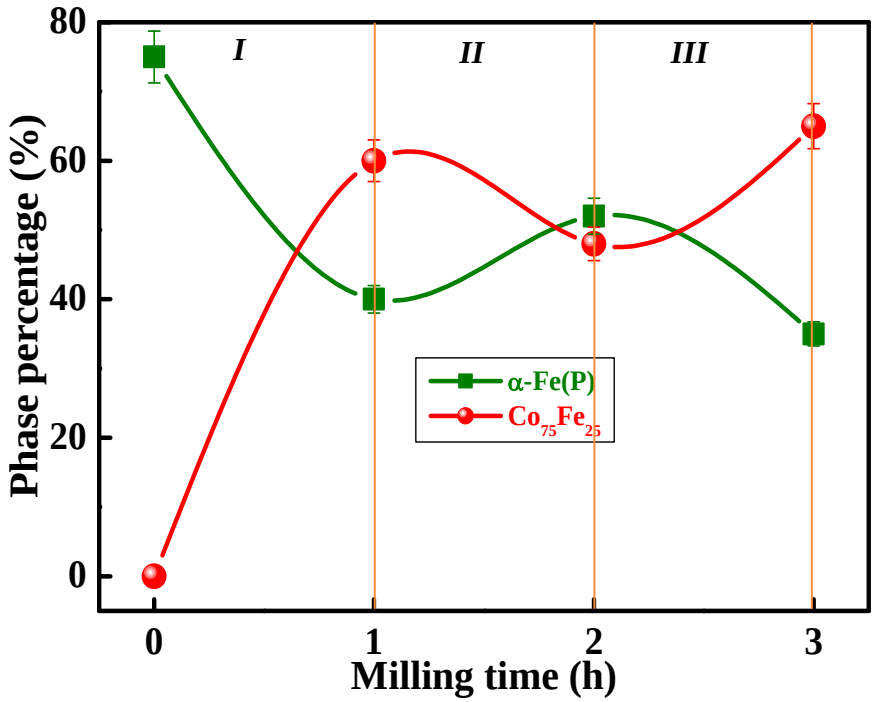

Figure III.7: *Phases percentage evolution during the milling.*

III.2 Microstructural Parameters

The microstructural parameters are essential to follow the phase constitution and transformation characteristics during high energy milling. In nanomaterials, the crystallite size and lattice strain play a major role since the phase constitution and transformation characteristics are dependent on them. The

values of the crystallite sizes $<L>$ and the internal microstrain $<\sigma^2>^{1/2}$ were obtained from Rietveld refinements of the XRD patterns by the MAUD program. Peak broadening of the diffraction profile is commonly affected by both the crystallite size and microstrain. This fact was considered in the values simultaneously extracted from the XRD peak patterns.

III.2.1 Evolution of Crystallite Sizes

Mechanical alloying process has been well known for its ability to reduce particle size to the range of nanometer in a short time (*Suryanarayana 2004*). A diffraction peak broadening, observed with increasing milling time, is usually associated with grain size reduction and increment of internal strain. Figure III.8 depicts the evolution of crystallite sizes <L> for the α-Fe(P) solid solution and the $Co_{75}Fe_{25}$ phase, plotted as a function of milling time. The formation of solid solution as confirmed by the change in XRD peaks broadening has been accompanied by particle size reduction (grain refinement). The increase in milling time results in a reduction in crystallite size and an increment in lattice strain. Accordingly, for α-Fe(P) solid solution, the crystallite size decreases from 483 nm to reach an average stable value of about 100 nm from 1 to 3h of milling. This rapid reduction indicates the effect of repeated collisions in flattening the grains. The reduction in crystallite size is mainly due to severe deformations of powders during the milling process, as well as the increase in the probability of sites nucleation during crystallization, provided by higher defects density (*Suryanarayana, 2001*). It was noticed that the crystallite size of the $Co_{75}Fe_{25}$ phase was nearly stable with milling time and reached a mean value of 193 nm (Figure III.8**)**. In fact, the crystallite size reached a saturation value possibly due to the constraint of the crystallites deformation. These results can be correlated with the values of the internal microstrains, $<\sigma^2>^{1/2}$.

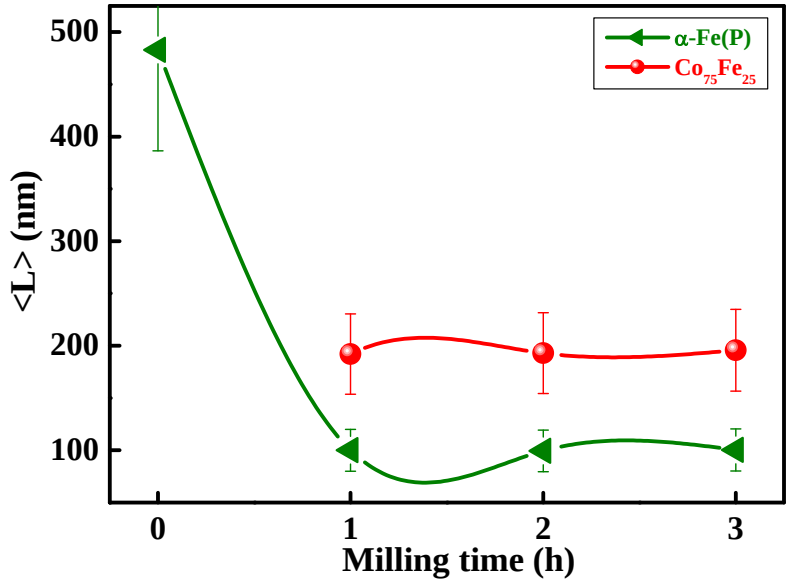

Figure III.8: *Variation with milling time, of crystallite size, <L>, for the α-Fe(P) solid solution and the $Co_{75}Fe_{25}$ phase.*

III.2.2 Internal Microstrain

The dependence of crystallite size on lattice strain is well known in nanomaterials, in addition to the preparation method and crystal dislocation contributions to lattice strain (*Dapiaggi, et al., 2005*). High lattice strain in nanocrystalline material is a result of the effect of grain boundary. While the crystallite size comes to extremely smaller size like nanometer, grain boundary is associated with more volume defects like vacancies and vacancy clusters. Hence, the stress induced from the volume defects at the grain boundaries exerts lattice strain in nanostructured materials.

The effect of milling time on internal microstrain $<\sigma^2>^{1/2}$ for the α-Fe(P) solid solution and the $Co_{75}Fe_{25}$ phase is illustrated in Figure III.9. The increment of microstrain level continues moderately until reaching maximum values of 0.04 ± 0.02 and 0.02 ± 0.02 % after 3h of milling for the binary $Co_{75}Fe_{25}$ and the α-Fe(P) solid solution, respectively. The important grain refinement occurs with a progressive rise in microstrain level as the milling time is prolonged. High density of dislocations induced by severe plastic deformations can be generated with a prolonged milling duration leading to an increase in the micro-hardness of the powder particles as well as an increase in internal micro strains (*Loudjani, et al., 2011*).

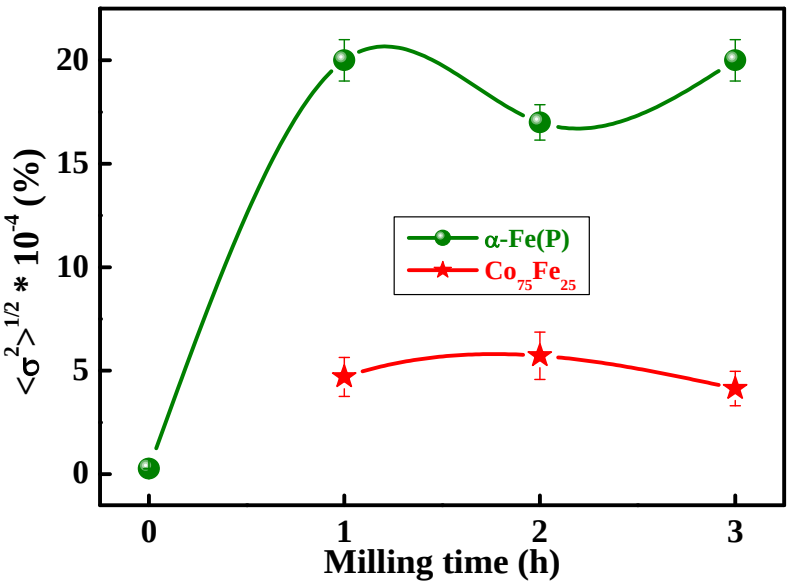

Figure III.9: *Evolution with milling time, of microstrain rate, $<\sigma^2>^{1/2}$, for the α-Fe(P) solid solution and the $Co_{75}Fe_{25}$ phase*

III.3 Effect of Milling time on Stacking Fault Probability

The stacking fault probability (SFP) is one of the most important microstructure defects, which is a measure of deformation faulting. The planar defects, expressed in terms of stacking faults probability, are given by the relation (*Warren, et al., 1950* and *1969*):

$$SFP = [1.5\ (\alpha' + \alpha'') + \beta] \qquad \text{(III.2)}$$

Where α', α'' are the intrinsic and extrinsic deformation faults probabilities, respectively, and β is the twin faults probability.

The SFP in the α-Fe(P) solid solution and the $Co_{75}Fe_{25}$ phase deduced from the Rietveld refinement of the XRD patterns of the $Fe_{15}Co_2P_3$ powder mixtures is shown in Figure III.10.a. For the solid solution, the SFP increases with increasing milling time reaching a value of 8.04×10^{-4} after 3h. This value is higher than that obtained in the binary $Co_{75}Fe_{25}$ phase after the same milling duration. The decrease of this parameter after 2h of milling can be attributed to the annihilation of dislocations to minimize their energy and thus increasing the SFP. It is clear that the dislocation density on $Co_{75}Fe_{25}$ was stable and reached the smallest values of about 2.22×10^{10} m^{-2}. It has been shown that twining and deformation stress depends on the crystallite size (*Meyers, et al., 2001*). The creation of stacking faults by mechanical deformations is closely related to the creation and the reaction of dislocations (*Louidi, et al., 2012*). These results highlights the path of the solid state reactions in this powder mixture, achieved by diffusing P and Co elements in the Fe matrix through the stacking fault and the dislocations induced by the milling process into the solid solution and the $Co_{75}Fe_{25}$ phase. As a host, the bcc α-Fe phase can dissolve P atoms, which create lattice defects such as dislocations and grain boundaries.

According to Warren's formulas, the determination of ordered planes N from the inverse of SFP (N = 1/SFP) indicates the average number of compact atomic planes between two consecutive stacking faults (either deformation or twin-type) (*Sort, et al., 2004*). The average number of layers between two stacking faults of the α-Fe(P) solid solution and the $Co_{75}Fe_{25}$ phase in the $Fe_{15}Co_2P_3$ powder mixtures is presented in Figure III.10.b. N shows that the number of planes between two neighboring stacking faults in the $Co_{75}Fe_{25}$ phase is reduced with milling time. In effect, after 3h of milling, N decreases from 30700 to 16920 planes. The higher value of N indicates that between two stacking faults there are, in average, 62500 ordered planes for the α-Fe(P) solid solution for the unmilled $Fe_{15}Co_2P_3$ powder mixtures. The lower value of N is 1200 ordered for the same solid solution existed in the $Fe_{15}Co_2P_3$ milled for 3h. As it is clear, the values of the average number of layers between two stacking faults in the $Co_{75}Fe_{25}$ phase, are found to be higher compared to those in the α-Fe(P) solid solution. Therefore, it can be inferred that Co facilitates the formation of the binary phase more than the amorphous red P in the formation of the solid solution. Those low values of ordered planes reached in the α-Fe(P) solid

solution, for a long milling time, makes it less stable in comparison to the $Co_{75}Fe_{25}$ phase and drives to its transformation.

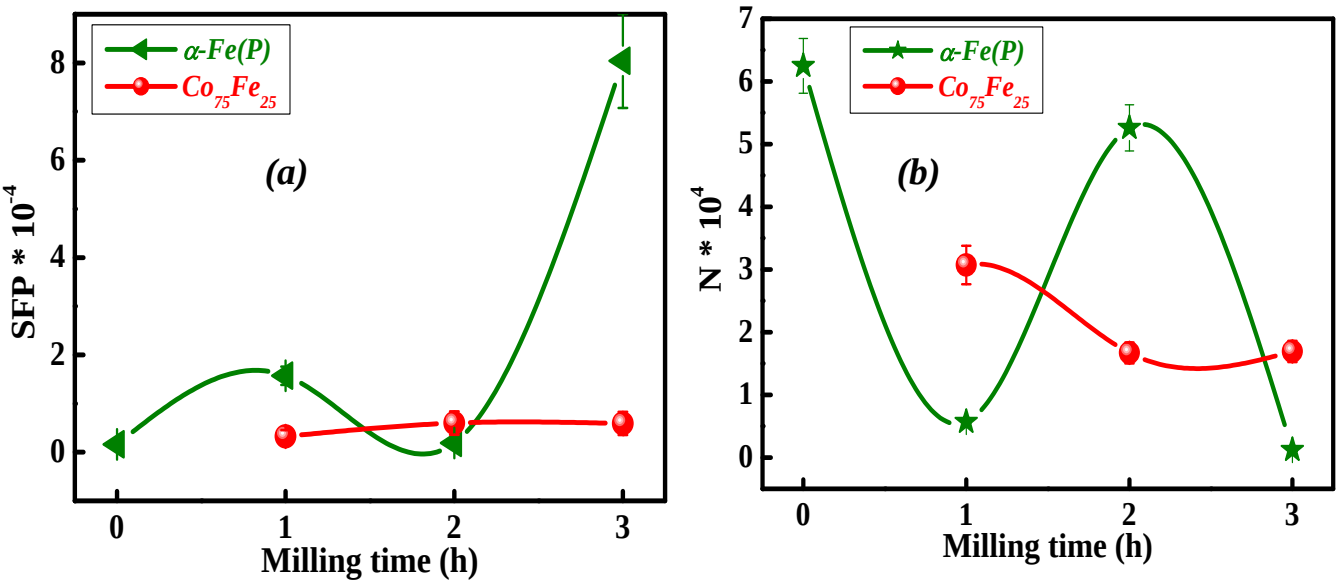

Figure III.10: *Variations with milling time of* ***(a)*** *the stacking fault probabilities and* ***(b)*** *the average number of layers, N, for the α-Fe(P) solid solution and the $Co_{75}Fe_{25}$ phase of the $Fe_{15}Co_2P_3$ powder mixtures during the ball-mill.*

III.4 Dislocations Density

For milled samples subjected to severe plastic deformation by impacts of balls, the dislocation density, ρ, is the main defects besides grain boundaries. The density of dislocation is one of the important parameter influencing the final nanocrystalline microstructure. It was calculated using the following equation (*Hull, et al., 1950*):

$$\rho = 2\sqrt{3}\frac{<\sigma^2>^{1/2}}{<L>B} \qquad \text{(III.3)}$$

Where B is the Burger's vector, equal to $a\sqrt{3}/2$ for the bcc crystallographic phase, the direction of easy dislocations concentration is (1 1 1), <L> is the crystallite size, and $<\sigma^2>^{1/2}$ is the microstrain (r.m.s). <L> and $<\sigma^2>^{1/2}$ are deduced from Rietveld refinement.

The variation of the dislocation density can be associated with the ball-to-powder mass ratio that characterizes the collision number, the energy impact, and the number of defects introduced within the lattice. The severe plastic deformation leads to a developing number of matrix dislocations. The created dislocations are multiplied in the shear zones, as a result of their rearrangement and interactions (*Enayati, et al., 2009*). Figure III.11 illustrates the evolution of the calculated dislocation densities for both α-Fe(P) solid solution and the $Co_{75}Fe_{25}$ phase of the alloyed $Fe_{15}Co_2P_3$. For the α-Fe(P) solid solution, ρ increased to reach a value of 5×10^{14} m^{-2} with the milling time increasing from 0 to 3h. On the other hand, the dislocation density of the $Co_{75}Fe_{25}$ phase was steady and reached the

smallest value of about 0.53×10^{14} m^{-2}. These results highlight the pathway of the solid state reactions in this powder mixture, occurring by diffusing both elemental P and Co within Fe host lattice through stacking faults as well as dislocations induced by the milling process into the solid solution and the $Co_{75}Fe_{25}$ phase. As a host, the bcc α-Fe phase can dissolve P atoms, thereby creating lattice defects such as grain boundaries and hence further increase in the dislocation density.

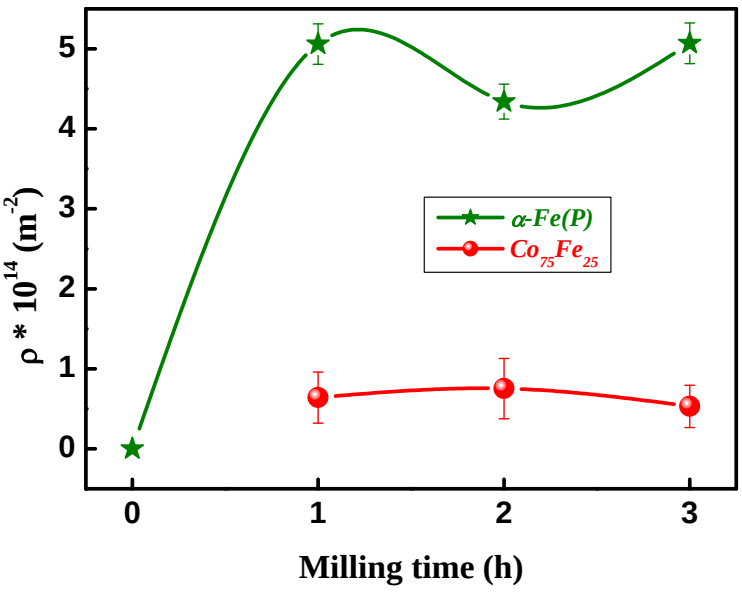

Figure III.11: *Variation, with milling time, of the dislocation density, ρ, for α-Fe(P) solid solution and the $Co_{75}Fe_{25}$ phase in the $Fe_{15}Co_2P_3$ powder mixtures.*

III.5 Mechanical Properties

In general, before any material or any component is utilized, the mechanical properties should be studied thoroughly to ensure the mechanical integrity during use. Young's modulus and Poisson's ratio are crucial parameters of the stiffness matrix in modeling materials subject to thermal and mechanical loading, and to model load transfer between different stacked layers (*Larson, 2013*). Using the MAUD software, it is possible to compute the evolution of the simulated mechanical parameters such as Poisson's ratio *v*, Young modulus E and the calculated bulk modulus, K.

III.5.1 Young Modulus

Young's modulus, E, or the modulus of longitudinal elasticity (the elastic stiffness) describes a material's resistance to stretching or compression during elastic deformation. The modulus of elasticity is a set of physical quantities that characterize the ability of any solid body to be elastically deformed under conditions where force is applied to it. In simple cases, E is defined as the ratio of stress to elongation. When hydraulic fracturing occurs, Young's modulus can be referred to as the amount of

pressure needed to deform the material. Materials with high Young's modulus tend to be very hard but are prone to brittleness. In other words, a low Young's modulus value means a solid is elastic while a high Young's modulus value means a solid is inelastic or stiff.

The highest value of Young modulus, E, in the $Fe_{15}Co_2P_3$ powder mixtures was nearly equal to 200 GPa, which is closed to those for coarsed metals and higher than those of nanomaterials. An example of such materials is nanomaterials obtained for FeCoP nanoglass films which are found to have a Young modulus of up to 138.85 GPa (*Zhang, et al., 2020*). Such results reflect the effect of the addition of the red P powder to the Fe-Co system which decreases Young modulus values compared to the Fe-Co binary alloys. In comparison with the $Fe_{60}Co_{40}$ alloys, Young modulus was estimated to approximately equal 250 GPa (*Vas'ko, et al., 2004*) and have a high value between 611 and 536 MPa for the monolithic FeCo alloy (*Albaaji, et al., 2017*). This can be attributed to the precipitation of the $Co_{75}Fe_{25}$ particles embedded in the α-Fe(P) solid solution during the milling process, resulting in the weakness and rigidness of final powder mixtures because the initial powder mixture was ductile (Co, Fe) — brittle (P) type.

III.5.2 Poisson's Ratio

Poisson's ratio, *v*, is often used to characterize the elastic properties of a material. Poisson's ratio measures the deformation in the material in a direction perpendicular to the direction of the applied force. When a stretching force is applied lengthwise to a solid, the solid starts to stretch. During this stretching, in the vast majority of cases, the cross-section of the material decreases. Poisson's ratio shows how the cross-section of a deformable body changes under lengthwise stretching (or compression). Its value is the ratio of the linear contraction of cross-section e' to the elongation e, mathematically expressed as follows (*Poplavko, 2019*):

$$v = \frac{|e'|}{e} \quad ; \quad v = \frac{\Delta d/D}{\Delta l/L} \qquad \text{(III.4)}$$

When a material undergoes a tensile force F, it occurs a stress according to the applied force. In proportion to the stress, the cross section is decreased by Δd from the diameter D and the length elongates by ΔL from the length L, as illustrated in Figure III.12. When a material is compressed in one direction, it usually tends to expand in the other two directions perpendicular to the direction of compression. This circumstance is called the Poisson effect.

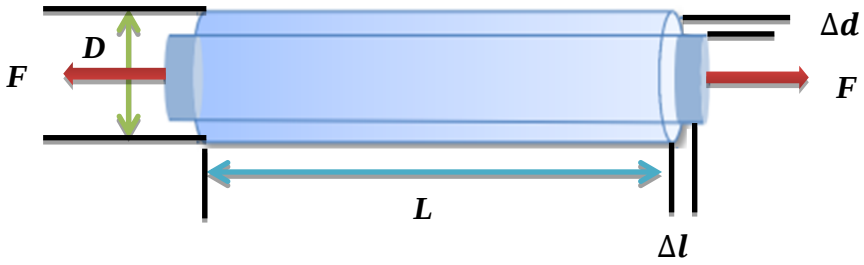

Figure III.12: *Tensile test of a sample.*

Poisson's ratio is dimensionless and ranges from 0.1 to 0.45. In case of an entirely brittle material, Poisson ratio is zero, whereas for a completely elastic material, ν=0.7. A low Poisson's ratio (0.1–0.25) means easier rock fracture whereas high Poisson's ratio (0.35–0.45) indicates the rocks are harder to fracture. Figure III.13 presents the evolution of Poisson's ratio versus milling time. Poisson's ratio, ν, of the $Co_{75}Fe_{25}$ phase had high values during milling. On the other hand, the α-Fe(P) solid solution had lower values gradually decreasing with milling time. Those results exposed the brittle nature of the α-Fe(P) solid solution in comparison with the $Co_{75}Fe_{25}$ phase which is harder to fracture.

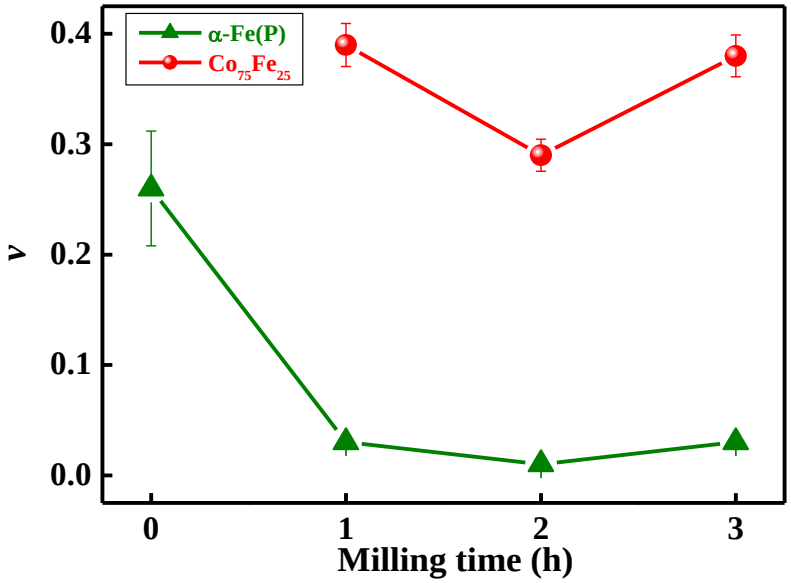

Figure III.13: *Evolution with milling time of Poisson ratio, v, of the $Co_{75}Fe_{25}$ phase and the α-Fe(P) solid solution in the $Fe_{15}Co_2P_3$ powder mixtures.*

III.5.3 Bulk Modulus

The bulk modulus of elasticity K is a parameter quantifying the inverse of compressibility. K results from the reduction of the body's bulk volume that occurs when equal forces are applied to all sides. Moreover, K characterizes the capability of an object to change its volume, for example, under hydrostatic pressure. It should be noted that K of a nonviscous liquid is different from zero, whereas

for an incompressible fluid, it is infinite. The bulk modulus is calculated using the following formula (*Donaldson, et al., 2013*):

$$K = \frac{E}{3(1-2v)} \qquad \text{(III.5)}$$

This equation shows that *v* must remain less than 0.5 for a positive value of K.

The bulk modulus for the α-Fe(P) solid solution rapidly decreased from 137.5 GPa to 70.20 GPa after 3h of milling because increasing the milling duration leads to more hardening work effect which made the α-Fe(P) solid solution brittle (Figure III.14). On the other hand, for the $Co_{75}Fe_{25}$ phase, K decreases after 2h of milling then it increased. The increase in bulk modulus during the last hour of milling is attributed to the refined microstructure; outcomes of the homogeneous distribution of the binder phase through the alloys. The bulk modulus of elasticity for the α-Fe(P) solid solution was less than that of the $Co_{75}Fe_{25}$ phase. These results revealed that the modulus is enhanced by the 3d-transition metals (Fe, Co) present in the $Co_{75}Fe_{25}$ phase.

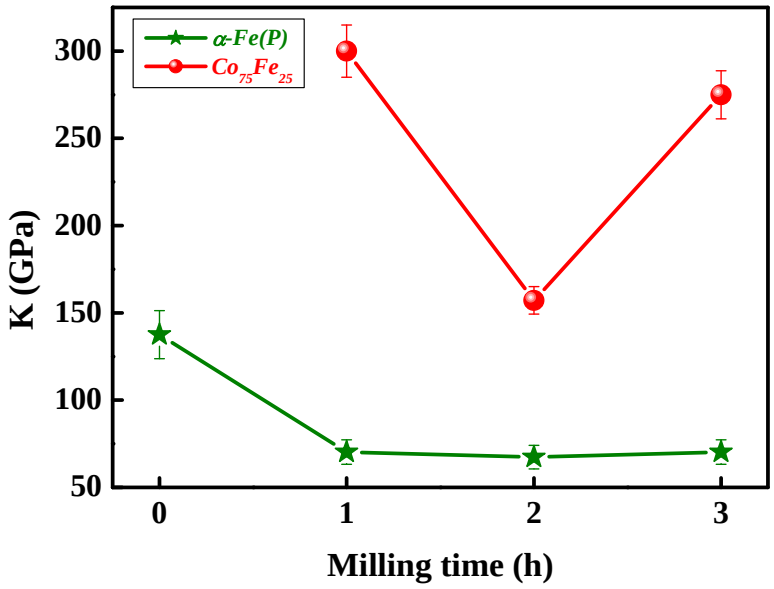

Figure III.14: *Bulk modulus versus milling time for $Co_{75}Fe_{25}$ phase and α-Fe(P) solid solution in the $Fe_{15}Co_2P_3$ powder mixtures.*

III.6 Conclusion

X-Ray spectral and phase composition evolution of the $Fe_{15}Co_2P_3$ powder mixtures were obtained from the MAUD program. During the first hour of milling, the $Fe_{15}Co_2P_3$ powders were subject to heavy plastic deformation accompanied by lattice defects, resulting in an enhancement in the solid state reactions between the diffusion couples (P, Fe) and (Co, Fe) of the reactant materials, leading to the formation of the α-Fe(P) solid solution and the $Co_{75}Fe_{25}$ phase. The crystallite size, structural microstrain and dislocation density of the α-Fe(P) solid solution and the $Co_{75}Fe_{25}$ phase in

the $Fe_{15}Co_2P_3$ mixtures, undergone ball milling for different time periods (0h – 3h), have been investigated in this study using different procedures based on integral breadth analysis of the obtained XRD patterns. Phase changes and the variations in the percentage of phases were also studied. In addition, the mechanical properties were examined to better understand the induced changes in the mechanical parameters of the existing solid solution, the binary phase and the role of milling time.

Based on this study, the following summarized conclusions can be offered:

- The results indicate that mechanical alloying leads to the formation of the α-Fe(P) solid solution and the $Co_{75}Fe_{25}$ binary phase after 1h of milling with bcc structure and Im-3m space group.
- The highest percentage before milling was 75 % for α-Fe then varied with milling time to reach 35% after 3h milling for the α-Fe(P) solid solution. After 3h of milling, the highest value of percentage was 65% obtained by the $Co_{75}Fe_{25}$phase.
- By increasing the milling time, the crystallite size of the α-Fe(P) solid solution remarkably decreases but is nearly stable for the $Co_{75}Fe_{25}$ phase. The crystallite size of the solid solution reached a value of 100.3 nm after 3h of milling. The presence of iron tremendously affects such changes.
- The stacking fault probability of the α-Fe(P) solid solution was clearly higher than that of the $Co_{75}Fe_{25}$ phase. The high values of the SFP reflect an important increase in the dislocations density in the Fe host lattice.
- The mechanical results reveal that the value of Young modulus in the $Fe_{15}Co_2P_3$ powder mixture is smaller than that obtained in binary Fe-Co alloys, reflecting the effect of P addition. Furthermore, the bulk modulus of elasticity for the α-Fe(P) solid solution is less than that of the $Co_{75}Fe_{25}$ phase. These results reflect the brittle nature of the α-Fe(P) solid solution in comparison with the harder to fracture $Co_{75}Fe_{25}$ phase..

Chapter IV:

Magnetic Properties

In this chapter, the magnetic behavior of the $Fe_{15}Co_2P_3$ powder mixture milled for several times is detailed. The dependence of magnetic properties on the structural/microstructural parameters of ball-milled Fe15Co2P3 powder mixtures was investigated.

IV.1 Hysteresis Loops

The effect of mechanical milling on the magnetic behavior as well as the evolution of the magnetic properties of the $Fe_{15}Co_2P_3$ powder mixture milled for 0, 1, 2 and 3h, were examined. The time dependence of the hysteresis loops (M-H) (the magnetization, M, as a function of the external applied magnetic field, H) at room temperature, of the mechanically alloyed $Fe_{15}Co_2P_3$ powder mixtures are illustrated in Figure IV.1 and Figure IV.2. All M-H curves of the nanostructured $Fe_{15}Co_2P_3$ powder mixtures were closed, narrow, saturated and irrespective of the milling time implying their typical ferromagnetic order. All hysteresis cycles exhibited a sigmoidal shape usually observed in nanostructured samples with small magnetic domains. This is due to the presence of structural distortions inside the grains. Generally, fine soft magnetic materials possess a small coercive domain (small hysteresis losses) (*McHenry* and *Laughlin, 2014*). In other words, lower maximum energy product is preferred for soft magnetic materials. This behavior can mainly be related to the microstructural internal deformations, chemical composition, grain size and magnetic anisotropy.

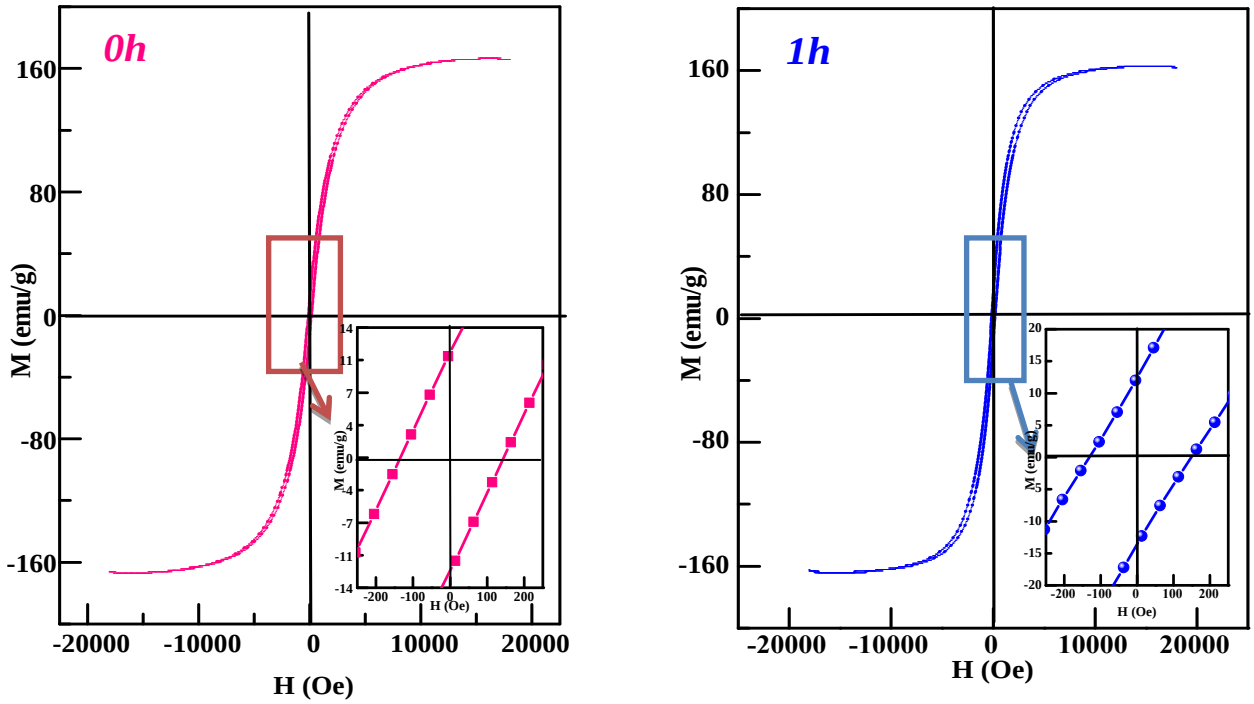

Figure IV.1: *Representative magnetization-field hysteresis loops recorded in the longitudinal configuration and the inset representing M-H curves at low fields for the $Fe_{15}Co_2P_3$ powder mixtures milled for 0h and 1h.*

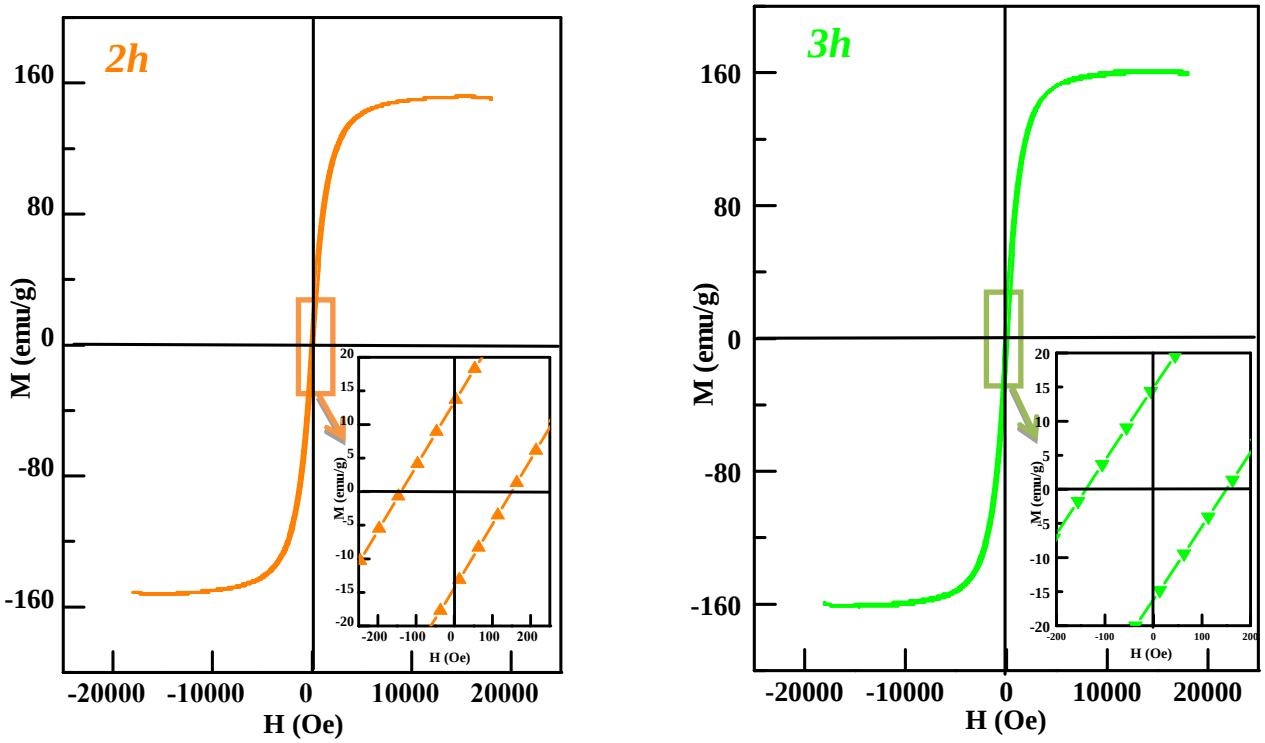

Figure IV.2: *Representative magnetization-field hysteresis loops recorded in the longitudinal configuration and the inset representing M-H curves at low fields for the $Fe_{15}Co_2P_3$ powder mixtures milled for 2h and 3h.*

IV.2 Coercivity

In alloys, the coercivity H_C, is governed by the movement of domain walls and the spin rotation, and hence it can be strongly influenced by the grain refinement. Thus, H_c is often affected by grain size, the lattice internal strain and most type's defects including point defects, grain boundaries, secondary phases and structural defects, precipitates, dislocations, and the redistribution of elements during phase evolution (*Herzer, 2005* and *Kronmüller, 1981*). However, in mechanical milling, the evolution of H_c is due to the internal nanostructure, impurities, pores and defects introduced during alloying. The microstructures obtained after mechanical milling can strongly influence the magnetic properties of the $Fe_{15}Co_2P_3$ powdered alloys (*Herzer, 1990*). The evolution of the average coercive field H_C, and the average crystallite size <L> with alloying time is displayed in Figure IV.3. The average coercive field of the $Fe_{15}Co_2P_3$ powder mixtures remarkably increased with milling time. This continual increase in H_c can also be due to the introduction of internal stresses, structural defects such as the increase in the density of dislocations, as a result of severe plastic deformation of the powders upon milling, which serve as pinning sites for the magnetic domain wall movement that would impede the wall motion (*Souilah, et al., 2012* and *Chermahini, et al., 2009*). As it can be seen in Figure IV.3, the decrease of the average grain size resulting from the competition between fracture and welding can be related to the increase in the coercivity. H_c increased from 144.621 Oe to a higher value of about 150.309 Oe after 3h of milling. This coercivity behavior as a function of the milling time is higher than

that reported by other studies on Fe-Co alloys (*Popova, et al., 2012* ; *Sort, et al., 2004* and *Zeleňàkovà, et al., 2007*), where values of the coercivity were in the range of 25–100 Oe for nanocrystalline FeCo alloys obtained by different methods, including mechanical alloying. H_C of the $Fe_{15}Co_2P_3$ powder mixtures was higher than H_C of the $Fe_{100-x}Co_x$ (x = 55, 50, 45) samples synthesized by high energy ball milling by Bez, et al. (2015) who found an H_C of almost 42 Oe for the $Fe_{45}Co_{55}$ sample. Mebrek, *el al.* (2021) found that the value of H_C for $Fe_{65}Co_{35}$ milled powders was very low and decreased during the ball-mill from ~7.28 Oe to ~1.88 Oe after just 2h and 30 min of milling. The increase of H_C that started just after 1h of milling is due to increased domain-wall pinning attributed to an increased number of grain boundaries (reduced average crystallite size), as determined from XRD analysis. This modest increase of coercivity between 1 and 3h of milling can be caused by the simultaneous diffusion mechanism and the formation of the same binary $Co_{75}Fe_{25}$ as well the α-Fe(P) solid solution during the ball-mill. In the $Fe_{15}Co_2P_3$ composition, a bcc-$Co_{75}Fe_{25}$ phase is completely formed after just 1h of milling and the incorporation of Co-atoms into the bcc-Fe structure increases the residual stresses. Therefore, H_C increases due to the coercivity being an extrinsic property of magnetic materials that strongly depends on the microstructure of the material including the effects of internal defects, residual stresses, grain sizes, and nonmagnetic inclusions, especially when mechanical milling is used to obtain it (*Sánchez-De Jesús, et al., 2016* and *Behvandi, et al., 2010*). Furthermore, the reduction of crystallite size promotes the formation of single magnetic domains which are more difficult to be oriented due to the presence of the α-Fe(P) solid solution and the $Co_{75}Fe_{25}$ phase. This acts as additional obstacles to the magnetic domain wall movement.

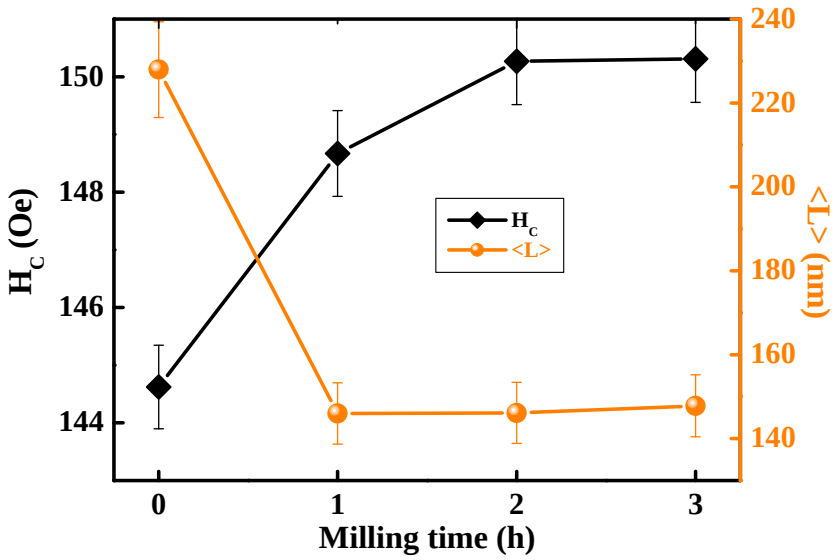

Figure IV.3: *Evolution of the average coercive field, H_C and the average crystallite size, <L>, of the $Fe_{15}Co_2P_3$ powder mixture versus milling time.*

IV.3 Saturation Magnetization

Saturation magnetization, M_s, is another important magnetic parameter which is determined by the nature of the component, and the composition and type of the crystal structure. The variation in M_s with milling time provides additional information on the evolution processes occurring during mechanical milling. The change of saturation magnetization M_S with milling time is depicted in Figure IV.4. It can be seen that M_S decreases rapidly from a higher value of 117.180 emu/g to a minimum value of 82.005 emu/g after 1h of milling. This noticeable decrease of M_S can be attributed to the presence of pure ferromagnetic *bcc*-iron and *hcp*-cobalt before the solid reactions take place, then the formation of the paramagnetic α-Fe(P) solid solution after 1h of milling. When P is alloyed to Fe, the change of the nearest neighbor configuration leads to the reduction of the magnetic moment per atom and therefore to the magnetization reduction. This fact can be explained by the interaction between the Fe metallic atoms which is ferromagnetic with P atoms that are non-ferromagnetic in nature (*Abdellaoui, et al., 1997* and *Bensebaa, et al., 2014*). Moreover, the 3p electrons of P can fill the d shell of Fe through p-d hybridization and suppress the magnetic moment of Fe, and consequently decreases M_S (*Wang, et al.,2013*). Furthermore, the decrease of M_S can be related to the dilution effect of the magnetic moment of cobalt atoms promoted by the formation of the binary $Co_{75}Fe_{25}$ phase. In fact, in correlation with XRD analysis, the alloying of non-ferromagnetic P atoms with the two ferromagnetic elements Co and Fe atoms leads to the formation of the solid solution and the $Co_{75}Fe_{25}$ binary phase by diffusion mechanism. This has been confirmed during the early hours of mechanical milling. The diffusion of Co in Fe matrix induces the transformation of charges between the Co and Fe atoms (*Yuping, et al., 2014*). It is known that the chemical composition, local environment of the magnetic atoms and their electronic structure have strong influence on M_S (*McHenry, et al., 1999*). Also, the refinement of grain size during the ball-mill and increasing the fraction of grain boundaries leads to the increase in the average inter-atomic distances between the neighboring atoms, weakens their exchange interaction, and consequently can contribute to the M_S diminution upon milling (*Taghvaei, et al., 2012*). M_S increases gradually to 97.340 emu/g after 3h, which can be attributed to the combined effects associated with the decrease of the proportion of the α-Fe(P) solid solution, the increase of the proportion of the ferromagnetic $Co_{75}Fe_{25}$ phase and the refinement of microstructures. This effect dominantly arises from alloying Co of smaller magnetic moment of 1.72 μB with Fe, which has a larger magnetic moment of 2.2 μB, as well as the formation of the $Co_{75}Fe_{25}$ binary phase with strong ferromagnetic exchange interaction (*Ling, et al.,2014*). M_s values were lower than those obtained from the $Fe_{100-x}Co_x$ (x = 55, 50, 45) samples by Bez, et al. (2015) who found that M_s was more than 200 emu/g for all the milled samples. Sánchez-De Jesús, et al. (2016) also found higher values for hcp-$Fe_{70}Co_{30}$ and bcc-$Fe_{30}Co_{70}$ of 225 emu/g and 154 emu/g, respectivly.

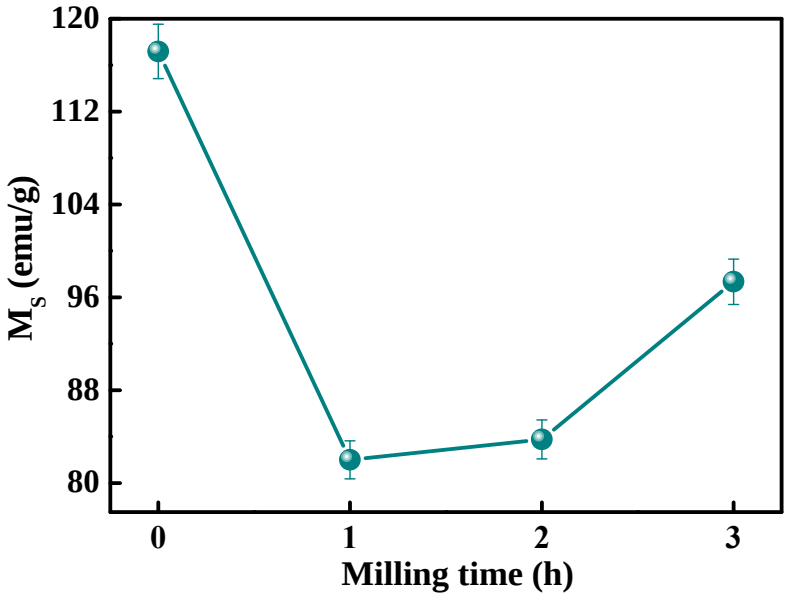

Figure IV.4: *Evolution of the saturation magnetization, M_s with the milling duration of the $Fe_{15}Co_2P_3$ powder mixtures.*

IV.4 Squareness

Once the M_r and M_S values for the $Fe_{15}Co_2P_3$ powder mixture milled for several times are determined, we can infer the squareness (the remanence ratio) by taking the ratio of M_r over M_S. M_r/M_s is an important parameter in the determination of the magnetic energy and the type of the magnetic domain. The squareness values are plotted against milling time in Figure IV.5. The behaviour of the M_r/M_s is almost similar to that of H_C. Effectively, the continuous increase in the squareness of $Fe_{15}Co_2P_3$ correlates with the increase in H_C observed in the alloys. The rise of the magnetic squareness ratio can be linked to the crystallization process that leads to the increase in magnetic anisotropy; the lower the $Fe_{15}Co_2P_3$ squareness, the higher the anisotropy in the alloys. Such lower values of M_r/M_s, ranging from 0.070 to 0.092 are less than 0.1 indicating that the small magnetic particles are typically single domains (*Fallot, 1936*). Azzaza, et al. (2006) found that the $Fe_{50}Co_{50}$ nanostructured powder prepared by high-energy ball milling behaves as a soft ferromagnetic with lower values of the squareness ratio (less than 0.065) as compared to those obtained for the $Fe_{15}Co_2P_3$ powder mixtures.

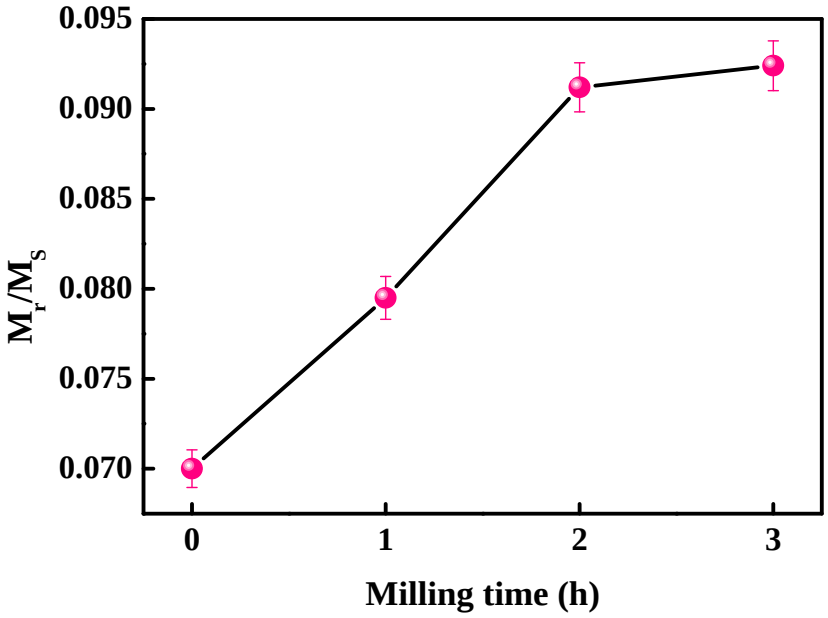

Figure IV.5: *Values of the squareness ratio, M_r/M_s, of $Fe_{15}Co_2P_3$ powder mixture versus milling time.*

IV.5 Magnetocrystalline Anisotropy Constant

The magnetocrystalline anisotropy constant k is an intrinsic property calculated using the relation between the saturation magnetization, M_S, and coercivity, H_C, as follows (*Zubair, et al., 2017)*:

$$k = \frac{H_C \times M_S}{2} \qquad \text{(IV.1)}$$

Figure IV.6 presents the magnetocrystalline anisotropy constant k as a function of the milling time. After 1h of milling, k reduced from a higher value of 8.473 × 10^3 erg/cm^3 of the un-milled powders to a minimum value of 6.095 × 10^3 erg/cm^3. As expected, the maximum value of the magnetocrystalline anisotropy constant is achieved by the un-milled mixture contining Co atoms, because it crystallizes in a hexagonal crystal structure (*hcp*) that has an uniaxial crystalline anisotropy higher than that of the materials with cubic structures (*bcc*), obtained after 1h of ball-mill. The reduction in k values indicates the existence of weak grain to grain interactions in these powder mixtures. Furthermore, the diminution in the anisotropy of magnetocrystalline in the first hour of milling is caused by the gradual reduction of crystallite size at the same hour, which is promoted by the mechanical energy generated by the high-energy ball milling thereby facilitating the rotation of the magnetic vector, the average effect of magnetization over the randomly oriented nano-sized grains and also the diffusion of P atoms in Fe matrix that leads to the formation of the α-Fe(P) solid solution (*Loudjani, et al., 2016*). Afterwards, k increases to 7.315 × 10^3 erg/cm^3 at 3h of milling due to the formation of the ferromagnetic $Co_{75}Fe_{25}$ phase with higher proportions. However, this value is smaller than that of the un-milled sample.

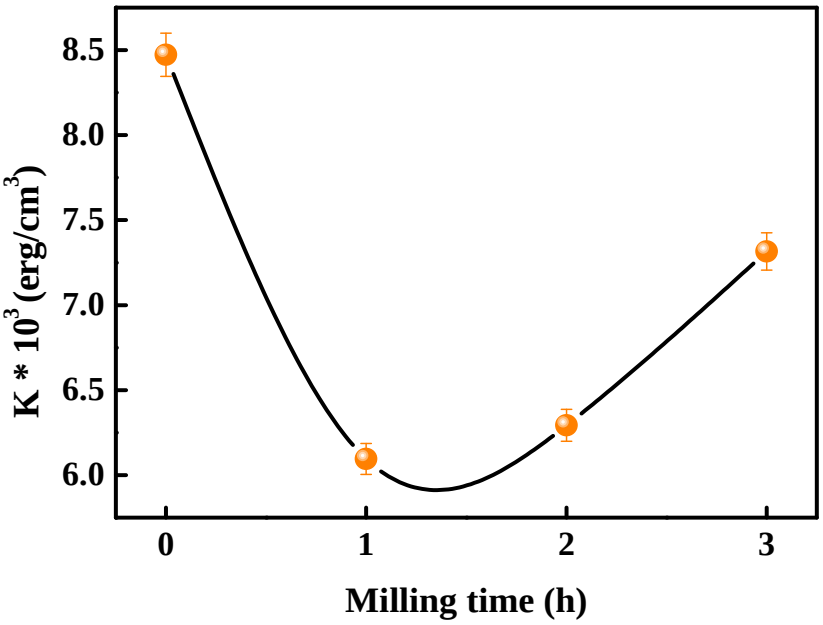

Figure IV.6: *Magnetocrystalline anisotropy constant, k, as a function of the milling time.*

IV.6 Maximum Energy Loss

Energy losses are the chief technical parameter by which the properties of a soft magnetic material are evaluated. The milling effect on the maximum energy loss $Q_{h,}$ in the 2nd and 4th quadrant of the hysteresis loop is shown in Figure IV.7. A very small hysteresis loss is implied by the resulting narrow hysteresis loop. This type of loss strongly depends on the crystallite size, residual stresses, and density of the material. According to the obtained results, the hysteresis loss for the $Fe_{15}Co_2P_3$ powder mixtures shows a higher value of 6.94×10^{-3} erg/cm^3 in the un-milled powder mixture due to the large crystallite size. The hysteresis loss decreased in the first hour of milling following an important reduction in the crystallite size (*Shokrollahi* and *Janghorban, 2006*) and then increased with further milling to reach the same value at 2 and 3h. The number of pinning centers influences the domain structure to a lesser extent, resulting in a moderate increase in energy loss. This increase occurs when the hampered domain wall moves during the milling process while the dislocation density increases due to plastic deformations (*Permiakov, et al., 2004*). The existence of a small gap either between the powder particles where the excitation field created in the alloy by the external field is in the intragranular pores and not in the particles of the magnetic circuit thus inducing energy losses (*Boukeffa, et al., 2021*).

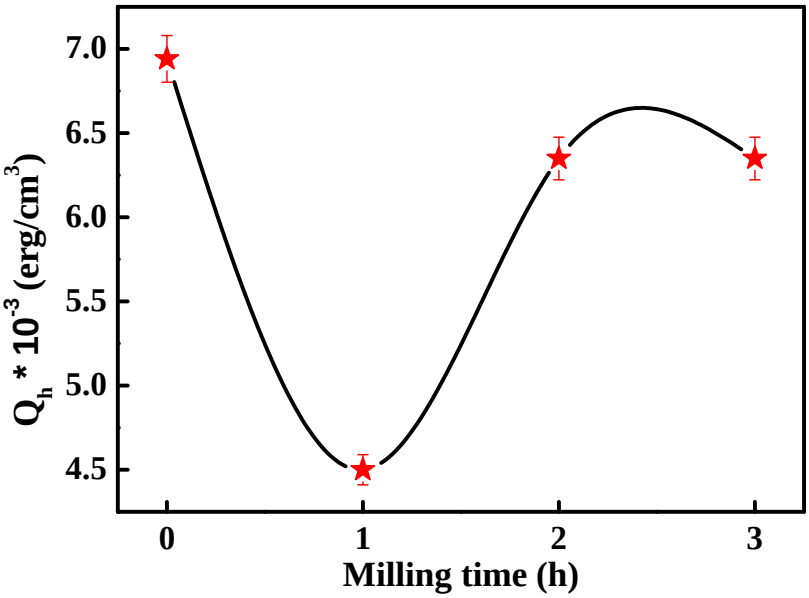

Figure IV.7: *Evolution with milling time of maximum hysteresis loss energy, Q_h.*

IV.7 Maximum Magnetic Permeability

The permeability is one of the most characteristic and important parameters for soft magnetic materials since it indicates the magnetic induction generated by the material in a given magnetic field. It is related to two different magnetization mechanisms; the spin rotation and the domain wall rotation. Furthermore, the permeability is a microstructure sensitive parameter, affected by the shape, density and porosity of the particle and strongly depends on grain size (*Hamzaoui, et al., 2006* and *Shokrollahi, 2009*). Figure IV.8 shows the evolution, during the ball-mill of the maximum magnetic permeability, μ_{max}, of the $Fe_{15}Co_2P_3$ powder mixtures. μ_{max} decreased to a minimum value of 49.302×10^{-3} emu/g/Oe during the first hour of milling as a result of the formation of the α-Fe(P) solid solution and the $Co_{75}Fe_{25}$ phase at the same hour. Subsequently, μ_{max} increased and reached a maximum permeability value about 65.441×10^{-3} emu/g/Oe at 3h of milling. This could results from the presence of the nonmagnetic P element in the α-Fe(P) solid solution in the $Fe_{15}Co_2P_3$ powder mixtures, which acts like an air gap as a source of the demagnetizing field causing the existence of very mobile domain walls thus increasing the maximum permeability. It is well known that the addition of P content increases the permeability (*Kordecki, et al., 1982* and *Manna, et al., 2014*). Also, the reason for the increased permeability is likely to be due to the increase in the ferromagnetic $Co_{75}Fe_{25}$ phase proportions. In fact, the finer grain size in soft materials, the lower magnetic properties due to the higher concentration of grain boundaries acting as pinning sites for domain walls that prevent their movement during the magnetization process (*Mazeeva, et al., 2020*).

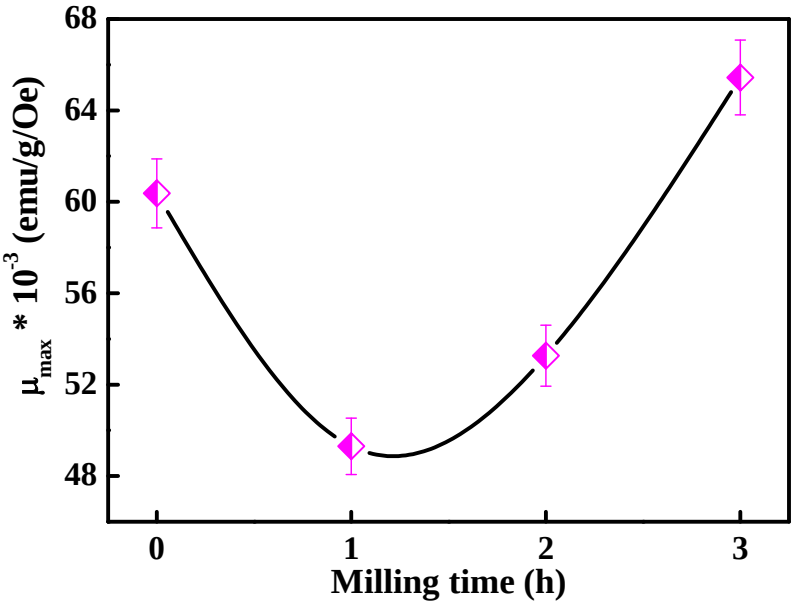

Figure IV.8: *Evolution with milling time of maximum magnetic permeability, μ_{max}.*

The values of the average remanent magnetization M_r, the nucleation field H_n, the switching field distribution SFD, are listed in Table IV.1.

The M_r of the un-milled powder mixture was estimated to be 8.242 emu/g and reached a minimum of 6.525 emu/g, after 1h of milling. Due to the crystal defects induced during milling and lattice distortion, the M_r followed an abrupt change in the milled samples. It reached a maximum value of 9.384 emu/g in 3h milled powder.

Nucleation means that a magnetization state becomes unstable and the change in the magnetization configuration starts at the nucleation field H_n. The nucleation field increases during the ball-mill as showed in Table IV.1. H_n reached values close to the coercive field H_c ($H_n \approx H_c$), indicating that our mixture powder is almost a perfect magnet.

The switching field distribution, SFD, is an important micromagnetic characteristic curve in the magnetic recording media that depends on the degree of alignment of particles along the easy axis in a texture (*Sebt* and *Akhavan, 2001*). It is supposed that the extracted SFD from macroscopic measurements rely on separating the contributions to the measurements of the intrinsic SFD and the extrinsic effects of magnetostatic and exchange interactions (*Ruta, et al., 2017*). The characteristic features of interphase exchange coupling are illustrated by switching field distribution via dH/dH_c (Table IV.1), where dH is the field between 0.5 M_r and −0.5 M_r and H_c is the coercivity. The distribution of the switching field showed a higher value at 1h of milling (a typical characteristic of

soft phases) indicating the magnetization reversal is completed in one step for this powder mixture. Consequently, the width of the dH/dH_c peak can be interpreted as an estimation of the efficiency of hard/soft interphase exchange coupling.

Table IV.1: *More magnetic measurements as a function of milling duration of the $Fe_{15}Co_2P_3$ powder mixtures.*

Milling time (h)	***M_r (emu/g)***	***H_n(Oe)***	***SFD***
0	8.242	144.62	1.02
1	6.525	148.67	1.12
2	7.64	150.27	1.03
3	9.384	150.31	1.03

IV.8 Conclusion

The magnetic measurements have been obtained using a vibrating sample magnetometer (VSM). The magnetic properties of mechanically alloyed materials can notably be influenced by the ball-mill process due to the stresses and defects generated during milling together with a consequent grain size reduction that results in enhanced magnetic behavior. The effect of milling time on the magnetic properties of the $Fe_{15}Co_2P_3$ powder mixtures have bee studied. The results indicate that:

- A narrow hysteresis loop suggests a very low hysteresis loss. All the magnetization curves displayed similar soft magnetic features of the $Fe_{15}Co_2P_3$ powder mixtures.
- The reduction in the crystallite size affects many magnetic parameters such as the coercive field and the remanence ratio which vary proportionally with the milling time. This is accompanied by an enhancement of the microstrain ratio.
- The M_S of the powders continuously decreased from a higher value of 117.18 emu/g after 1h of milling to a lower value of 97.340 emu/g after 3h of milling. It has been demonstrated that the simultaneous changes in the lattice strain and crystallite size determine the variation in H_C of the powders during milling.
- The magnetocrystalline anisotropy constant and the maximum magnetic permeability showed similar changes during the ball-mill.
- The different magnetic parameters such as the average remanent magnetization, the SFD and the nucleation field have been determined as function of milling time.
- The simultaneous changes in the lattice strain, the average crystallite size and the proportion of the α-Fe(P) solid solution and the $Co_{75}Fe_{25}$ phase determine the variation in the magnetic parameters of the powder mixtures during milling.

Chapter V

Effect of $Fe_{15}Co_2P_3$ Powder Mixtures on Test-Bacteria Growth

In this chapter, $Fe_{15}Co_2P_3$ nanostructured powders were monitored by bacterial cell growth tests. The quantitative analysis was evaluated using optical density measurements to study the effect of powder mixtures on four bacterial strains (*Staphylococcus (α), Staphylococcusaureu, Klebsiella pneumonia and Haemophilus influenzae).* The influence of concentration, average grain size and magnetic saturation on bacteria growth is also discussed, in details.

V.1 Effect of $Fe_{15}Co_2P_3$ Powder Mixtures in Growth of Test Gram-Positive and Gram-Negative Bacteria Strains

The qualitative bacteriological assay of the synthetized $Fe_{15}Co_2P_3$ nanostructured powders, milled for 0, 1, 2 and 3h on bacteria strains, was studied. Growth curves are presented by OD_{600} values as a function of the incubation time. A close study of the growth of the four species *Streptococcus (α)*, *Staphylococcus aureus, Klebsiella pneumoniae* and *Haemophilus influenzae*, used as models for Gram-positive and Gram-negative bacteria strains respectively, was conducted with different concentrations of the powder mixtures at the same temperature in the same laboratory environment.

V.1.1 Effect of the Un-milled $Fe_{15}Co_2P_3$ Powder Mixtures on the Growth of Bacteria Strains

In Figure V.1, cell growth in the test variants prepared with both Gram-positive and Gram-negative bacteria strains in terms of optical density is given for the un-milled $Fe_{15}Co_2P_3$ powder mixture with different concentrations. A good bacterial growth for both Gram-positive cells was observed in the presence of different concentrations of the un-milled $Fe_{15}Co_2P_3$. There was an increase in viability with the passage of time, as compared with the results of the control treatment (bacterial incubation without powder mixture 0.00 mg/mL). It is well noted that the un-milled powder mixture with different concentrations had no effect on these bacteria strains. The highest value of the optical density, OD, was about 0.347 registries for the contact of *Streptococcus (α)* with 0.22 mg/mL (Figure V.1a). During kill time analysis, *S.aureus* treated with the un-milled $Fe_{15}Co_2P_3$ powder mixture showed an optical density of about 0.55 after 24h of incubation (Figure V.1b). The bacteriological activity indicated that the un-milled mixture powder with higher concentrations clearly improved the growth of these Gram-positive strains producing reliable good growth curves with these strains. Pure Fe, red P and especially the Co presented on the un-milled $Fe_{15}Co_2P_3$ powder mixture could not impede both Gram-positive bacteria strains. Besides, little information is available in the literature on the bacteriological activity of metallic pure iron and cobalt nanoparticles without conjugation with other materials. The un-milled $Fe_{15}Co_2P_3$ with higher concentrations can easily be taken up by *Streptococcus (α)* and *S.aureus* and also used as a growth factor. The results of the optical density measurement after treatment of the un-milled $Fe_{15}Co_2P_3$ powder mixture showed that the growth of *Klebsiella* strains is completely stopped in the presence of high concentrations of the un-milled powder mixture (1.66 mg/mL), which was improved by the slight decrease in the OD values and completely stopped after 24h of incubation **(**Figure V.1c). The un-milled powder mixture caused the death of *K. pneumonia* strains. The highest value of OD was about 0.18 obtained from 0.22 mg/mL of the un-milled powder mixture. Figure V.1d shows that the un-milled $Fe_{15}Co_2P_3$ powder mixture caused the death of the Gram-negative bacteria *H.influenzae*. As observed from this figure, bacteria showed no

significant decrease with an increase in the un-milled $Fe_{15}Co_2P_3$ powder mixture with different concentrations, compared to the control which reached growth values close to zero.

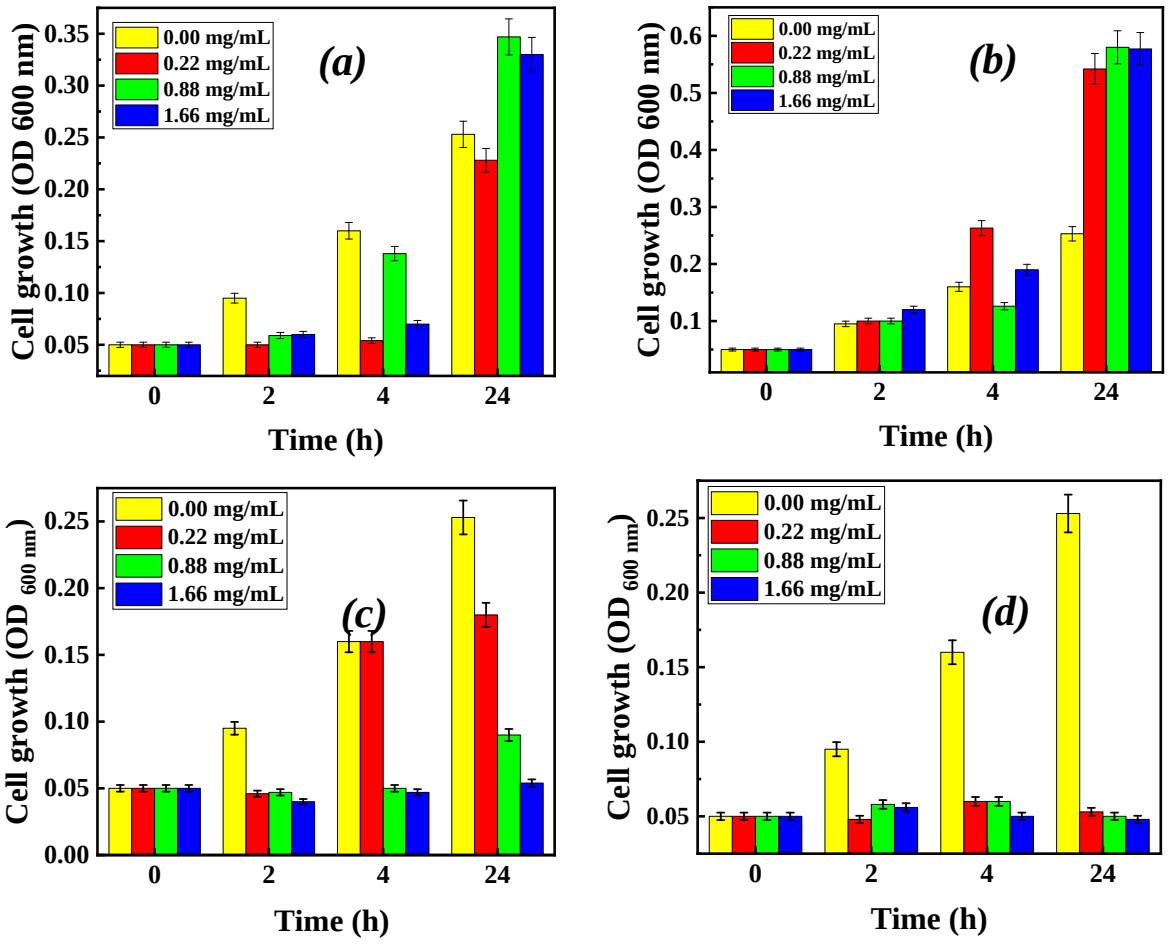

***Figure V.1**: Effect of the un-milled $Fe_{15}Co_2P_3$ powder mixture on **(a)** Streptococcus (α), **(b)** Staphylococcus aureus, **(c)** Klebsiella pneumoniae* and ***(d)** Haemophilus influenzae.*

V.1.2 Effect of $Fe_{15}Co_2P_3$ Powder Mixture milled for 1h on the Growth of Bacteria Strains

Cell growth in the test variants prepared with both Gram-positive and Gram-negative bacteria strains in terms of optical density for the $Fe_{15}Co_2P_3$ powder mixture milled for 1h with different concentrations is illustrated in Figure V.2. *Streptococcus (α)* in contact with this powder mixture showed no significant change in the optical density (Figure V.2a). A clear diminution was observed in the optical density after 2h of incubation until the end of the incubation period (24h) for different concentrations compared to the control. The highest values of OD were about 0.1 obtained due to 0.22 mg/mL concentration of this product after 2, 4 and 24h of incubation. Many studies considered the use of complex nanostructured systems based on cobalt and iron, such as $CoFe_2O_4$ nanoparticles (*Gheidari, et al., 2020* and *Venkatesan, et al., 2015*), and Co-doped TiO_2 nanostructures (*Hosseini-Zori, 2018*), which have presented a good antimicrobial behavior in Gram-positive bacteria with

remarkable efficacy against this pathogen responsible for serious infections. However, Figure V.2b, shows a good cell growth of *Staphylococcus aureus* in contact with the 1h milled $Fe_{15}Co_2P_3$ powder mixtures with different concentrations after 24h of incubation. This powder mixture improved the growth of this strain. The highest values of OD were about 0.55 obtained by 0.88 mg/mL concentration of this product after 24h of incubation of *S. aureus*. On the other hand, the increase in the concentration of the $Fe_{15}Co_2P_3$ powder mixture milled for 1h increases the growth of both Gram-negative bacteria strains after 24h of incubation (Figure V.2c and Figure V.2d). Based on such observations, it can be suggested that increasing the concentration of this powder mixture leads to a good growth of *K. pneumonia and H. influenzae* strains compared to the control plates. The highest values of OD were about 0.45 and 0.29 obtained, respectively, from *Klebsiella* and *Haemophilus* after 24h of incubation in contact with 1.66 mg/mL of the $Fe_{15}Co_2P_3$ powder mixture milled for 1h. This product clearly improves the growth of these Gram-negative strains and results in reliable good growth curves with the strains. The $Fe_{15}Co_2P_3$ powder mixture milled for 1h can easily be taken up by *K. pneumonia* and *H. influenzae* and also used as a growth factor. Therefore, this powder mixture was not effective against these bacteria strains.

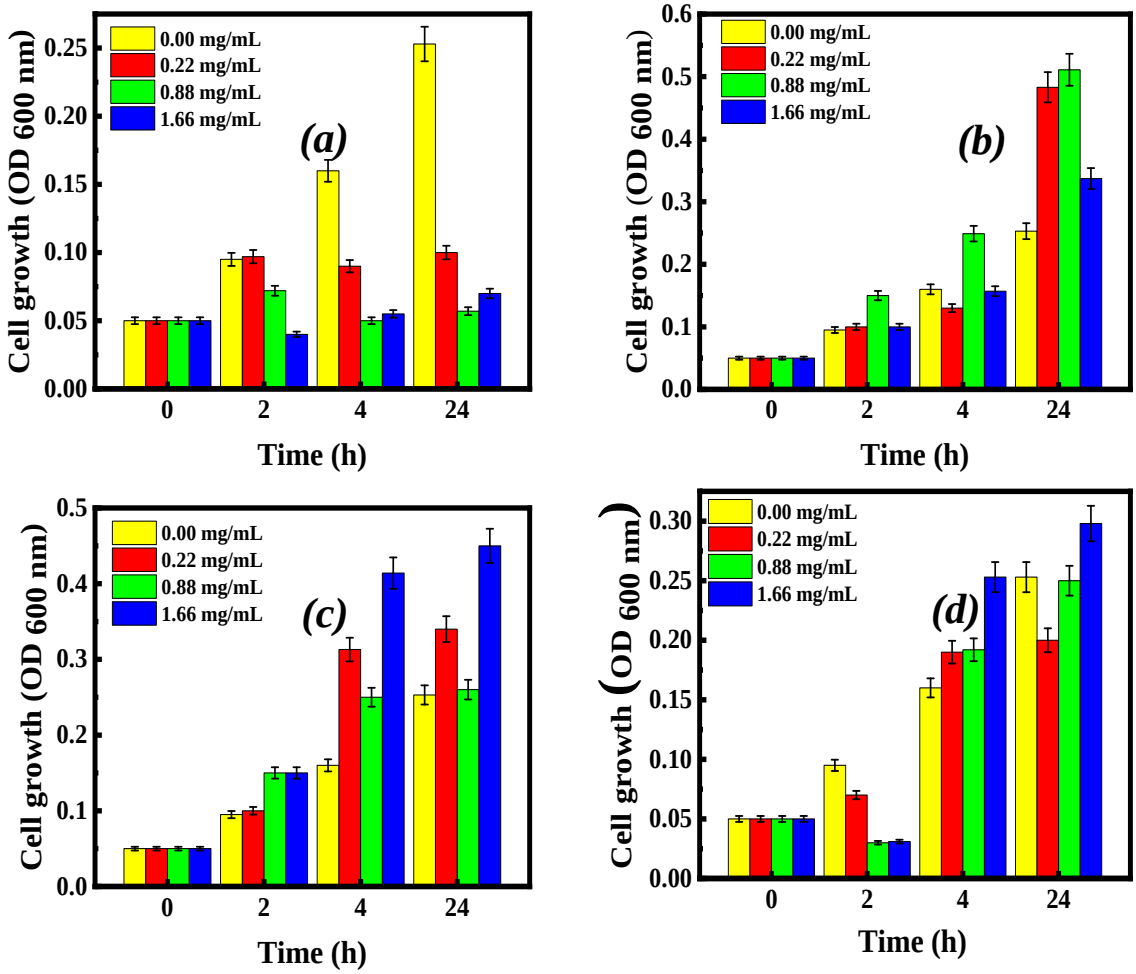

***Figure V.2**: Effect of $Fe_{15}Co_2P_3$ powder mixture milled for 1h on **(a)** Streptococcus (α), **(b)** Staphylococcus aureus, **(c)** Klebsiella pneumoniae* and ***(d)** Haemophilus influenzae.*

V.1.3 Effect of $Fe_{15}Co_2P_3$ Powder Mixture milled for 2h on the Growth of Bacteria Strains

The four bacteria strains have been in contact with the $Fe_{15}Co_2P_3$ powder mixture milled for 2h and incubated for 2, 4 and 24h. Bacteria cell growth was followed and the obtained results are shown in Figure V.3. The $Fe_{15}Co_2P_3$ powder mixture milled for 2h improved *Streptococcus (α)* death with the incubation duration compared to the control (0.00 mg/mL of the product), as shown in Figure V.3a. Nevertheless, the increase in the concentration of the powder mixture improved the growth of *Staphylococcus aureus* bacteria strain after 24h of incubation (Figure V.3b). The highest value of OD for this product was about 0.18 for both concentrations of 0.88 and 1.66 mg/mL after 24h of incubation. The increase in the concentration of the $Fe_{15}Co_2P_3$ powder mixture milled for 2h led to a good growth of Gram-negative bacteria strains compared to the control plates (Figure V3.c and Figure V.3d). After 24h of incubation, the values of OD are about 0.39 and 0.20 obtained from *Klebsiella* and *Haemophilus* in contact with 1.66 mg/mL of $Fe_{15}Co_2P_3$ powder mixture milled for 2h. The $Fe_{15}Co_2P_3$ powder mixture milled for 2h can easily be taken up by *K. pneumonia* and used as a growth factor.

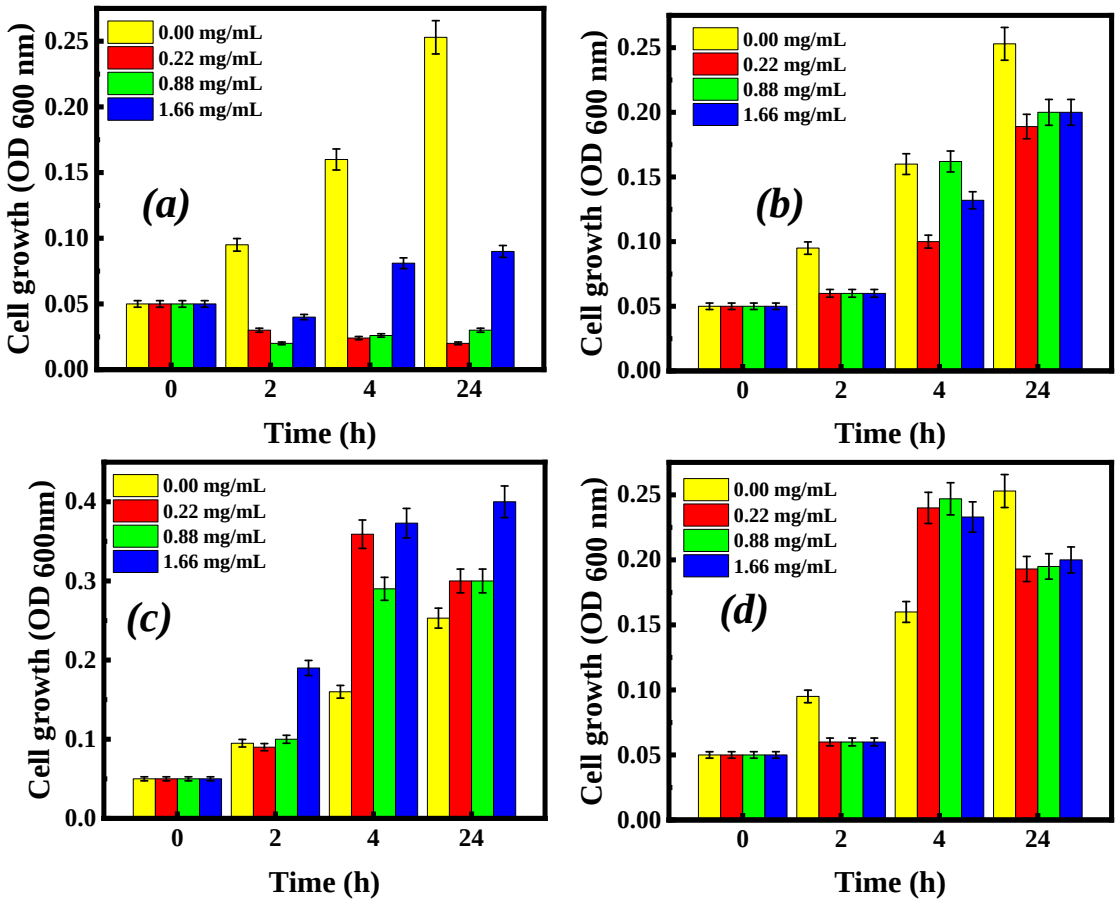

***Figure V.3**: Effect of $Fe_{15}Co_2P_3$ powder mixture milled for 2h on **(a)** Streptococcus (α), **(b)** Staphylococcus aureus, **(c)** Klebsiella pneumoniae* and ***(d)** Haemophilus influenzae.*

V.1.4 Effect of $Fe_{15}Co_2P_3$ Powder Mixture milled for 3h on the Growth of Bacteria Strains

In Figure V.4, cell growth in the test variants prepared with the four bacteria strains is given for the $Fe_{15}Co_2P_3$ powder mixture milled for 3h with different concentrations. It was noticed that this powder mixture with different concentrations killed *Streptococcus (α)* with further negative influence on the cell metabolism and consequently on cell multiplication as compared to the control (Figure V.4a). However, the same powder mixture remarkably improved cell growth; it can be used by *Staphylococcus aureus* in its metabolism (Figure V.4b). Based on such finding, it can be suggested that increasing the concentration of this product leads to a good growth of the *S. aureus* strain. The highest value of OD was about 0.25 obtained in contact with a 1.66 mg/mL of this powder mixture. Figure V.4c and Figure V.4d, clearly show a good growth of bacterial density in samples containing the same powder mixture. This means that this powder mixture improves the growth of *K. pneumoniae* and *H. influenzae*. It can be concluded that the growth increases by increasing the concentration of this powder mixture. The highest values of OD after 24h of incubation of *Klebsiella* and *Haemophilus* were 0.29 and 0.32 in contact with 0.22 mg/mL and 0.88 mg/mL of this mixture, respectively. The results could be related to the presence of iron and phosphorus in the $Fe_{15}Co_2P_3$ powder mixtures, which are essential for Gram-negative pathogen growth (*Palmer, et al., 2016* and *Sheldon, et al., 2016*).

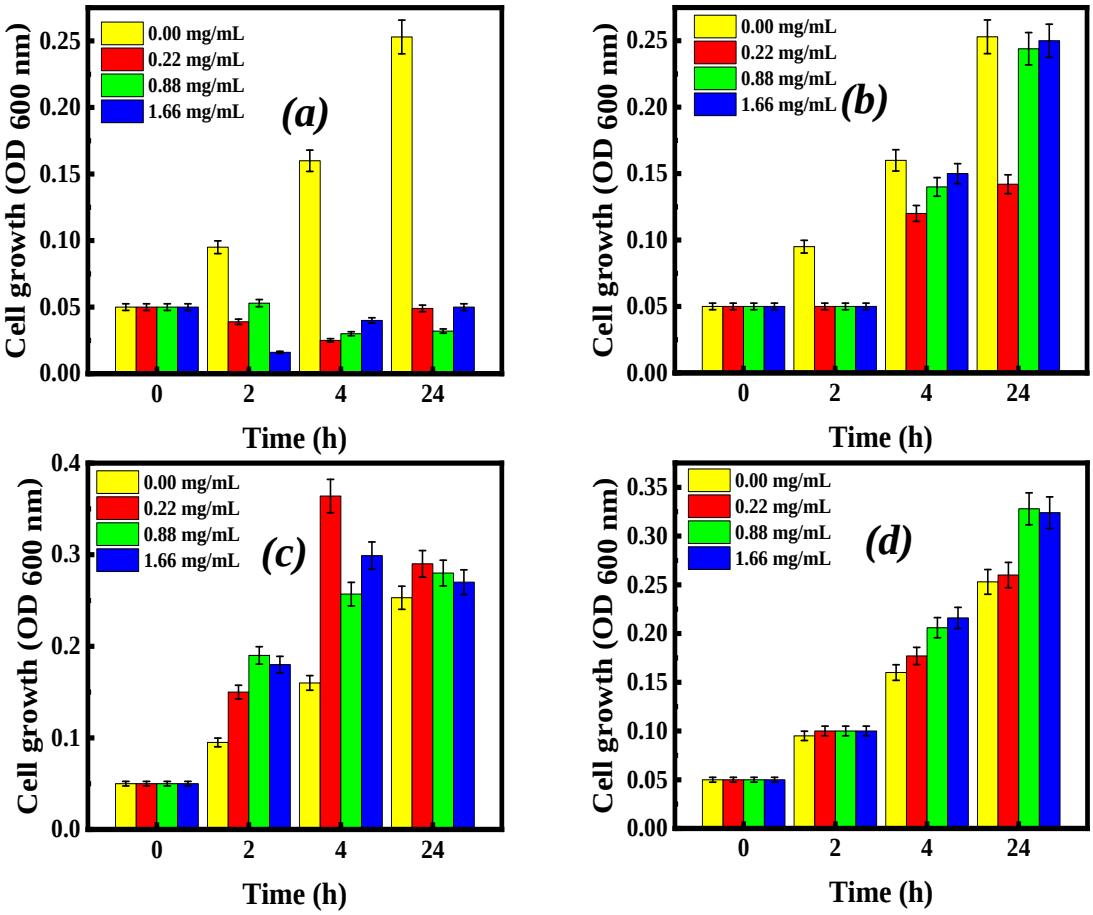

***Figure V.4**: Effect of $Fe_{15}Co_2P_3$ powder mixture milled for 3h on **(a)** Streptococcus (α), **(b)** Staphylococcus aureus, **(c)** Klebsiella pneumoniae* and ***(d)** Haemophilus influenzae.*

V.2 Effect of the Average Crystallite Size on Bacterial Cell Growth

In order to study the effect of crystallite size <L> of the $Fe_{15}Co_2P_3$ powder mixtures on different bacteria strains, the obtained OD_{600} was gathered for the same 1.66 mg/mL concentration of different $Fe_{15}Co_2P_3$ powder mixtures milled for several durations after 24h of incubation with all bacteria strains (Figure V.5). An excellent correlation was demonstrated between OD and <L>. The optical density decreased with the decrease of the average crystallite size during milling for both Gram-positive strains *Streptococcus (α)* and *S. aureus* (Figure V.5a). This good bacterial activity of $Fe_{15}Co_2P_3$ powder mixtures could result from the penetration of the small crystallite size into *Streptococcus (α)* and *S. aureus* members. Many studies have demonstrated that the small size of nanostructured materials can also contribute to bactericidal effects. For example, Makhluf, et al. (2005) and Yamamoto (2001) reported that the decrease in MgO and ZnO particle size could increase the antibacterial activity against *S. aureus*. It is therefore evident that the crystallite size affects the antibacterial activity. i.e. in order to increase the antibacterial activity, the average crystallite size must be reduced. On the other hand, for the Gram-negative strains *K. pneumonia* and *H. influenzae*, the optical density increases with the decrease in the average grain size (Figure V5.b). Both Gram-negative strains can use the milled $Fe_{15}Co_2P_3$ mixture like a cofactor for their growth. Hence, the interaction of the powder mixtures toward microbial cell wall would be more intense if the crystallite size was smaller. The results of the bacterial activity showed similar tendency in the powder mixtures milled for 1, 2, and 3h. Therefore, the results can be explained by cell wall differences between Gram-positive and Gram-negative bacteria strains that interfere with the interaction with the $Fe_{15}Co_2P_3$ powder mixtures. This could be because Gram-positive and Gram-negative bacteria strains have different cell wall structures, cell physiology, metabolism and degree of contact. The cell wall in Gram-positive bacteria such as *Streptococcus (α)* and *S. aureus* has a peptidoglycan layered cell wall that facilitates the direct interaction between the $Fe_{15}Co_2P_3$ powder mixtures and the bacterial outer membrane and kills them smoothlier than the cell wall of Gram-negative bacteria cells, like *K. pneumonia* and *H. influenzea.* Such wall has another thick cell wall and different external membrane that contains lipopolysaccharides, the porin channels and a thin peptidoglycan which covers a layer of those Gram-negative bacteria cells (*Banner, et al., 2020*; *Slavin, et al., 2017* and *Matthew, et al., 2005*). As a consequence, it can be concluded that nanomaterials' bacteriological behavior is strongly size dependent (*Bagherzade, et al., 2017*)

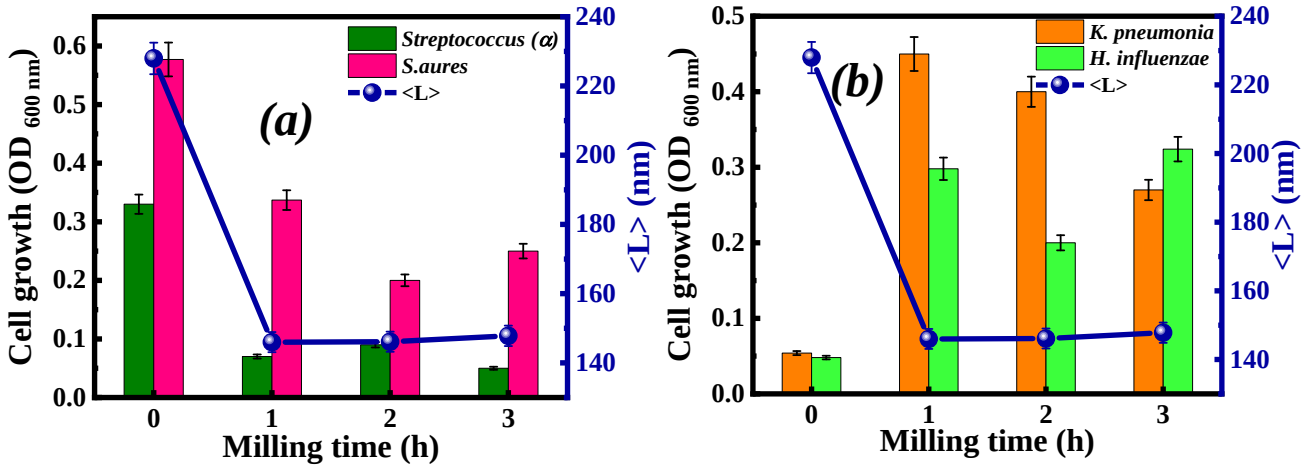

Figure V.5: *Evolution with milling time of the average crystallite size, <L> and the optical density, OD_{600} overtime at concentrations of 1.66 mg/mL, for $Fe_{15}Co_2P_3$ powder mixtures after 24h of incubation on* ***(a)*** *Gram-positive and* ***(b)*** *Gram-negative strains.*

V.3 Effect of the Saturation Magnetization on Bacterial Cell Growth

Magnetic nanoparticles and magnetic nanomaterials have been of importance since the successful use of magnetically labeled antibodies for cell separation and growth of test bacteria (*Whitesides, et al., 1983*; *Kemsheadl and Ugelstad, 1985* and *Stolyar, et al., 2019*). Investigation of magnetic nanomaterials in vitro has ushered modern antibacterial studies into an increasingly attractive research area. A study of the induced effect of the milled $Fe_{15}Co_2P_3$ powder mixtures with their saturation magnetization values on bacterial growth was performed in Figure V.6, comparing the effect of the saturation magnetization on Gram-positive and Gram-negative bacteria strains. Figure V.6 presents the evolution of saturation magnetization, M_S, and the optical density, OD_{600}, with milling time at a concentration of 1.66 mg/mL of the $Fe_{15}Co_2P_3$ powder mixtures on various bacterial strains after 24h of incubation. The OD decreases with the decreasing saturation magnetization during ball milling for both Gram-positive strains (Figure V.6a). The results indicate that the saturation magnetization of the powder mixtures gives a measurable change in the growth rates of both Gram-positive bacterial species. Wang, et al. (2011) have demonstrated the viability of silver-coated magnetic nanoparticles for achieving effective bacterial inactivation efficiency, comparable to and better than silver nanoparticles conventionally used. It is well known that inorganic metallic-based core–shell nanomaterials, especially iron oxide magnetic nanomaterials are able to disrupt pathogen membranes and generate reactive oxygen species, which cause mitochondrial damage (*Tokajuk, et al., 2017*). However, for Gram-negative strains, OD increases with decreasing saturation magnetization (Figure V.5b). This shows that the lower the saturation magnetization value leads to a good growth of

Klebsiella and *Haemophilus*. Interestingly, iron, in this case, is required for the growth of many bacteria and phosphorus is an essential component of all living systems. The good cell growth of *K. pneumonia* and *H. influenzae* can be due to the existence of iron in the milled $Fe_{15}Co_2P_3$ powder mixtures, which is a transition metal essential for Gram-negative pathogen growth (*Palmer, et al., 2016* and *Sheldon, et al., 2016*). Magentic nanomaterials and nanoparticles with antimicrobial properties can find application in water treatment facilities of any liquid wastes (household, industrial, medical) (*Stolyar, et al., 2019*).

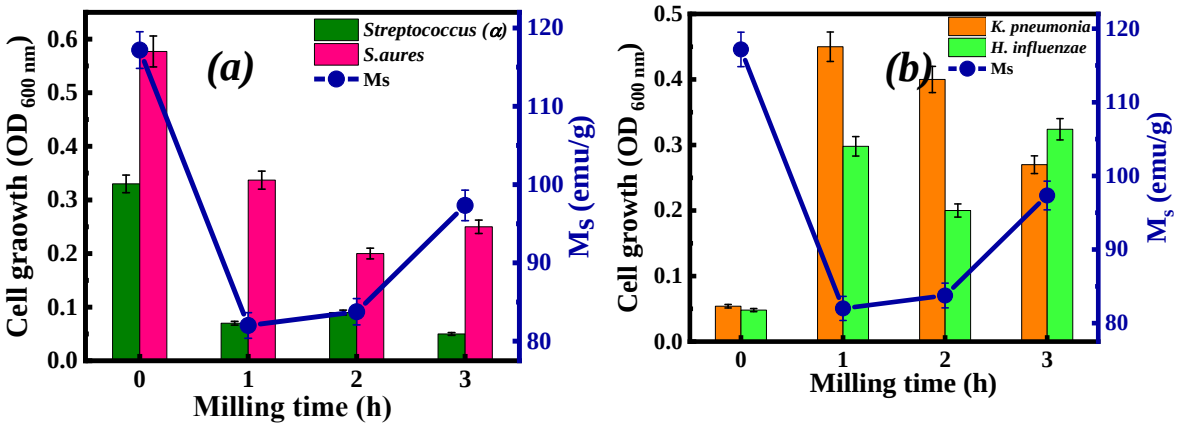

Figure V.6: *Evolution with milling time of saturation magnetization, $M_S$and the optical density, OD_{600} overtime at concentrations of 1.66 mg/mL, of $Fe_{15}Co_2P_3$ powder mixtures on* ***(a)*** *Gram-positive strains and* ***(b)*** *Gram-negative strains after 24h of incubation.*

V.4 Conclusion

The current study provides evidence that the $Fe_{15}Co_2P_3$ powder mixtures prove several benefits:

- The un-milled $Fe_{15}Co_2P_3$ powder mixture gives rise to cell growth of the Gram-positive strains with different concentrations. The un-milled $Fe_{15}Co_2P_3$ powder mixture can be used like a cofactor for *Streptococcus (α)* and *S. aureus* strains but the same powder mixture have showed better antibacterial activity against Gram-negative *K. pneumonia* and *H. influenzae* bacteria strains.
- The addition of the $Fe_{15}Co_2P_3$ powder mixtures milled for 1, 2 and 3h killed *Streptococcus (α)* with further negative influence on the cell metabolism and consequently on cell multiplication.
- *Staphylococcus aureus* can use the $Fe_{15}Co_2P_3$ powder mixtures milled for 1 and 3h like cofactors for a good bacteria growth. However, $Fe_{15}Co_2P_3$ milled for 2h inhibited the growth of this bacteria strain.
- *K. pneumonia* and *H. influenzae* are most resistant when treated with the $Fe_{15}Co_2P_3$ powder mixtures milled for 1h, 2h and 3h. This milled $Fe_{15}Co_2P_3$ can be used like a cofactor with different concentrations for the examined Gram-negative bacteria strains.

- The milling time periods play an important role in the formation of homogeneous nanostructured materials with smaller crystallite size, and hence, the smaller the crystallite size the good bacteriological behavior of the powder mixture.
- Saturation magnetization plays an important role in the bacteriological behavior of the milled powder mixtures in contact with the four bacteria strains. The decrease in saturation magnetization of the $Fe_{15}Co_2P_3$ powder mixtures leads to cell death of Gram-positive bacteria strains especially *Streptococcus (α)*. However, the lower saturation magnetization values of the powder mixture increase the growth of Gram-negative bacteria strains.

General Conclusions and Future Outlook

The first objective of this thesis deals with the synthesis of the $Fe_{15}Co_2P_3$ powder mixtures using mechanical milling process. This robust non-equilibrium technique allows the elaboration of nanocrystalline powders and leads to significant changes in the phase diagram of the FeCoP system. The effect of the mechanical milling time, that ranged from 0 to 3h, on the evolution of the structural, mechanicaland magneticproperties, as well as on bacteria cell growth of mechanically produced $Fe_{15}Co_2P_3$ powder mixtures prepared from elemental Fe, Co and red P powders, has been investigated. Qualitative and quantitative phase analysis of XRD patterns were performed by means of the Rietveld method using the MAUD program. The magnetic measurements were obtained using the VSM and the effect of the concentration and the average grain size of $Fe_{15}Co_2P_3$ powder mixtures on cell growth test have been discussed in terms of optical density using the UV-Vis spectrophotometer. The obtained results can be summarized as follows:

- ✓ From the XRD analysis, the α-Fe(P) solid solution and the $Co_{75}Fe_{25}$ binary phase with a body centered cubic structure forms in the first hour of milling. This phenomenon is confirmed by the progressive decrease of peaks' intensity as well as the remarkable peak broadening with milling time. The powder-ball collisions generate severe plastic deformations and high level of crystal defects promoting the mutual diffusivity of elements.
- ✓ The unit cell volume expansion of the newly formed binary $Co_{75}Fe_{25}$ phase is higher than that of the α-Fe(P) solid solution.
- ✓ The crystallite size gradually decreases reaching 100.3 nm for the α-Fe(P) solid solution but is nearly stable for the $Co_{75}Fe_{25}$ binary phase.
- ✓ The mechanical results reflect the brittle nature of the α-Fe(P) solid solution in comparison with the $Co_{75}Fe_{25}$ phase (harder to fracture).
- ✓ The milled $Fe_{15}Co_2P_3$ alloy powder exhibits a soft ferromagnetic characteristics where the magnetic parameters are sensitive to the milling time, mainly due to the average grain size refinement as well as the formation the of α-Fe(P) solid solution and the $Co_{75}Fe_{25}$ phase.
- ✓ Both the coercivity (H_c) and the squareness ratio (M_r/M_s) increase with the milling time.
- ✓ The saturation magnetization (M_s) and the magnetocrystalline anisotropy constant (k) have showed the same evolution during the ball-mill, attaining the values of M_s = 97.340 emu/g and k = 7.315×10^3 erg/cm^3 after 3h of milling.
- ✓ The Un-milled $Fe_{15}Co_2P_3$ powder mixture has a good growth for *Streptococcus (α)* and *S. aureus* Gram-positive strains. The milled $Fe_{15}Co_2P_3$ powder mixture for different durations 1, 2 and 3h killed *Streptococcus (α)* and *S. aureus* bacteria strains. This powder mixture have showed better antibacterial activity against *Streptococcus (α)* strain.
- ✓ The same un-milled powder mixture killed both Gram-negative *K. pneumonia* and *H. influenzae* bacteria strains. The milled $Fe_{15}Co_2P_3$ powder mixture for different durations 1, 2

and 3h gave a rise in the growth of both *K. pneumonia* and *H. influenzae* strains. Therefore, it can be used like a cofactor for both examined Gram-negative strains.

Further research should be carried out using Mössbauer spectroscopy in order to investigate more magnetic parameters of the $Fe_{15}Co_2P_3$ powder mixtures. In addition, a detailed study on the thermal, morphological properties and the antifungal activity of $Fe_{15}Co_2P_3$ powder mixtures is to be completed.

Appendix

A.1 Fundamental Properties of Pure Elements

The elemental powders used to synthetize our $Fe_{15}Co_2P_3$ powder mixtures were iron, red phosphorus and cobalt. Some properties of each pure element are given bellow in Table A.1.

Table A.1: *Fundamental properties of Fe, Co and red P.*

Properties	***Iron (Fe)***	***Cobalt (Co)***	***Red phosphorus (P)***
Atomic number	26	27	15
Chemical series	Transition metal	Transition metal	Non-metal
Density (g/Cm^3)	7.86 at 25°C	8.9 at 25°C	2.34 at 25°C
Hardness	4	5	---
Atomic properties			
Electronic configuration	[Ar] $3d^6 4s^2$	[Ar] $3d^7 4s^2$	[Ne] $3s^2 3$
Atomic radius (nm)	0.125	0.167	0.128
Atomic mass (g.mol^{-1})	55.845 ±0.002	58.93	30.973 ± 5
Crystalline structure	bcc	Hcp	bcc
Crystalline parameters(nm)	a = 0.286	a = 0.251 , c = 0.405	a = 0.229
Physical properties			
State at 20°C	Solid	Solid	solid
Melting point (°C)	1535	1495	416
Boiling point (°C)	2750	2900	-
The molar heat of fusion (°C)	14.9	16.2	
Other properties			
Magnetic structure	Ferromagnetic	Ferromagnetic	Diamagnetic
Elastic modulus (GPa)	200	211	128
Electronegativity	1.83	1.88	2.19
Specific heat (J/kg°C)	449	435	800
Electricalconductivity (Sm^{-1})	9.93×10^6	17×10^6	$1{,}0\times10^{-9}$
Thermal conductivity (wm^{-1}K^{-1})	80.2	69.21	0.235
Others	Reactive, unstable,	Unstable, magnetic, toxic, absorbs.	Stable, insoluble, reactive, nontoxic.

A.2 Equilibrium Diagrams

A.2.1 Fe-Co (Iron-Cobalt) System

The constitution of the Co-Fe alloys is reproduced in Figure A.1. The system is characterized by an extensive solid solution range between fcc γ(Fe) and fcc γ(Co) and a wide α-Fe solid solution region, which transforms via a second order reaction into the ordered CsCl type phase FeCo. Cobalt exists in two allotropic forms, a closed-packed hexagonal (ε) stable at temperatures below 421°C, and a face-centred cubic (α) stable at higher temperatures (*Betteridge, 1982*). A peritectic reaction at 1494°C decreases smoothly to a shallow minimum at 1476°C and about 65 at.% Co. The allotropic transformation γ/ε occurs over a wide range of temperatures (around 400°C), obviously owing to the small differences in Gibbs energy of the two modifications and the relatively low temperature. A thermodynamic analysis of the fcc/hcp transformation in ternary Fe-alloys leading to the relative stability of ε(Fe) was undertaken by Ishida and Nishizawa (*Ishida, et al., 1974*). They could evaluate the effect of iron on the fcc/hcp transformation of pure cobalt. The addition of cobalt to iron hardly raises the α/γ transformation temperature between 0 and 8 at. %Co (*Fischer, et al., 1970*). The temperature then rises very slowly to a maximum at about 970°C and ~ 45 at. %Co. Further additions of Co decrease the transformation temperature rapidly whilst increasing the (α+γ) two phase field. The γ/ε(Co) transformation, with relatively low differences in Gibbs energy coupled with low diffusion rates owing to the relatively low temperature, make equilibration a slow process resulting in substantial discrepancies between the various observations. However, more recent information has been used, mainly data pertaining to the order/disorder reactions. The disordered fcc γ-Fe phase transforms to a disordered bcc α-Fe phase via a first order reaction, while α-Fe transforms at the maximum temperature of about 733°C ~48 at. % Co (*Oyedele, 1970*) via a second order reaction into an ordered CsCl type phase FeCo. It is known that ordered iron-cobalt alloys exhibit anomalous behavior near 550°C. Cobalt exists in two allotropic forms, a closed-packed hexagonal (ε) stable at temperatures below 421°C, and a face-centred cubic (α) stable at higher temperatures (*Betteridge, 1982*). There is an eutectoïd transformation at 250°C. Additions of iron to cobalt may lead to the formation of a brittle, ordered α' phase which is stable at room temperature in alloys containing between 25-75 wt.% Fe . Table A.2 shows the Co-Fe crystal structure data.

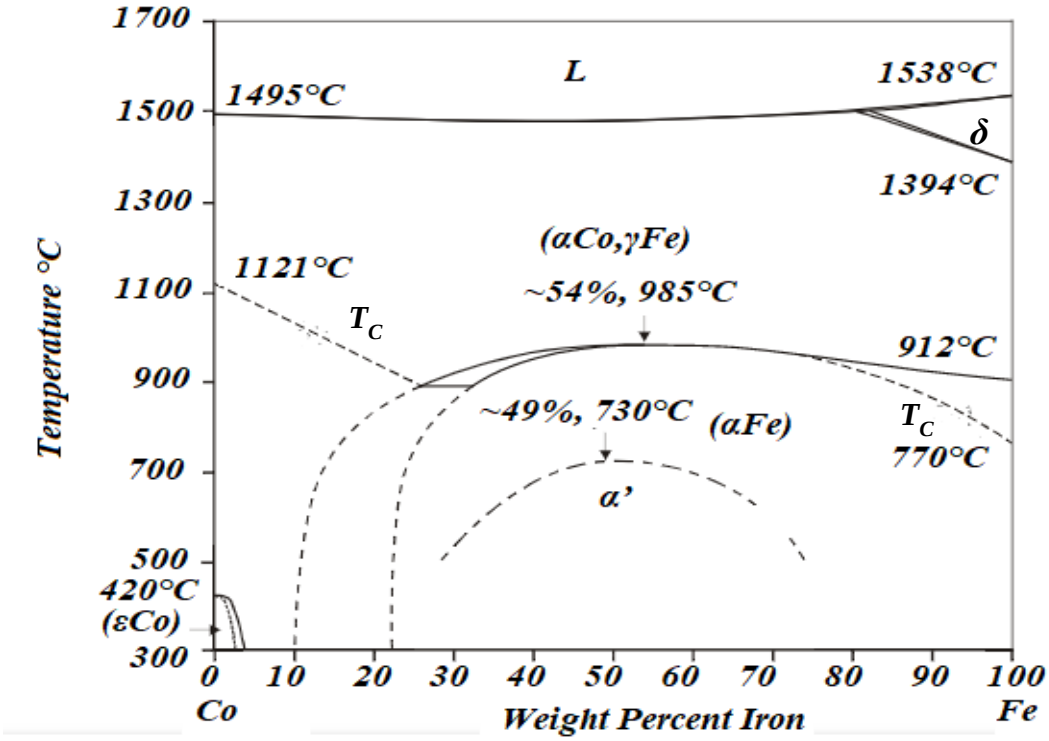

Figure A.1: *Phase diagram of the Fe-Co system (Massalski and Okamoto, 1990).*

Table A.2: *Co-Fe crystal structure data (Okamoto, 2008).*

Phase	***Pearson symbole***	***Space group***
(αCo, γFe)	*cF4*	*Fm-3m*
(δFe)	*cI2*	*Im-3m*
(αFe)	*cI2*	*Im-3m*
(εCo)	*hP2*	*$P6_3/mmc$*
α'	*cP2*	*Pm-3m*

A.2.2 Fe-P (Iron-Phosphorus) System

Experimental studies on the phase equilibrium and thermodynamic properties of the Fe-P system were reviewed by Okamoto (Figure A.2) (*Massalski and Okamoto, 1990*), who proposed a partial diagram of the Fe-P system in the Fe-rich region. The Fe-P system was thermodynamically optimized in the full composition range and five stoichiometric phosphides including Fe_3P, Fe_2P, FeP, FeP_2 and the existance FeP_4 between 627 °C and 927 °C (*Jeitschko* and *Braun, 1978*) and the (γFe), (αFe) solid solutions,were considered. The melting temperature of Fe is 1538°C. The crystal structure information

of all solid phases in the Fe-P system is summarized in Table A.3. The Fe-richest eutectic was placed at 16.9 at.% P and 1048°C, the metastable eutectic at 18.7 at. % P and 930°C (melts with more than 16.7 at. % P tends to form unstable states, if solidification takes place too quickly). The δFe↔γFe and γFe↔αFe transformation temperatures are 1394 and 912°C, respectively. The melting point of δFe is 1538°C. The solid solubility of phosphorus in iron is below 1000°C (*Hofmann, et al., 1970* and *Takayama, et al., 1981*). The assessed maximum solubility of P in (γFe) is 0.56 at.% is at ~ 1150°C. The solid solubility of P in (αFe) decreases as the temperature decreases. The most common form of P is αP (white). The melting point and the boiling point temperatures of αP are 44.14 and 277°C, respectively. The thermal stability of the P-rich phosphide compounds such as FeP_2 and FeP_4 were estimated to be much higher than those of Fe_3P, Fe_2P and FeP. High-order phosphides FeP_2 and FeP_4 were considered stable till at least 1544°C. The L↔(αFe) + Fe_3P eutectic temperature was reported as ~ 980°C. The Fe_3P considered the melting to be congruent at 1104°C. However, subsequent investigations showed peritectic melting occurs at the temperature of 1166°C. The L↔Fe_2P + FeP eutectic temperature is 1262 or 1265°C. The enthalpies, $\Delta_r H$ and entropies, $\Delta_r S$ of the dissociation are for some reactionswere given in Table A.4. The estimated values of enthalpies of formation, $\Delta_f H$ (298) and heat capacity, *Cp* for Fe_3P and Fe_2P are given in Table A.5.

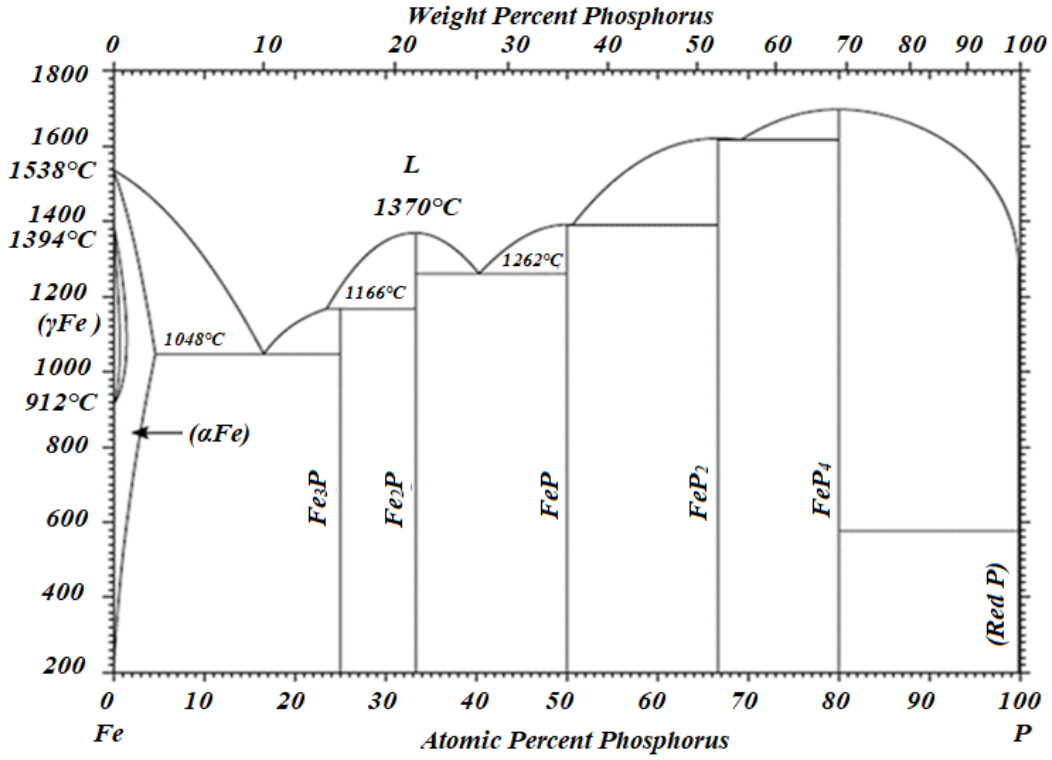

Figure A.2: *Phase diagram of the Fe-P system (Massalski and Okamoto, 1990).*

Table A.3: *Summary of crystal structure information of all phases in the Fe-P system, space group and enthalpy of formation, ΔH^S (You, 2020 ; Brahimi, 2019).*

Phase	***Structure***	***Type***	***a(nm)***	***b(nm)***	***c(nm)***	***Space group***	ΔH^S
α-Fe	*Cubic (bcc)*	---	*0,2866*	---	---	$Im\bar{3}m$	---
γ-Fe	*Cubic (fcc)*	---	*0,3591*	---	---	$Fm\bar{3}m$	---
Fe_3P	*Tetragonal*	*Ni_3P*	*0,9100*	---	*0,4460*	$I\bar{4}$	*–164,0*
Fe_2P	*Hexagonal*	*Ni_2P*	*0,5852*	---	*0,3453*	$P\bar{6}2m$	*–160,2*
FeP	*Orthorhombic*	---	*0,5191*	*0,5790*	*0,30983*	*Pna21*	*–138,1*
FeP_2	*Orthorhombic*	*FeS_2*	*0,4973*	*0,5657*	*0,27235*	*Pnnm*	*–220,9*
FeP_4	*Monclinic*	---	*0,4619*	*1,3670*	*0,7002*	*P21/c*	---

Table A.4: *The enthalpies, $\Delta_r H$ and entropies, $\Delta_r S$ of the dissociation of some reactions.*

Reaction	$\Delta_r H$ ***(KJ)***	$\Delta_r S$ ***(J/K)***
$2FeP_2 \leftrightarrow 2FeP + P_{2(g)}$	259.4 ± 8.5	221.3 ± 4.5 $(531\ to\ 973°C)$
$4FeP \leftrightarrow 2Fe_2P + P_{2(g)}$	354.8 ± 8.5	210.5 ± 4.2 $(727\ to\ 2125\ °C)$

Table A.5: *The estimated values of enthalpies of formation, $\Delta_f H$ (298) and heat capacity, Cp for Fe_3P and Fe_2P*

Compound	***Reaction of formation***	***Cp (J/mol. K)***	***$\Delta_f H$ (298) (kJ/mol)***
Fe_3P	*$3Fe + \alpha P \leftrightarrow Fe_3P$*	*$117.11 + 13.067 \times 10^{-3}T - 17.78 \times 10^5 T^{-2}$ (25 to 1166°C)*	*-164.01 ± 8.4*
Fe_2P	*$2Fe + \alpha P \leftrightarrow Fe_2P$*	*$76.73 + 17.046 \times 10^{-3}T - 6.054 \times 10^5 T^{-2}$ (25 to 1370°C)*	*-160.25 ± 8.4*

A.2.3 Co-P (Cobalt-Phosphorus) System

The assessed partial Co-P phase diagram (Figure A.3), is based primarily on the data of *Żemczużny, et al.* (*1909*). The equilibrium phases of the Co-P system are: rich phase in phosphorus CoP_3, equimolar intermediate CoP with *orthorhombic* structure and Co_2P phase rich in cobalt. The melting point of cobalt is 1495°C. The CoP compound, with a melting temperature higher than 1000 °C, is an amonoclinic compound formed at a high pressure phase rich in phosphorus CoP_2, and the cubic intermediate phase CoP_3. The Co_2P phase with an extended homogeneity range at higher temperatures, is stable up to its congruent melting temperature of 1386 °C. Co_2P rich in cobalt, contain the eutectic α-Co + Co2P at 20 at.%P, which melts at 1023°C (*Żemczużny, et al., 1909* and *Hashimoto, 1939*) and 1041 °C (*Berak, 1951*). Its instability gives a proof that the evaporation of CoP_3 directly gives CoP phase (929 – 1072 °C) without going through an intermediary CoP_2 performed by the reaction $CoP_{3\,(s)} = CoP_{(s)} + P_{2\,(g)}$, with enthalpy $\Delta H^{\circ}_{1034} = 263.67 \pm 2.64 \frac{KJ}{mol}$ and entropy, $\Delta S^{\circ}_{1034} = 187.74 \pm 2.43 \frac{J}{mol.K}$. The CoP transforms to Co_2P (1125-1328°C), $4CoP_{(s)} = 2Co_2P_{(s)} + P_{2(g)}$, $\Delta H^{\circ}_{1238} = 298.19 \pm 4.27 \frac{KJ}{mol}, \Delta S^{\circ}_{1238} = 172.97 \pm 3.39 \frac{J}{mol.K}$ (*Ishida* and *Nishizawa, 1990*). Table A.6 presentsCo-P crystal structure data.

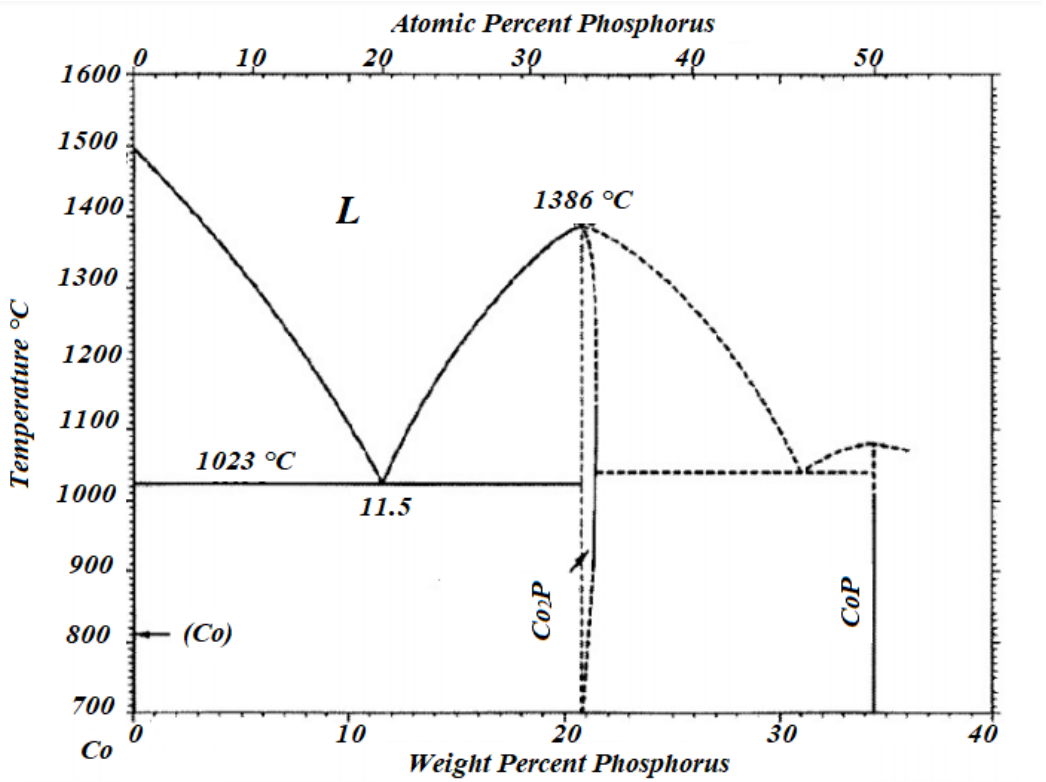

Figure A.3: *Phase diagram of the Co-P system (Ishida* and *Nishizawa 1990).*

Table A.6: *Co-P crystal structure data (Ishida* and *Nishizawa 1990).*

Phase	***Composition, at.% P***	***Pearson symbol***	***Space group***
(αCo)(a)	*~0*	*cF4*	$Fm\bar{3}m$
(εCo)(b)	*~0*	*hP2*	$P6_3/mmc$
Co_2P	*~33 à 34*	*oP12*	*Pnma*
CoP	*50*	*oP8*	*Pnma*
CoP_2(c)	*66,7*	*(d)*	….
CoP_3	*75*	*cI32*	*Im3*
P (white)	*100*	*(e)*	….
P (black)	*100*	*0C8*	*Cmca*
P (red)	*100*	*(e)*	….

(a) From 1495 to ~422°C, (b) ~422°C, (c) At 65 kbar, (d) Monoclinic and (e) Cubic.

A.2.4 Fe-Co-P (Iron-Cobalt-Phosphorus) System

Ternary phosphide materials are composed of three elements and usually involve two metals and a phosphorus isothermal section, 900 °C (1173 K) (Figure A.4). Phase relations within the system Fe–Co–P were first described by (*Berak, 1951*) and later summarized by (*Villars, et al., 1995*). Three phases are stable in the metal-rich part of the system: Co_2P, Fe_2P, and Fe_3P. Furthermore, they reported three compounds: $(Fe_{1-x}Co_x)_3P$ solid solution and $(Fe_{1-x}Co_x)_2P$ phosphides crystallized in an orthorhombic or a hexagonal structure. Researchers stated that no compounds have the composition Co_3P corresponding to Fe_3P (*Villars, et al., 1995* and *Ishida* and *Nishizawa, 1991*). The maximum solubility of cobalt in Fe_3P at 900°C is at.45% which rapidly decreases with a temperature to 10 at.% below 70°C (*Berak, 1951*).

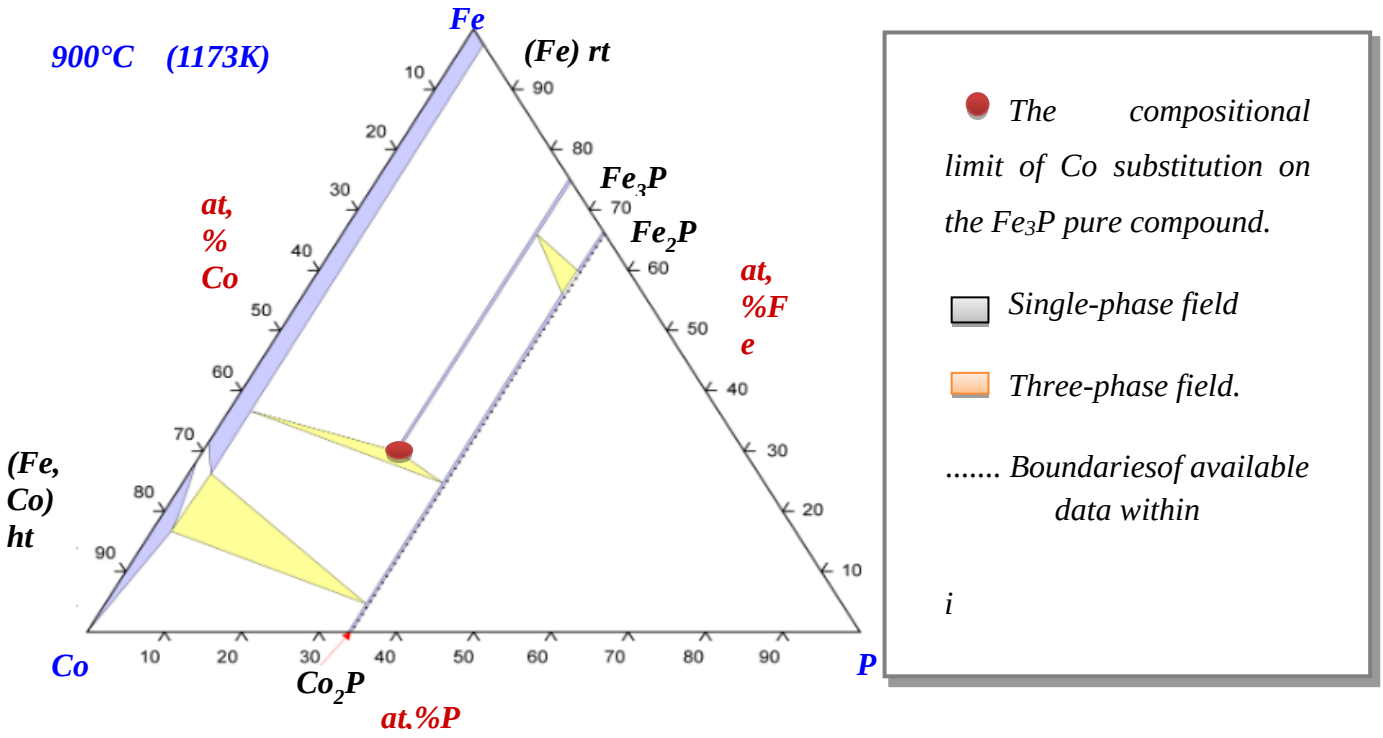

Figure A.4: *Phase diagram of the Fe-Co-P system*[1]

References

[1]https://materials-springer-com.www.sndl1.arn.dz/isp/phase-diagram/docs/c_0925042. 15/08/2021 at 14:57

A

Abdellaoui, M., Djega-Mariadassou, C., Gaffet, E. **(1997)**. Structural study of Fe-Si nanostructured materials. *Journal of Alloys and Compounds*. 259, 241-248. https://doi.org/10.1016/S0925-8388(97)00102-3

Abdullaeva, Z.,**(2017)**.Chemical properties and mechanical characteristics of nanomaterial characterization tools in nanotechnology. In book: Nano- and Biomaterials: Compounds, Properties, Characterization, and Applications, Chapter 6, 151-187. http://dx.doi.org/10.1002/9783527807024.ch6

Adeel, M., Duzagac, F., Canzonieri, V., Rizzolio, F. **(2020)**. Self-therapeutic nanomaterials for Cancer therapy: A review. *ACS Applied Nano Materials*, 3, 6. 4962–4971. https://doi.org/10.1021/acsanm.0c00762

Ahmadian Baghbaderani, H., Sharafi, S., Delshad Chermahini, M. **(2012)**. Investigation of nanostructure formation mechanism and magnetic properties in $Fe_{45}Co_{45}Ni_{10}$ system synthesized by mechanical alloying. *Powder Technology*, 230, 241–246. https://doi.org/10.1016/j.powtec.2012.07.039

Akkouche, K., Guittoum, A., Boukherroub, N., Souami, N. **(2011)**. Evolution of structure, microstructure and hyperfine properties of nanocrystalline $Fe_{50}Co_{50}$ powders prepared by mechanical alloying. *Journal of Magnetism and Magnetic Materials*, 323, 2542–2548. https://doi.org/10.1016/j.jmmm.2011.05.028

Alagarasi, A. (**2009**). Introduction to nanomaterials (Chapter). In book: *Nanomaterials* (ed. B. Viswanathan), 2–25. Mumbai: Narosa Publishing House. https://www.researchgate.net/publication/259118068

Albaaji, A.J., Castle, E.G., Reece, M.J., Hall, J.P., Evans, S.L. **(2017)**. Effect of ball-milling time on mechanical and magnetic properties of carbon nanotube reinforced FeCo alloy composites. *Material & Design.* 122:296–306. https://doi.org/10.1016/j.matdes.2017.02.091

Al-Kayiem, H.H., Lin, S.C., Lukmon, A. (**2013**). Review on nanomaterials for thermal energy storage technologies. *Nanoscience and Nanotechology –Asia*, 3:60–71. http://dx.doi.org/10.2174/22113525113119990011

Arzt, E. (**1998**). Size Effects in Materials Due to Microstructural and Dimensional Constraints: A comparative review. *Acta Materialia*, 46, 16. 5611-5626. http://dx.doi.org/10.1016/S1359-6454(98)00231-6

Attarilar, S., Yang, J., Ebrahimi, M., Wang, Q., Liu, J., Tang, Y., Yang, J. **(2020)**. The toxicity phenomenon and the related occurrence in metal and metal oxide nanoparticles: a brief review from the biomedical perspective. *Frontiers Bioengineering Biotechnology*, 8:822. https://doi.org/10.3389/fbioe.2020.00822

Azzaza, S., Alleg, S., Moumeni, H., Nemamcha, A.R., Rehspringer, J.L., Greneche, J.M., **(2006)**. Magnetic properties of nanostructured ball-milled Fe and $Fe_{50}Co_{50}$ alloy. *Journal of Physics: Condensed Matter*. 18, 7257–7272. http://dx.doi.org/10.1088/0953-8984/18/31/020

B

Bae, K.H., Chung, H.J., Park, T.G. **(2011)**. Nanomaterials for cancer therapy and imaging. *Molecules and Cells*, 31(4). 295-302. https://doi.org/10.1007/s10059-011-0051-5

Bagha, S.P., Sheibani, S., Khakbiz, M., Ebrahimi-Barough, S., Hermawan. H. **(2018)**. Novel antibacterial biodegradable Fe-Mn-Ag alloys produced by mechanical alloying. *Materials Science & Engineering C*. S0928-4931(17)32804-7. http://dx.doi.org/10.1016/j.msec.2018.03.005

Bagherzade, G. Tavakoli, M.M. Namaei, M.H. **(2017)**. Green synthesis of silver nanoparticles using aqueous extract of saffron (Crocus sativus L.) wastages and its antibacterial activity against six bacteria. *Asian Pacific Journal of Tropical Biomedicine*, 7, 227–233. https://doi.org/10.1016/j.apjtb.2016.12.014

Baheti, V.K., Abbasi, R., Militky, J. **(2012)**.Ball milling of jute fibre wastes to prepare nanocellulose. *World Journal of Engineering*, 9, 45-50. https://doi.org/10.1260/1708-5284.9.1.45

Banner, D.J. Firlar, E. Jakubonis, J. Baggia, Y. Osborn, J.K. Shahbazian-Yassar, R. Megaridis, C.M. Shokuhfar, T. **(2020)**. Correlative ex situ and liquid-cell TEM observation of bacterial cell membrane damage induced by rough surface topology. *International Journal of Nanomedcine*, 15:1929-1938. https://doi.org/10.2147/IJN.S232230

Bardhan, S., Pal, K., Roy, S., Das, S., Chakraborty, A., Karmakar, P., Basu, R., Das, S. **(2019)** Nanoparticle size-dependent antibacterial activities in natural minerals. *Journal of Nanoscience Nanotechnology*, 19. 7112–7122. https://doi.org/10.1166/jnn.2019.16658

Behvandi, A., Shokrollahi, H., Chitsazan, B., Ghaffari, M. **(2010)**. Magnetic and structural studies of mechanically alloyed nanostructured $Fe_{49}Co_{49}V_2$ powders. *Journal of Magnetism and Magnetic Materials*, 322, 3932–3937. https://doi.org/10.1016/j.jmmm.2010.08.025

Benjamin, J.S. **(1970)**. Dispersion strengthened superalloys by mechanical alloying. *Metallurgical and Materials Transactions B*, 1. 2943–2951. http://dx.doi.org/10.1007/BF03037835

Benjamin, J.S., Bomford, M.J. **(1977)**.Dispersion strengthened aluminum made by mechanical alloying. *Metallurgical and Materials Transactions A*, 8. 1301–1305. http://dx.doi.org/10.1007/BF02643845

Benjamin, J.S., Schelleng, R.D. **(1981)**.Dispersion Strengthened Aluminum-4 Pct Magnesium Alloy Made by Mechanical Alloying. *Metallurgical and Materials Transactions A*, 12. 1827–1832. http://dx.doi.org/10.1007/BF02643766

Benjamin, J.S., Volin, T.E. **(1974)**. The mechanism of mechanical alloying. *Metallurgical and Materials Transactions B*, 5. 1929–1934. http://dx.doi.org/10.1007/BF02644161

Bensalem, R., Tebib, T., Alleg, A., Sunol, J.J., Bessais, L., Greneche, J.M. **(2009)**. Magnetic properties of nanostructured $Fe_{92}P_8$ powder mixture. *Journal of Alloys and Compounds*. 471, 24–27 https://doi.org/10.1016/j.jallcom.2008.03.138

Bensebaa, N., Loudjani, N., Alleg, S., Dekhil, L., Suñol, J.J., Al Sae, M., Bououdina, M. **(2014)**. XRD analysis and magnetic properties of nanocrystalline $Ni_{20}Co_{80}$ alloys. *Journal of Magnetism and Magnetic Materials*. 349, 51–56. https://doi.org/10.1016/j.jmmm.2013.08.045

Bentayeb, F. Z., Alleg, S., Greneche, J. M. **(2007)**. Structural and microstructural study of Fe-31Cr-12Co mixture prepared by ball milling. *Journal of Alloys and Compounds*, 434-435, 477–480. https://doi.org/10.1016/j.jallcom.2006.08.111

Berak, J.B. **(1951)**. The Fe-P-Co system. *Arch. Eisenhiittenwes*, 22, 131-135. In German. (Equi Diagram; Experimental).

Betteridge, W. **(1982)**. Cobalt and its alloys. *Ellis Horwood Limited Publishers, Chichester*, 14-15

Bez, R., Bessais, L., Zehani, K., Moscovici, J., Mliki, N. **(2015)**. Structural and magnetic properties of $Fe_{100-x}Co_x$ nanoparticles synthesized by different methods. *In book: TMS 144th Annual Meeting & Exhibition*.

Bish, D.L. and Howard, S.A. **(1988)**. Quantitative phase analysis using the Rietveld method. *Journal of Applied Crystallography*, 21, 86-91. https://doi.org/10.1107/S0021889887009415

Biswas, A., Bayer, I. S., Biris, A. S., Wang, T., Dervishi, E., Faupel, F., (**2012**) Advances in top–down and bottom–up surface nanofabrication: techniques, applications & future prospects. *Advances in Colloid and Interface Science*, 170(1):2–27. http://dx.doi.org/10.1016/j.cis.2011.11.001

Bouchenafa, O. **(2020)**. Mécanosynthèse et matériaux de construction : optimisation et application pour la clinkérisation et la géopolymérisation. Doctorat thesis. Paris-Est University.

Boukeffa, S., Tebib, W., Redouani, L., Bououdina, B. **(2022)**. Novel magnetic properties evaluation of an advanced Fe_9Cu_2Zn Alloy. *Journal of Superconductivity and Novel Magnetism*, 35, 125–132. https://doi.org/10.1007/s10948-021-06007-5

Bozorth, R.M. **(1951)**. Ferromagnetism (Chapter XII). D. Van Nostrand Company. New York

Bozorth, R.M. (**1978)**. Ferromagnetism. *IEEE Magnetics Society*, 2nd edn New York, IEEE press.

Brahimi, A. **(2019)**. Elaboration et étude de matériaux magnétiques nanostructurés $(Fe_{1-X}Mn_X)_2P$. PhD thesis. Badji Mokhtar–Annaba university, Algeria.

Burda, C., Chen, X., Narayanan, R., El-Sayed, M.A. **(2005)**. Chemistry and properties of nanocrystals of different shapes. *Chemical Reviews*. 105, 1025-1102. http://dx.doi.org/10.1021/cr030063a

Buzea, C., Pacheco, I., Robbie, K. **(2007)**.Nanomaterials and nanoparticles: Sources and toxicity. *Biointerphases*, 2. 17–71. http://dx.doi.org/10.1116/1.2815690

C

Cai, J., Ruffieux, P., Jaafar, R., Bieri, M., Braun, T., Blanken burg, S., Muoth, M., Seitsonen, A., Saleh, M., Feng, X., et al. (**2010).** Atomically precise bottom-up fabrication of graphene nanoribbons. *Nature*, 466. 470–473. http://dx.doi.org/10.5167/uzh-36020

Callejas, J. F., Read, C. G., Roske, C. W., Lewis, N. S. & Schaak, R. E. **(2016)**. Synthesis, characterization, and properties of metal phosphide catalysts for the hydrogenevolution reaction. *Chemistry of Materials*, 28, 6017-6044. https://doi.org/10.1021/acs.chemmater.6b02148

Callister, W., Rethwisch, D. **(2013)**. Fundamentals of material science and engineering: An integrated approach 4th edition. Wiley. Chapter. 3.

Casalini, T., Limongelli, V., Schmutz, M., Som, C., Jordan, O., Wick, P., Borchard, G., Perale, G., Perle, G. **(2019)**. Molecular modeling for nanomaterial–biology interactions: Opportunities, challenges, and perspectives. *Frontiers Bioengineering Biotechnology*, 268. https://doi.org/10.3389/fbioe.2019.00268

Ceppatelli, M., Bini, R., Caporali, M., Peruzzini, M. Angew. (**2013**). High-pressure chemistry of red phosphorus and water under near UV irradiation. *Angewandte Chemie International Edition*, 52. 2313- 2317. https://doi.org/10.1002/anie.201208684

Chan, H., Kwok, P. **(2011**). Production methods for nanodrug particles using the bottom-up approach. *Advanced Drug Delivery Reviews*, 63. 6. 406–416. http://dx.doi.org/10.1016/j.addr.2011.03.011

Cheng, Z., Li, M., Dey, R., Chen, Y. **(2021)**. Nanomaterials for cancer therapy: current progress and perspectives. *Journal of Hematology and Oncology*. https://doi.org/10.1186/s13045-021-01096-0

Chermahini, M.D., Sharafi, S., Shokrollahi, H., Zandrahimi, M., Shafyei, A. **(2009)**. The evolution of heating rate on the microstructural and magnetic properties of milled nanostructured $Fe_{1-x}Co_x$(x = 0.2, 0.3, 0.4, 0.5 and 0.7) powder. *Journal of Alloys Compoudns*. 484, 54–58. https://doi.org/10.1016/j.jallcom.2009.05.055

Chi, L. Nanotechnology. **(2010)**. *Volume 8: Nanostructured surfaces*. 7. *Wiley, Weinheim*

Chitsazan, B., Shokrollahi, H., Behvandi, A., Mirzaee, O. **(2011)**. Characterization and magnetic coercivity of nanostructured $(Fe_{50}Co_{50})_{100-X}V_{X=0,2,4}$ powders containing a small amount of Co_3V intermetallic obtained by mechanical alloying. *Powder Technology*, 214, 105–110. https://doi.org/10.1016/j.powtec.2011.07.042

Coey, J.M.D. **(1991)**. Novel permanent magnetic materials. *Physica Script*. T39, 21–28. http://dx.doi.org/10.1088/0031-8949/1991/T39/002

Coey, J.M.D. **(2020)**. Perspective and prospects for rare earth permanent magnets. *Engineering*, 6, 119–131. http://dx.doi.org/10.1016/j.eng.2018.11.034

Cullity, B.D.; Graham C.D. **(2009).** Introduction to Magnetic Materials. 2nd edution, *Wiely Inter science*.

D

Dadkhah, M., Saboori, Z., Fino, P. **(2019)**. An overview of the recent developments in metal matrix nanocomposites reinforced by graphene. *Materials*, 12, 2823. https://doi.org/10.3390/ma12172823

Dai, L., Liu, Y., Dong, Z. **(2012)**. Size and structure evolution of yttria in ODS ferritic alloy powder during mechanical milling and subsequent annealing. *Powder Technology*, 217. 281-287. https://doi.org/10.1016/j.powtec.2011.10.039

Dapiaggi, M., Geiger, C. A., Artioli, G. **(2005)**. Letter: Microscopic strain in synthetic pyrope-grossular solid solutions determined by synchrotron X-ray powder diffraction at 5 K: The relationship to enthalpy of mixing behavior. *American Mineralogist*. 90, 506. https://doi.org/10.2138/am.2005.1716

Dakiche, M. **(2020)**. Synthèse et caractérisation de composés intermétalliques nanostructurés à base de Mn. PhD thesis. Houari Boumadiene University. Algeria.

Dash, P., Dash, T., Rout, T.K., Sahu, A.k., Biswal, S.K., Mishra, B.K. **(2016)**. Preparation of graphene oxide by dry planetary ball milling process from natural graphite. *RSC Advances*, 6, 12657-12668. https://doi.org/10.1039/C5RA26491J

De, M., Sen Gupta, S.P. **(1984)**. Lattice imperfection studies in polycrystalline materials by x-ray diffraction line-profile analysis, *Pramana – Journal of Physics,* 23, 721–744.

Dekhil, L., Alleg, S., Bououdina, M., Suñol, J.J., Grenèche, J.M. **(2015)**. Phase transformations and magnetic properties of ball-milled Fe–6P–1.7C powders. *Advanced Powder Technology* , 26. 337-678. http://dx.doi.org/10.1016/j.apt.2014.12.011

Delshad Chermahini, M., Zandrahimi, M., Shokrollahi, H., Sharafi, S. **(2009)**. The effect of milling time and composition on microstructural and magnetic properties of nanostructured Fe-Co alloys. *Journal of Alloys and Compounds*, 477, 45–50. https://doi.org/10.1016/j.jallcom.2008.10.163.

DeWitt, T.W., Skolnik, S. **(1946)**. Conversion of liquid white phosphorus to red phosphorus. I. kinetics of the reaction. *Journal of American Chemical Society*, 68. 2305-2309. https://doi.org/10.1021/ja01215a052

Donaldson, E.C., Alam, W., Begum, N. **(2013)**. Hydraulic fracturing explained. Evaluation, Implementation, and Challenges. *Elsevier*, 47-76

Dong, L., Craig, M.M., Khang, D., Chen, Ch. **(2012)**. Applications of nanomaterials in biology and medicine. *Jornal of Nanotechnology*, 2. https://doi.org/10.1155/2012/816184

Dutta, A., Pradhan, N. **(2016)**. Developments of metal phosphides as efficient OER precatalysts. *Journal of Physical Chemistry Letters*, 8. 144-152. https://doi.org/10.1021/acs.jpclett.6b02249

E

Eastman, J.A., Fitzsimmons, M.R., Thompson, L.J. **(1992)**. The thermal properties of nanocrystalline Pd from 16 to 300 K. *Philosophical Magazine Part B*, 66. 667-696. http://dx.doi.org/10.1080/13642819208207667

Eckert, M. **(2012)**. Disputed Discovery: The beginnings of X-Ray diffraction in crystals in 1912 and its repercussions. *Acta Crystallographica Section A*, 68, 30-39. https://doi.org/10.1107/s0108767311039985

El-Eskandarany, M.S. **(2015)**. Mechanical Alloying, Nanotechnology, Materials Science and Powder Metallurgy, 2 nd, William Andrew.

El-Eskandarany, M.S., Al-Hazza, A., Al-Hajji, L.A., Ali, N., Al-Duweesh, A.A.; Banyan, M., Al-Ajmi, F. **(2021)**. Mechanical milling: A superior nanotechnological tool for fabrication of nanocrystalline and nanocomposite materials. *Nanomaterials*, 11, 2484. http://dx.doi.org/10.3390/nano11102484

El-Eskandarany, S.M. **(2001)**. Mechanical alloying: For fabrication of advanced engineering materials. *New York: William Andrew Publishing*.

Elmen, G.W. **(1929)**. Magnetic material and appliance. US patent No 1,739,752.

Enayati, M. H. Aryanpour, G. R. and Ebnonnasir, A. **(2009)**. Production of nanostructured WC-Co powder by ball milling. *International Journal of Refractory Metals and Hard Materials*, 27, 159–163. http://dx.doi.org/10.1016/j.ijrmhm.2008.06.005

Eshelby, J.D., Frank, F.C., Nabarro, F.R.N. **(1951)**. The equilibrium of linear arrays of dislocations. *Philosophical Magazine Series 7*, 42, 351–364. http://dx.doi.org/10.1080/14786445108561060

F

Fabbro, A., Bosi, S., Ballerini, L., Prato, M. **(2012)**. Carbon nanotubes: Artificial nanomaterials to engineer single neurons and neuronal networks. *ACS Chemical Neuroscience*, 3, 611–618. http://dx.doi.org/10.1021/cn300048q

Fallot, M. **(1936)**. Ferromagnétisme des alliges de Fer.Thesis. Strasbourg

Fang, M., Zeisberg, W.M., Condon, C., Ogryzko, V., Danchin, A., Mechold, U. **(2009)**. Degradation of nanoRNA is performed by multiple redundant RNases in Bacillus subtilis. *Nucleic Acids Research*, 37:5114. http://dx.doi.org/10.1093/nar/gkp527

Farahmandjou, M., Honarbakhsh, S., Behrouzinia, S. (**2018**). FeCoNanorods Preparation Using New Chemical Synthesis.*Journal of Superconductivity and Novel Magnetism*. 31:4147–4152. https://doi.org/10.1007/s10948-018-4659-y

Fischer, W.A., Lorenz, K., Fabritius, H., Schlegel, D. **(1970)**. Examination of the alpha-gamma transformation in very pure binary alloys of iron with molybdenum, vanadium, tungsten, niobium, tantalum, zirconium, and cobalt. *Arch. Eisenhiittenwes*. 41, 489

Foner, S. **(1956)**. Vibrating sample magnetometer. *Review of Scientific Instr*uments, 27, 548. https://doi.org/10.1063/1.1715636

Foner, *S.* **(1959)**.Versatile and Sensitive Vibrating-Sample Magnetometer *THE REVIEW OF SCIENTIFIC INSTRUMENTS* . 30, 7. https://doi.org/10.1063%2F1.1716679

Franco, V., Blázquez, J., Ingale, B., Conde, A., **(2012)**. The magnetocaloric effect and magnetic refrigeration near room temperature: materials and models. *Annual Review of Materials Research*, 42. 305-342. https://doi.org/10.1146/annurev-matsci-062910-100356

Fukunaga, T., Nakamura, K., Suzuki, K., Mizutani, U. **(1990)**. Amorphization of immiscible CuTa system by mechanical alloying and its structure observation. *Journal of Non-Crystalline Solids*, 118, 700–703. http://dx.doi.org/10.1016/0022-3093(90)90625-V

G

Galloway, T.S., Cole, M., Lewis, C. **(2017).** Interactions of microplastic debris throughout the Marine ecosystem. *Nature Ecology & Evolution 1, 5*. 116. http://dx.doi.org/10.1038/s41559-017-0116

Gheidari, D., Mehrdad, M., Maleki , S., H, Samanesadat. **(2020)**. Synthesis and potent antimicrobial activity of $CoFe_2O_4$ nanoparticles under visible light. *Heliyon*, 6, 10, e05058. https://doi.org/10.1016/j.heliyon.2020.e05058

Gilman, P.S., Benjamin, J.S. **(1983)**. Mechanical alloying. *Annual Review of Material Science.* 13, 279–300. http://dx.doi.org/10.1146/annurev.ms.13.080183.001431

Gleiter, H. **(1989)**. Nanocrystalline materials. *Progress in Materials Science*, 33, 223-315. https://doi.org/10.1016/0079-6425(89)90001-7

Gleiter, H. **(1995)**. Nanostructured materials: State of the art and perspectives. *Nanostructured Materials*. 6, 3-14. https://doi.org/10.1016/0965-9773(95)00025-9

Gleiter, H. (**2000).** Nanostructured materials: Basic concepts and microstructure. *Acta Materialia*, 48, 1–29. http://dx.doi.org/10.1016/S1359-6454(99)00285-2 Godoy-Gallardo, M., Eckhard, U., Delgado, L.M., de Roo Puente, Y.J.D., Hoyos-Nogués, M., Gil, F.J., Perez, R. A. **(2021)**. Antibacterial approaches in tissue engineering using metal ions and nanoparticles: From mechanisms to applications. *Bioactive Materials*.6. 4470-4490. https://doi.org/10.1016/j.bioactmat.2021.04.033

Goldman, A., **(2006)**. Modern ferrite technology. *Springer Science & Business Media.*

Gómez-Romero, P., Sanchez, C. **(2005)**. Hybrid Materials, Functional Applications. An Introduction. In book: *Functional Hybrid Materials*. *Weinheim, Germany: Wiley-VCH*, 434. http://dx.doi.org/10.1002/3527602372.ch1

Gravereau, P. **(2012).** Introduction à la pratique de la diffraction des rayons X par les poudres. ICMCB-CNRS, Université Bordeaux 1.

Gubicza, J., Kassem, M., Ribarik, G., Ungar, T. **(2004)**. The microstructure of mechanically alloyed Al–Mg determined by X-ray diffraction peak profile analysis. *Materials Science and Engineering A*, 372, 115–122. http://dx.doi.org/10.1016%2Fj.msea.2003.12.016

H

Hajipour, M.J., Fromm, K.M, Ashkarran, A.A., Jimenez de Aberasturi, D., Ruiz de Larramendi, I., Rojo, T., Serpooshan, V., Parak, W.J., and Mahmoudi, M. **(2012).** Antibacterial properties of nanoparticles. *Trends in Biotechnol*ogy, 30. 499–511. https://doi.org/10.1016/j.tibtech.2012.06.004

Hall, E.O. **(1951)**. The deformation and ageing of mild steel: III Discussion of results. *Proceedings of the Physical Society. Section B*, 64. 747–753. http://dx.doi.org/10.1088/0370-1301/64/9/303

Hall, W.H. **(1949)**. X-ray line broadening in metals. *Physical Society Section A,* 62, 741–743. https://doi.org/10.1088/0370-1298/62/11/110

Hamzaoui, R., Elkedim, O., Gaffet, E., Greneche, J.M. **(2006)**. Structure, magnetic and mössbauer studies of mechanically alloyed Fe–20 wt.% Ni powders. *Journal of Alloys and Compounds*. 417, 32–38. https://doi.org/10.1016/j.jallcom.2005.09.064

Han, Y., Ding, J., Kong, F.L., Inoue, A., Zhu, S.L., Wang, Z., Shalaan, E., Al-Marzouki, F. **(2017)**. FeCo-based soft magnetic alloys with high B_s approaching 1.75 T and good bending ductility. *Journal of Alloys and Compounds*, 691. 364-368. https://doi.org/10.1016/j.jallcom.2016.08.250

Hashimoto, U. **(1939)**. The effect of various elements on the α↔β allotropic transformation point of cobalt. *Journal of Japan Institute of Metals and Materials*, 2, 67-77. In Japanese. (Equi Diagram, Mag- netism; Experimental.

Herzer, G. **(1990)**. Grain size dependence of coercivity and permeability in nanocrystalline ferromagnets. *IEEE Transactions on Magnetics*. 26, 13977. https://doi.org/10.1109/20.104389

Herzer, G. **(1997)**. Nanocrystalline soft magnetic alloys, "Handbook of Magnetic Materials", Edited by K. Buschow, *Elsevier Science*. 10, 415-462,

Herzer, G. **(2005)**. The random anisotropy model. Properties and applications of nanocrystalline alloys from amorphous precursors. NATO Science Series, *Springer, Dordrecht*, 184, 15–34. https://doi.org/10.1007/1-4020-2965-9_2

Hill, R.J. and Howard, C.J. **(1987)**. Quantitative phase analysis from neutron powder diffraction data using the Rietveld method. *Journal of Applied Crystallography*, 20, 467-474. https://doi.org/10.1107/S0021889887086199

Hofmann, H.P., Lohberg, K., Reif, W. **(1970)**. Solubility of P in Fe and Fe-C alloys at temperatures below 1000 C. *Arch Eisenhuttenwesen*, 41(10), 975-982.

Holleman, A.F., Wiberg, E. (Walter de Gruyter). **(1995).** Lehrbuch der anorganischen Chemie. https://doi.org/10.1515/9783110838176

Horst, M.F, Coral, D.F, Fernandez van Raap MB, Alvarez M, Lassalle V. **(2017)**. Hybrid nanomaterials based on gum Arabic and magnetite for hyperthermia treatments. *Material Science Engineering*, 74. 443–450. https://doi.org/10.1016/j.msec.2016.12.035

Hosseini-Zori, M. **(2018)**. Biology Co-doped TiO_2 nanostructures as a strong antibacterial agent and self- cleaning cover: synthesis, characterization and investigation of photocatalytic activity under UV irradiation. *Journal of photochemistry and Photobiology B: Biol*ogy, 178, 512–520. https://doi.org/10.1016/j.jphotobiol.2017.12.008

Huba, Z.J., Carroll, K.J., Carpenter, E.E. **(2011)**. Synthesis of high magnetization FeCo alloys prepared by a modified polyol process. *Journal of Applied Physics*. 109, 07B514. https://doi.org/10.1063/1.3544430

Hull, D. Bacon, D.J. **(1950)**. Introduction to dislocations. Fifth edition. *Butterworth-Heinemann, Elsevier*.

I

Iqbal, P., Preece, J.A., Mendes, P.M. **(2012)**. Nanotechnology: The "top-down" and "bottom-up" approaches. In: Gale PA, Steed JW, editors. *Supramolecular Chemistry.John Wiley & Sons, Ltd*. http://dx.doi.org/10.1002/9780470661345.smc195

Ishida, K., Nishizawa, *T*. (**1974**). Effect of alloying elements on stability of epsilon iron. *Transactions of the Japan Institute of Met*als. 15, 225. https://doi.org/10.2320/matertrans1960.15.225

Ishida, K.; Nishizawa, T. **(1990)**. The Co-P (Cobalt-Phosphorus) system. *Bulletin of Alloy Phase Diagrams*, 6,555-559. https://doi.org/10.1007/BF02841716

J

Jeitschko, W., Braun, D.J. **(1978)**. Synthesis and crystal structure of the iron polyphosphide FeP_4. *Acta Crystallographica*, 34, 3196-3201. https://doi.org/10.1107/S056774087801047X

Jiang, P., Liu, Q., Ge, Ch., Cui, W., Pu, Z., Asiribc, A.M., Sun, X. **(2014).** CoP nanostructures with different morphologies: synthesis, characterization and a study of their electrocatalytic performance toward the hydrogen evolution reaction. *Journal of Materials Chemistry. A*, 2, 14634-14640. https://doi.org/10.1039/C4TA03261F

Jiles, D. (**2016**). Introduction to magnetism and magnetic materials. *3ed ed. CRC Press.* https://doi.org/10.1201/b18948

K

Karak, N. **(2019)**. Fundamentals of nanomaterials and polymer nanocomposites. Chapter 1. *In book: Nanomaterials and Polymer Nanocomposites.* Tezpur University, Tezpur, India. http://dx.doi.org/10.1016/B978-0-12-814615-6.00001-1

Karthik, S., Suriyaprabha, R., Balu, K.Sh., Manivasakan, P., Rajendran. V. **(2016)**. Influence of ball milling on the particle size and antimicrobial properties of Tridax procumbens leaf nanoparticles. *IET Nanobiotechnology*. 11, 1751-8741. http://dx.doi.org/10.1049/iet-nbt.2016.0028

Kemsheadl, J. T., and Ugelstad, J. **(1985)**. Magnetic separation techniques: their application to medicine. *Molecular and Cellular Biochemistry*. 67, 11–18. https://doi.org/10.1007/BF00220980

Khan, F.A. **(2020)**. Applications of Nanomaterials in Human Health. *Springer Nature Singapore Pte Ltd*, 125-126. https://doi.org/10.1007/978-981-15-4802-4

Kim, D, Kim J., Lee, J., Kang, M.K., Kim, S., Park, S.H., Kim, J., Choa, Y-H., Lim, J-H. **(2019)**. Enhanced magnetic properties of FeCo alloys by two-step electroless plating. *Journal of the Electrochemical Society*, 166 (4) D131-D136. https://doi.org/10.1149/2.1251902jes

Kim, K., Churchill, DG. **(2011)**. Phosphorus. *Korea Advanced Institute of Science and Technology (KAIST), Daejeon, Republic of Korea.* DOI: 10.1002/9781119951438. eibc0418. Available from: https://onlinelibrary.wiley.com/doi/abs/10.1002/9781119951438.eibc0418

Koch, C.C., Cavin, O.B., McKamey, C.G., Scarbourgh, J.O. **(1984)**. Preparation of "amorphous" $Ni_{60}Nb_{40}$ by mechanical alloying. *Applied Physics Letters*, 43. 1017–1019. http://dx.doi.org/10.1063/1.94213

Koper, O., Winecki, S. **(2001)**. Specific heats and melting points of nanocrystalline materials. *Nanoscale materials in chemistry*. 263-277. http://dx.doi.org/10.1002/0471220620.ch8

Kordecki, A., Węgliński, B., Kaczmar, J. **(1982)**. Properties and applications of soft magnetic powder composites. *Powder Metallurgy*, 25:4, 201-208. https://doi.org/10.1179/pom.1982.25.4.201

Kronmüller, H., **(1981)**. Theory of the coercive field in amorphous ferromagnetic alloys. *Journal of Magnetism and Magnetic Materials*, 24, 159-167. https://doi.org/10.1016/0304-8853(81)90010-X

Kumar, M., Xiong, X., Wan , Zh., Sun, Y., Tsang , D.C.W., Gupta, J., Gao ,B., Cao , X., Tang, J., Sik Ok, Y. **(2020)**. Ball milling as a mechanochemical technology for fabrication of novel biochar nanomaterials. *Bioresource Technology*, 312. 123613. https://doi.org/10.1016/j.biortech.2020.123613

Kumar, S., Dubey, A. K., Pandey, A. K. (**2013**). Computer-aided genetic algorithm based multi-objective optimization of laser trepan drilling. *Intnational Journal of Precision Engineering and Manufacturing*, 14. 1119–1125. http://dx.doi.org/10.1007/s12541-013-0152-5

Kuo, K.K., Risha, G.A., Evans, B.J., Boyer, E. **(2003)**. Potential usage of energetic nano-sized powders for combustion and rocket propulsion. *Materials Research Society symposia Proceedings,Materials Research Society* 800, AA1.1.1- AA1.1.12. http://dx.doi.org/10.1557/PROC-800-AA1.1

L

Laala-Bouali, H., Bentayeb, F.-Z., Louidi, S., et al. **(2013)**. X-ray line profile analysis of the ball-milled Fe–30Co alloy. *Advanced Powder Technology*. 24, 168–174. https://doi.org/10.1016/j.apt.2012.04.007

Lagerlof, P.P. **(2018)**. Crystal dislocations: Their impact on physical properties of crystals. *Crystals, 8, 413*. Case Western Reserve University USA. http://dx.doi.org/10.3390/cryst8110413

Larson, M.G., Bengzon, F. **(2013)**. Finite element method: Theory, implementation, and applications. *Springer-verlag Berlin Heidelberg*. https://doi.org/10.1007/978-3-642-33287-6

Le Mercier T. **(2019)**. Matériaux nanostructurés industriels : Impact de la maîtrise de la taille sur les propriétés. *Book Chimie, nanomatériaux, nanotechnologie*. France. https://doi.org/10.1051/978-2-7598-2399-4.c005

Li, J.C.M. **(1963)**. Petch relation and grain boundary sources. *Transactions of the Metallurgical Societyof AIME*, 227, 239–247

Li-cong, P., Ying, Zh., Shu-lan, Z., Min, H., Jian-wang, C., Shou-guo, W., Hong-xiang, W., Jian-qi, L., Tong-yun, Zh., Bao-gen, Sh. (**2018**). Lorentz transmission electron microscopy studies on topological magnetic domains. *Chinese Physics B*, 27. 066802. http://dx.doi.org/10.1088/1674-1056/27/6/066802

Ling, H., Li, Q., Li, H., Zhang, J., Dong, Y., Chang, C., & Seonghoon, Y. **(2014)**. Preparation and characterization of quaternary magnetic $Fe_{80-x}Co_xP_{14}B_6$ bulk metallic glasses. *Journal of Applied Physics*, *115*(20), 204901. https://doi.org/10.1063/1.4878917

Liu, Y., Zhu, Sh., Gu, Zh., Chen, Ch., Zhao, Y. **(2022)**. Toxicity of manufactured nanomaterials. *Particuology*, 69, 31-48. https://doi.org/10.1016/j.partic.2021.11.007

Loffler, J., Weissmuller, J. (**1995**). Grain-boundary atomic structure in nanocrystalline palladium from x-ray atomic distribution functions. *Physical ReviewB*, 52. 7076-7093. https://doi.org/10.1103/PhysRevB.52.7076

Loginov P.A., Levashov E.A., Kurbatkina V.V., Zaitsev, A.A., Sidorenk, D.A. **(2015)**. Evolution of the microstructure of Cu–Fe–Co–Ni powder mixtures upon mechanical alloying. *Powder Technolgy*. 276, (Supplement C), 166–174. http://dx.doi.org/10.1016/j.powtec.2015.02.020

Loudjani, N., Benchiheub, M., Bououdina, M. **(2016)**. Structural, thermal and magnetic properties of nanocrystalline $Co_{80}Ni_{20}$ alloy prepared by mechanical alloying. *Journal of Superconductivity and Novel Magnetism.* 29, 2717–2726. http://dx.doi.org/10.1007%2Fs10948-016-3541-z

Loudjani, N., Bensebaa, N., Dekhil, L., Alleg, S., Sunol, J.J. **(2011)**. Structural and magnetic properties of $Co_{50}Ni_{50}$ powder mixtures. *Journal of Magnetism and Magnetic Materials*. 323, 3063–3070. https://doi.org/10.1016/j.jmmm.2011.06.059

Louidi, S., Bentayeb, F-Z., Tebib, W., Sunol, J.J., Escodac, L. Mercier, A.M. **(2012)**. Stacking faults and phase transformations study in ball milled $Co_{100-x}Cr_x$ (x = 0, 20, 50) alloys. *Materials Chemistry and Physics*. 132, 761–765. http://dx.doi.org/10.1016/j.matchemphys.2011.12.008

Lü, L., Lai, M.O. **(1998)**. Mechanical alloying, 1st ed.; Shingu, P.H., Ed.; *Springer: Boston, MA, USA*, 1. 1–9. https://doi.org/10.1007/978-1-4615-5509-4

Lu, L., Zhang, Y.F. **(1999)**. Influence of process control agent on interdiffusion between Al and Mg during mechanical alloying. *Journal of Alloys and Compounds*. 290. 279-283. https://doi.org/10.1016/S0925-8388(99)00221-2

Lucas, L., Perez, C.; Aroca, P., Sánchez, E., López, M., Sánchez, C. **(2005)**. Magnetic properties of CoP alloys electrodeposited at room temperature. *Journal of Magnetism and Magnetic Materials*, 290–291. 1513–1516. https://doi.org/10.1016/j.jmmm.2004.11.563

Lungu, M., Neculae, A., Bunoiu, M., Biris, C. **(2015)**. Natural sources of nanoparticles " Nanoparticles promises and risks": Characterization, manipulation, and potential hazards to humanity and the environment. Chapter 2. *Springer Cham Heidelberg New York Dordrecht London*.9-19. http://dx.doi.org/10.1007/978-3-319-11728-7

Lutterotti, L., Matthies, S., Wenk, H.R. **(1999)**. MAUD: A friendly java program for material analysis using diffraction. IUCr: Newsletter of the CPD 21:14–15.

M

Makhluf, S. Dror, R. Nitzan, Y. Abramovich, Y. Jelinek, R. Gedanken, A. **(2005**). Microwave-assisted synthesis of nanocrystalline MgO and its use as a bacteriocide. *Advanced Functional Materials*, 15(10):1708–1715. http://doi.org/10.1002/adfm.200500029

Manna, S.K., Prabhu, D.B., Gopalan, R., Srinivas, V. **(2014)**. AC Magnetic properties and core loss behavior of Fe – P soft magnetic sheets. *IEEE Transactions of Magnetics*. 50, 4–7. https://doi.org/10.1109/TMAG.2014.2331084

Massalski, T.B, Okamoto, H. **(1990)**. Binary alloy phase diagrams. *ASM International Materials Park, Ohio*, 2, 1186-1187

Matthew, T.C. Christine, J-W. **(2005)**. Bacterial cell shape. *Nature Reviews Microbiol*ogy, 3(8):601-10. http://doi.org/10.1038/nrmicro120

Mazeeva, A.K., Staritsyn, M.V., Bobyr, V.V., Manninen, S.A., Kuznetsov, P.A., Klimov, V.N. **(2020)**. Magnetic properties of Fe–Ni permalloy produced by selective laser melting. *Journal of Alloys and Compounds*. 814, 152315. https://doi.org/10.1016/j.jallcom.2019.152315

McHenry, M.E., Laughlin, D.E. **(2014)**. Magnetic properties of metals and alloys. Physical metallurgy, fifth ed., *Elsevier B.V.*, 1881–2008. http://dx.doi.org/10.1016/B978-0-444-53770-6.00019-8

McHenry, M.E., Willard, M.A., Laughlin, D.E. **(1999)**. Amorphous and nanocrystalline materials for applications as soft magnets. *Progress in Materials Science*. 44, 291-433. https://doi.org/10.1016/S0079-6425(99)00002-X

Mebrek, S., Haddad, A., Haine, N. **(2021)**. Characterization of nano crystalline alloy $Fe_{65}Co_{35}$. *Digest Journal of Nanomaterials and Biostructures*. 16, 331 - 335

Meyers, M.A., Vöhringer, O., Lubarda, A.A. **(2001)**. The onset of twinning in metals: A constitutive description. *Acta Materialia*. 49, 4025-4039. https://doi.org/10.1016/S1359-6454(01)00300-7

Michelson, A.A., Morley E.W. **(1887).** On the relative motion of the earth and the luminiferous ether. *TheAmerican Journal of the Medical Sciences*, 34, 333–345. https://doi.org/10.2475/ajs.s3-34.203.333

Mijatovic, D., Eijkel, J., Den Van, Berg A. **(2005)**. Technologies for nanofluidic systems: top-down versus bottom-up—a review. *Lab on a Chip*, 5. 492–500. http://dx.doi.org/10.1039/b416951d

Modin, E.B., Voitenko, O.V., Pustovalov, E.V., Plotnikov, V.S., Grudin, B.N., Polischuk, S.V., Grabchikov. S.S. **(2014)**. HAADF–STEM Investigation of the structures of electrolytically deposited CoP and CoNiP alloys. *Bulletin of the Russian Academy of Sciences. Physics*, 78. 886–889. http://dx.doi.org/10.3103/S1062873814090172

Moskowitz, B.M., **(1991)**. Hitchhiker's guide to magnetism. *In Environmental Magnetism Workshop (IRM)*, 279. 1. 48.

Moumeni, H., Nemamcha, A., Alleg, S., Greneche, J. M. **(2013**). Hyperfine interactions and structural features of Fe-44Co6Mo (wt.%) nanostructured powders. *Materials Chemistry and Physics*, 138, 209–214. http://dx.doi.org/10.1016/j.matchemphys.2012.11.048

Moumeni, H., Alleg, S., Greneche, J. M. **(2005)**. Structural properties of $Fe_{50}Co_{50}$ nanostructured powder prepared by mechanical alloying. *Journal of Alloys and Compounds*, 386, 12–19. https://doi.org/10.1016/j.jallcom.2004.05.017

Mukherjee, A. K. **(1993)**. Superplasticity in metals, ceramics and intermetallics. H. Mughrabi (ed.), *Verlagsges; Weinheim*, Germany. 6. 407-460.

Murty, B.S., Shankar, P., Raj, B., Rath, B.B., Murday, J. **(2013)**. *Textbook of and Nanoscience Nanotechnology. USA. Springer*

N

Nasibi, S., Shokrollahi, H. Karimi, L. Janghorban, K. **(2012)**. Investigation of structural, microstructural and magnetic properties of mechanically alloyed amorphous/nanocrystalline $Fe_{32.5}Co_{32.5}Nb_{35}$ powders. *Powder Technology*, 228, 404–409. https://doi.org/10.1016/j.powtec.2012.05.059

Nath, D., Banerjee, P. **(2013)**. Green nanotechnology - A new hope for medical biology. *Environmental Toxicology and Pharmacology*, 36. 997–1014. https://doi.org/10.1016/j.etap.2013.09.002

Nel, A., Xia, T., Mädler, L., Li, N. **(2006)**. Toxic potential of materials at the nanolevel. *Science*, 311. 622–627. http://dx.doi.org/10.1126/science.1114397

Nilges, T., Schmidt, P., Weihrich, R. **(2018)**. Phosphorus: The allotropes, stability, synthesis, and selected applications. *Encyclopedia of Inorganic and Bioinorganic Chemistry*. https://doi.org/10.1002/9781119951438.eibc2643

O

Oberdörster, G., Maynard, A., Donaldson, K., Castranova, V., Fitzpatrick, J., Ausman, K., Carter, J., Karn, B., Kreyling, W., Lai, D., Olin, S., Monteiro-Riviere, N., Warheit, D. **(2005)**. Principales for characterizing the potential human health effects from exposure to nanomaterials: elements of a screening strategy. Review. Particle and Toxicology, 2:8. Doi: 10.1186/1743-8977-2-8.

Okamoto, H. **(2008)**. Co-Fe (Cobalt-Iron). *Journal of Phase Equilibria and Diffusion*. 29:383–384. https://doi.org/10.1007/s11669-008-9345-5

Okamoto, H. (**2010).** Ni-P (Nickel-Phosphorus). *Journal of Phase Equilibria Diffusions*, 31. 200−201. https://doi.org/10.1007/s11669-010-9664-1

Oyama, S.T. **(2003)**. Novel catalysts for advanced hydroprocessing: transition metal phosphides. *Journal of Catalysis*, 216. 343-352. https://doi.org/10.1016/S0021-9517(02)00069-6

Oyedele, J.A.**(1979)**. McMaster Univ. *Dissertation AbstractsInternational*. 39, 9.

P

Palmer, L.D. Skaar, E.P. **(2016)**. Transition metals and virulence in bacteria. *Annual Review of Genetics*, 50, 67–91. http://doi.org/10.1146/annurev-genet-120215-035146.

Park, I., Li, Z., Pisano, A., Williams, R., **(2009)**.Top-down fabricated silicon nanowire sensors for real-time chemical detection. *Nanotechnology*. 21. 015501. 9. http://dx.doi.org/10.1088/0957-4484/21/1/015501

Permiakov, V., Dupré, L., Pulnikov, A., Melkebeek, J. **(2004)**. Loss separation and parameters for hysteresis modelling under compressive and tensile stresses. *Journal Magnetism and Magnetic Materials*. 272–276, e553–e554. https://doi.org/10.1016/j.jmmm.2003.11.381

Petch, N.J., **(1953)**. The cleavage strength of polycrystals. *Journal of Iron Steel Institute*, 174. 25–28.

Pilar, M., Suñol, J.J., Escoda, L., Saurina, J., Arcondo, B. **(2008)**. Synthesis and characterization of nanocrystalline $Fe_{60}X_{20}B_{10}P_{10}$ (X = Co, Ni) alloys. *Journal of Non-Crystalline Solids*, 354. 5129–5131. https://doi.org/10.1016/j.jnoncrysol.2008.06.107

Pokropivny, V.V., Skorokhod, V.V. (**2007)**. Classification of nanostructures by dimensionality and concept of surface forms engineering in nanomaterial science. *Materials Science and Engineering C*, 27. 990–993. http://dx.doi.org/10.1016/j.msec.2006.09.023

Pokropivny, V.V., Skorokhod, V.V. **(2008)**. New dimensionality classifications of nanostructures. *Physica E* 40, 40. 2521–2525. http://dx.doi.org/10.1016/j.physe.2007.11.023

Poplavko, Y.M. (**2019**). Mechanical properties of solids. Chapter 2. *Electronic Materials*. *Elsevier*, Amsterdam, 71-93. https://doi.org/10.1016/B978-0-12-815780-0.00002-5

Popova, A. N., Zaharov, Y. A., Pugachev, V. M. **(2012)**. Chemical synthesis, structure and magnetic properties of nanocrystalline Fe-Co alloys. *Materials Letters*, 74, 173–175. https://doi.org/10.1016/j.matlet.2012.01.090

Poudya, N., Rong, Ch., Zhanga, Y., Wang, D., Kramer, M.J., Hebert, R.J., Liu, J.P. **(2012)**. Self-nanoscaling in FeCo alloys prepared via severe plastic deformation. *Journal of Alloys and Compounds*, 521. 55-59. https://doi.org/10.1016/j.jallcom.2012.01.026

Prins, R., Bussell, M.E. **(2012)**. Metal Phosphides: Preparation, Characterization and Catalytic Reactivity. *Catalysis Letters*, 142. 1413–1436. https://doi.org/10.1007/s10562-012-0929-7

Q

Quigley, R.E. Jr., **(1993)**. More Electric Aircraft, Conference Record, *IEEE Applied Power Electronics Conference*, 906-911.

R

Rietveld, H.M. **(1969)**. A profile refinement method for nuclear and magnetic structures. *Journal of Applied Crystallography*, 2, 65-71. https://doi.org/10.1107/S0021889869006558

Roduner, E. **(2006)**. Size matters: Why nanomaterials are different. *The Royal Society of Chemistry*, 35. 583-592. http://dx.doi.org/10.1039/b502142c

Roth, W., DeWitt T., Smith, A. J. **(1947)**. Polymorphism of Red Phosphorus. *Journal of the American Chemical Society*, 69. 2881-2885. https://doi.org/10.1021/ja01203a072

S

Saleh, T.A., Gupta, V.K. **(2016)**. Nanomaterial and polymer membranes: Synthesis, characterization, and applications. *Elsevier*.

Sánchez-De Jesús, F., Bolarín-Miró, A. M., Cortés Escobedo, C. A., Torres-Villaseñor, G., Vera-Serna. P. **(2016)**. Structural Analysis and Magnetic Properties of FeCo Alloys Obtained by Mechanical Alloying. *Journal of Metallurgy*. http://dx.doi.org/10.1155/2016/8347063

Scheer, M., Balazs, G., Seitz, A. **(2010)**. P_4 Activation by main group elements and compounds. *Chemical reviews*, 110. 4236-4256. https://doi.org/10.1021/cr100010e

Scherrer, P. **(1912)**. Bestimmung der inneren Struktur und der Größe von Kolloidteilchen mittels Röntgenstrahlen. In: Kolloidchemie Ein Lehrbuch. Chemische technologie in Einzeldarstellungen. *Springer, Berlin, Heidelberg*. 387-409. https://doi.org/10.1007/978-3-662-33915-2_7

Sebt, A., Akhavan, M.. Switching field distribution of magnetic fine particles. **(2001).** *Journal of Magnetism and Magnetic Materials*, 237, 111–118. https://doi.org/10.1016/S0304-8853(01)00440-1

SenGupta, S.P, Chatterjee, P. **(2002)**. Powder diffraction: Proceedings of the II international powder diffraction: Proceedings of the II international school on powder diffraction. *Allied publishers LTD*, India. 63-76.

Sergiu Ruta, S., Hovorka, O., Huang, P-W., Wang, K., Ju, G., Chantrell, R.**(2017).** First order reversal curves and intrinsic parameter determination for magnetic materials; limitations of hysteron-based approaches in correlated systems.. *Scientific Reports*, 7:45218. DOI: 10.1038/srep45218

Shankar B. Dalavi, M. Manivel Rajab, Rabi N. Panda. (**2015**). FTIR, magnetic and Mössbauer investigations of nano-crystalline Fe_xCo_{1-x} ($0.4 \leq x \leq 0.8$) alloys synthesized via a superhydride reduction route. *J. The Royal Society of Chemistry*. https://doi.org/10.1039/C5NJ01727K

Sharma, R.K., Sharma, Sh., Yadav, M., Dutta, S. **(2019)**. An Introduction to silica-based organic-inorganic hybrid nanostructured catalytic systems (Chapter 01). *In book: Silica-Based Organic–Inorganic Hybrid Nanomaterials*. University of Delhi. India. http://dx.doi.org/10.1142/9781786347473_0001

Sheldon, J.R. Laakso, H.A. Heinrichs, D.E. **(2016)**. Iron acquisition strategies of bacterial pathogens. *Microbiology Spectrum*, 4: VMBF-0010-2015. http://doi.org/10.1128/microbiolspec.VMBF-0010-2015.

Shokrollahi, H. **(2009)**. The Magnetic and structural properties of the most important alloys of iron produced by mechanical alloying. *Materials & Design*. 30, 3374–3387. http://dx.doi.org/10.1016/j.matdes.2009.03.035

Shokrollahi, H., Janghorban, K. **(2006)**. The effect of compaction parameters and particle size on magnetic properties of iron-based alloys used in soft magnetic composites. *Materials Science and Engineering B*. 134, 41–43. https://doi.org/10.1016/j.mseb.2006.07.015

Shukla, A. K. **(2017)**. EMR/ESR/EPR Spectroscopy for characterization of nanomaterials. *Advanced Structured Materials*. *62*. Allahabad. India

Shull, R.D. **(2007)**. Nanocrystalline and nanocomposite magnetic materials and their applications . *Journal of Iron and Steel Research, International*. 14(4), 69-74. http://dx.doi.org/10.1016/S1006-706X(07)60061-2

Silva, G. **(2004)**. Introduction to nanotechnology and its applications to medicine. *Surgical Neurology*, 61. 216–220. http://dx.doi.org/10.1016/j.surneu.2003.09.036

Singh, V., Yadav, P., Mishra, V. **(2020)**. Recent advances on classification, properties, synthesis, and characterization of nanomaterials (Chapter). *In book: Green Synthesis of Nanomaterials for Bioenergy Applications.* School of Biochemical Engineering, IIT (BHU), Varanasi, Uttar Pradesh, India. http://dx.doi.org/10.1002/9781119576785.ch3

Skomski, R. Sellmyer, D. J. (2008). Intrinsic and Extrinsic Properties of Advanced Magnetic Materials. *Chemical Informatics*. 37(47), 1-57. http://dx.doi.org/10.1007/1-4020-7984-2_1.

Sládková, K., Houška, J., Havel, J. **(2009)**. Laser desorption ionization of red phosphorus clusters and their use for mass calibration in time-of-flight mass spectrometry. *Rapid Communications in Mass Spectrometry*, 23. 3114-3118. https://doi.org/10.1002/rcm.4230

Slavin, Y.N. Jason Asnis, J. Urs O. Häfeli, O.U. Bach, H. **(2017)**. Metal nanoparticles: understanding the mechanisms behind antibacterial activity. *Journal of Nanobiotechnology*, 15, 1–20. http://doi.org/10.1186/s12951-017-0308-z.

Sort, J., Nogués, J., Suriñach, S., Muñoz, J. S., Baró. M. D. **(2004)**. Correlation between stacking fault formation, allotropic phase transformations and magnetic properties of ball-milled cobalt. *Materials Science and Engineering A*, 375-377, 869–873. https://doi.org/10.1016/j.msea.2003.10.186

Sort, J., Noguès, J., Suriňach, S., Munoz, J.S., Barò, M.D. **(2004)**. Correlation between Stacking Fault formation, allotropic phase transformations and magnetic properties of ball-milled cobalt. *Material Science and Engineering A*, 375-377, 869-873. https://doi.org/10.1016/j.msea.2003.10.186

Souilah, S., Alleg, S., Djebbari, C., Bensalema, R., Sunol, J.J. **(2012)**. Magnetic and microstructural properties of the mechanically alloyed $Fe_{57}Co_{21}Nb_7B_{15}$ powder mixture. *Materials Chemistry and Physics*. 132, 766–772. https://doi.org/10.1016/j.matchemphys.2011.12.010

Sourmail, T. **(2005)**. Near equiatomic FeCo alloys: Constitution, mechanical and magnetic properties. *Progress in Materials Science*. 50, 816-880. https://doi.org/10.1016/j.pmatsci.2005.04.001

Sourmail, T. **(2005)**. Near equiatomic FeCo alloys: Constitution, mechanical and magnetic properties. *Progress in Materials Science*, 50, 816–880. https://doi.org/10.1016/j.pmatsci.2005.04.001

Stefanita, C. G., **(2012)**. Magnetism: Basics and applications. *Springer Science & Business Media*. http://dx.doi.org/10.1007/978-3-642-22977-0

Stolyar, S. V., Chekanova , LA., Yaroslavtsev, RN., Ladygina, V. Tirranen, LS. **(2019)**. Effect of nanoparticles in growth of test – bacteria. *Journal of Physics: Conference Series*. 399 022029. https://doi.org/10.1088/1742-6596/1399/2/022029

Stoner, E.C., Wohlfarth, E.P. **(1948)**. A mechanism of magnetic hysteresis in heterogeneous alloys. *Royal Society*,240, 826. https://doi.org/10.1098/rsta.1948.0007

Sundar, R.S. and Deevi, S.C. **(2005)**. Soft magnetic FeCo alloys: alloy development, processing, and properties. International Materials Reviews, 50, 157-192. http://dx.doi.org/10.1179/174328005X14339

Suryanarayana, C. **(1995)**. Nanocrystalline materials. *International Materials Reviews*, 40. 41-64. http://dx.doi.org/10.1179/095066095790151106

Suryanarayana, C. **(2001)**. Mechanical alloying and milling. *Progress in Materials Science*, 46, 1-184. https://doi.org/10.1016/S0079-6425(99)00010-9

Suryanarayana, C. **(2004)**. Mechanical alloying and milling. *Materials Engineering, Marcel Dekker*, New York. http://dx.doi.org/10.1201/9780203020647

Svanberg, S. **(2004).** Atomic and molecular spectroscopy: Basic aspects and practical applications. New York: *Springer-Verlag*. https://doi.org/10.1007/978-3-642-18520-5

T

Taghvaei, A.H., Stoica, M., Khoshkhoo, M.S., Thomas, J., Vaughan, G., Janghorban, K., Eckert, J. **(2012)**. Microstructure and magnetic properties of amorphous/nanocrystalline $Co_{40}Fe_{22}Ta_8B_{30}$ alloy produced by mechanical alloying. *Materials Chemistry and Physics*. 134, 1214–1224. http://dx.doi.org/10.1016/j.matchemphys.2012.04.031

Tahir, M.B., Rafique, M., Sagir, M. **(2021)**. Nanotechnology trends and future applications. *Springer Nature Singapore Pte Ltd*. http://dx.doi.org/10.1007/978-981-15-9437-3

Takayama. T., Wey, M.Y., Nishizawa, T. **(1981)**. Effect of magnetic transition on the solubility of alloying elements in bcc iron and fcc cobalt. *Transactions of the Japan Institute of Metals*, 22, 315-325. https://doi.org/10.2320/matertrans1960.22.315

Tavakoli, M., Shokrollahi, H., Karimi, L., Janghorban, K. **(2013)**. Investigation of structural, microstructural and magnetic properties of mechanically alloyed nanostructured $(Fe_{50}Co_{50})_{100-x}$ Mo*x*(x = 25,35) powders. *Powder Technology*, 234, 13–18. https://doi.org/10.1016/j.powtec.2012.09.013

Tebib, W., Alleg, S., Bensalem, R., Bensebaa, N., Bentayeb, F.Z., Suñol, J.J., Grenèche, J.M. **(2008)**. Structural characterization of nanostructured Fe-8P powder mixture. *Journal of Nanoscience and Nanotechnology*. 8, 2029–2036. https://doi.org/10.1166/jnn.2008.056

Tebib, W., Alleg, S., Grenèche, J.M., Suñol, J.J. **(2018)**. Thermal stability of the nanocrystalline Fe-8P (wt.%) powder produced by ball milling. *Phosphorus, Sulfur, and Silicon and the Related Elements*, 193. 500-506. https://doi.org/10.1080/10426507.2018.1452233

Teo, B.K., Sun, X. H. **(2007)**. Classification and representations of low-dimensional nanomaterials: Terms and symbols. *Journal of Cluster Science*, 18. 346–357. http://dx.doi.org/10.1007/s10876-007-0125-x

Thangadurai, T.D., Manjubaashini, N. Sabu, T., Maria, H.J. **(2020)**. Nanostructured Materials. *Engineering Materials*. https://doi.org/10.1007/978-3-030-26145-0

Tiwari, N.J., Tiwari, N.R., Kim, S.K., **(2012)**. Zero-dimensional, one-dimensional, two-dimensional and three-dimensional nanostructured materials for advanced electrochemical energy devices. *Progress in Materials Science*, 57. 724–803. http://dx.doi.org/10.1016/j.pmatsci.2011.08.003

Tjong, S.C., Chen, H. **(2004)**. Nanocrystalline materials and coatings. *Materials Science and Engineering R*, 45, 1–88. http://dx.doi.org/10.1016%2Fj.mser.2004.07.001

Tokajuk, G., Niemirowicz, K., Deptuła, P., Piktel, E., Cieśluk, M., Wilczewska, A.Z., Dąbrowski, J.R., Bucki, R. **(2017)**. Use of magnetic nanoparticles as a drug delivery system to improve chlorhexidine antimicrobial activity. *International Journal of Nanomedicine*. 12 7833–7846. http://dx.doi.org/10.2147/IJN.S140661

Tomar, R.S., Abdala, A.A., Chaudhary R.G., Singh, N.B. **(2020)**. Photocatalytic degradation of dyes by nanomaterials. *Materials Today: Proceedings*, 29. 967–973. http://dx.doi.org/10.1016/j.matpr.2020.04.144

Tomar, R.S., Jyoti, A., Kaushik, S. **(2020)**. Nanobiotechnology: Concepts and applications in health, agriculture, and environment. *Apple Academic Press.*

Tucci, P., Porta, G., Agostini, M., Dinsdale, D., Iavicoli, I.,Cain, K., Finazzi-Agró, A., Melino, G.; Willis, A. **(2013)**. Metabolic effects of TiO_2 nanoparticles, a common component of sunscreens

and cosmetics, on human keratinocytes. *Cell Death and Disease*, 4. e549. https://doi.org/10.1038/cddis.2013.76

V

Vas'ko, V.A. Rantschler, J.O. Kief, M.T. **(2004)**. Structure, stress, and magnetic properties of high saturation magnetization films of FeCo. *IEEE Transactions on Magnetics*. 40:2335–2337. https://doi.org/10.1109/TMAG.2004.832256

Venkatesan, K. Supriya, R. Kavya Bai, M.P. Madeswaran, S. Vidya, R. Rajan Babu, D. **(2015)**. Cobalt ferrite ($CoFe_2O_4$) nanoparticles for evaluation of antibacterial activity. *Journal of the Indian Chemical Society*, 92(5):637-639

Villars, P., Prince, A., Okamoto, H. **(1995)**. Handbook of ternary alloy phase diagrams. *ASM International, Materials Park, Ohio*. eds.

W

Wang Y, Xia Y. **(2004)**. Bottom-up and top-down approaches to the synthesis of monodispersed spherical colloids of low melting-point metals. *Nano Letters*. 4:2047-2050. http://dx.doi.org/10.1021/nl048689j

Wang, G., Zhang, R., Jiang, T., Chernova, N.A., Dong, Zh., Whittingham, M.S. **(2014)**. Facile synthesis and electrochemical performance of the nanoscaled FeP_y anode. *Journal of Power Sources*, 270. 248-256. https://doi.org/10.1016/j.jpowsour.2014.07.095

Wang, H., Hu, T., Zhang, T. **(2013)**. Atomic, electronic and magnetic properties of $Fe_{80}P_{11}C_9$ amorphous alloy: A first-principles study. *Physica B: Condensed Matter*. 411, 161–165. http://dx.doi.org/10.1016%2Fj.physb.2012.11.044

Wang, L., Hu, Ch., Shao, L. **(2017)**. The antimicrobial activity of nanoparticles: present situation and prospects for the future. Review. *International Journal of Nanomedicine*. 12 1227–1249. http://dx.doi.org/10.2147/IJN.S121956

Wang, L., Luo, J., Shan, S., Crew, E., Yin, J., Zhong, C-J ,. Wallek, B., Wong, S. **(2011)**. Bacterial inactivation using silver-coated magnetic nanoparticles as functional antimicrobial agents. *Analytical Chemistry*. 83, 8688–8695. https://doi.org/10.1021/ac202164p

Wang, M., Raghunathan, N., Ziaie, B. **(2007)**. A nonlithographic top-down electrochemical approach for creating hierarchical (micro-nano) superhydrophobic silicon surfaces. *Langmuir*. 23. 2300–2303. http://dx.doi.org/10.1021/la063230l

Wareen, B.H. **(1969)**. X-ray diffraction. Addition-Wesley. 275.

Warren, B.H. Averbach, B.L. **(1950)**. *Journal of Applied Physics*. 21:595.

Weiss, P. **(1907)**. L'hypothèse du champ moléculaire et la propriété ferromagnétique. *Journal of Physics: Theories and Applications*, 6. 661-690. http://dx.doi.org/10.1051/jphystap:019070060066100

West, A.R. **(2007)**. Solid state chemistry and its applications. *John Wiley & Sons*.

Whitesides, G. M., Kazlauskas, R. J., and Josephson, L. **(1983)**. Magnetic separations in biotechnology. *Trends in Biotechnology*. 1, 144–148. https://doi.org/10.1016/0167-7799(83)90005-7

Wilcox, B.A., Wright, I.G. **(1974)**. Observations on strengthening and oxidation behavior of a dispersion hardened Fe-Cr-base alloy prepared by mechanical alloying. *Metallurgical Transactions*, 5. 957-960. http://dx.doi.org/10.1007/BF02643157

Williamson, G.K., Hall, W.H. **(1953)**. X-ray line broadening from filed **a**luminium and wolfram. *Acta Metallurgica*, 1, 22–31. https://doi.org/10.1016/0001-6160(53)90006-6

Wu, A., Yang, X., Yang, H. **(2013)**. Magnetic properties of carbonencapsulated Fe–Co alloy nanoparticles. *Dalton Transactions*, 42, 4978–4984. https://doi.org/10.1039/C3DT32639J

Y

Yamamoto, O. **(2001)**. Influence of particle size on the antibacterial activity of zinc oxide. *International Journal of Inorganic Materiels*, 3, 643-646. http://doi.org/10.1016/S1466-6049(01)00197-0

Yang, F., Gao, H., Hao, J., Zhang, Sh., Li, P., Liu, Y., Chen, J., Guo, Z. **(2019)**. Yolk–Shell structured FeP-C nanoboxes as advanced anode materials for rechargeable lithium-/potassium-ion batteries. *Advenced Functional Materials*, 1808291. https://doi.org/10.1002/adfm.201808291

Yang, H. **(2005)**. Principles for characterizing the potential human health effects from exposure to nanomaterials: Elements of a screening strategy. *Particle and Fibre Toxicology*, 2. 8-35. https://doi.org/10.1186/1743-8977-2-8

Yong, K., Roy, I., Law, W., Hu, R. **(2010)**. Synthesis of cRGD-peptide conjugated near-infrared CdTe/ZnSe core–shell quantum dots for in vivo cancer targeting and imaging. *Chemical Communications*,46. 7136-7138. https://doi.org/10.1039/C0CC00667J

You, Zh. **(2020)**. Critical Evaluation and Thermodynamic Modeling of High Alloy Fe-Mn-Al-Si-C-P System. PhD thesis, McGill University, Montreal, Quebec, Canada.

Young, R.A. **(1996)**. The Rietveld method, 1st edn. Oxford University, Oxford

Yuping, D., Yahong, Z., Tongmin, W., Shuchao, G., xin, L., Xingjun, L. (2014). Evolution study of microstructure and electromagnetic behaviors of Fe–Co–Ni alloy with mechanical alloying. Materials Science and Engineering B. 185, 86–93 http://dx.doi.org/10.1016/j.mseb.2014.02.014

Z

Zeleňàkovà, A., Olekšàkovà, D., Degmovà, J., et al. **(2007)**. Structural and magnetic properties of mechanically alloyed FeCo powders. *Journal of Magnetism and Magnetic Materials*, 316, e519–e522. https://doi.org/10.1016/j.jmmm.2007.03.005

Żemczużny, S., Schepelew, J. **(1909)**. The Co-P System. *Zeitschrift für Anorganische and allgemeine Chemie*, 64, 245.257. In German. (Equi Dia- gram; Experimental). https://doi.org/10.1002/zaac.19090640119

Zhang, G-Q., Li, B.,Liu, M-Ch., Yuan, Sh-K., Niu, L-Y. **(2017)**. Liquid Phase Synthesis of CoP Nanoparticles with High Electrical Conductivity for Advanced Energy Storage. *Journal of Nanomaterials.* https://doi.org/10.1155/2017/9728591

Zhang, M. Zhou, P. Li, Q. Gong, P. Wang, X. **(2020)**. Electrodeposition of FeCoP nanoglass films. *Microelectronic Engineering*, 229:111363. https://doi.org/10.1016/j.mee.2020.111363

Zhao, Y., Liao, X. **(2010)**. Ductility of bulk nanostructured materials. *Trans Tech Publications Ltd, Switzerland.*

Zhu, Y.T., Wu, X.L. **(2018).** Ductility and plasticity of nanostructured metals: Differences and issues. *Materials Today Nano*, 2, 15-20. http://dx.doi.org/10.1016/j.mtnano.2018.09.004

Zubair, A., Ahmad, Z., Mahmood, A., Cheong, W-Ch., Ali, I., Khan, M.A., Chughtai, A.H., Ashiq, M.N. **(2017)**. Structural, morphological and magnetic properties of Eu-doped $CoFe_2O_4$ nano-ferrites. *Results in Physics 7*, 3203–3208. http://dx.doi.org/10.1016/j.rinp.2017.08.035